Electronic properties of photochromic switches in hybrid interfaces

D i s s e r t a t i o n

zur Erlangung des akademischen Grades

d o c t o r r e r u m n a t u r a l i u m
(Dr. rer. nat.)

im Fach Physik

eingereicht an der

Mathematisch–Naturwissenschaftlichen Fakultät

der Humboldt–Universität zu Berlin

von

Herrn M. Sc. Qiankun Wang

Präsident der Humboldt–Universität zu Berlin

Prof. Dr.-Ing. Dr. Sabine Kunst

Dekan der Mathematisch–Naturwissenschaftlichen Fakultät

Prof. Dr. Elmar Kulke

Gutachter: 1. Prof. Dr. Norbert Koch

2. Prof. Dr. David Beljonne

3. PD Dr. Sylke Blumstengel

Tag der mündlichen Prüfung: 15.05.2019

To my beloved parents, wife and son!

獻給我深愛的父母，妻子和兒子！

Abstract

Photochromic switches (photoswitches) such as diarylethenes (DAEs), dihydropyrenes (DHPs), azobenzenes and spiropyrans have attracted increasing interest for the development of photoswitchable multifunctional devices, including phototransistors and optical memories. In such devices, their multifunctional properties are fulfilled by modulating the charge transport as well as the interface charge injection with photoswitches upon external stimuli treatment. To fabricate a high-performance and mutifunctional device, a key element is understanding how the electronic properties of photoswitches change upon switching and how the switching modifies the energy level alignment at the photochromic interface of a device. Therefore, the present work of this thesis is to investigate the fundamental electronic properties of photoswitches, i.e., molecular conjugation, dipole moment, energy gaps and frontier levels. Particular focus is on dynamically tuning the frontier level alignment between the (in)organic semiconductors and photoswitches with external stimuli (e.g., light, thermal energy). DAE and DHP molecules are chosen as prototypical photoswitches due to their high switching performance and fatigue resistance.

First, the electronic changes of DAE photoswitches upon light illumination are evidenced by direct and inverse photoemission spectroscopy together with density functional theory calculations, for example, the highest occupied molecular orbital (HOMO) of DAE thin films exhibits an 800 meV difference between their two isomeric states. Similar changes are also found at the lowest unoccupied molecular orbitals. With these light-controlled properties, DAE molecules are then employed to modify the electronic structure at interfaces with organic and inorganic components (e.g., P3HT, N2200, ZnO, ITO). It is proved that upon light illumination DAE molecules can indeed dynamically and reversibly switch the interface frontier level alignment by hundreds of meV.

To obtain knowledge on multiple stimuli-induced switchings, e.g., light and heat, a T-type photoswitch pyridyl-DHP (Py-DHP) is synthesized for this purpose, since Py-DHP can be switched with light in one direction and switched back with heat treatment. The electronic properties at the ZnO/Py-DHP interfaces are investigated both experimentally and theoretically. It is found that, the switching-induced electronic changes are impacted by a Fermi level pinning due to the presence of molecular dipoles. These studies provide a solid basis for the use of photoswitches for dynamically manipulating energy level alignment for charge injections at interfaces with organic and inorganic components, and will aid the development of improved photoswitchable (opto-) electronic devices.

Keywords: photoswitch, diarylethene, dihydropyrene, energy level alignment, photoemission spectroscopy, density functional theory

Kurzfassung

Photochrome Schalter (Photoschalter), wie Diarylethene (DAEs), Dihydropyrole (DHPs), Azobenzole und Spiropyrane, haben ein zunehmendes Interesse an der Entwicklung von photoschaltbaren multifunktionalen Geräten, einschließlich Phototransistoren und optischen Speichern, auf sich gezogen. In solchen Geräten werden die multifunktionalen Eigenschaften der Photoschalter durch Modulation des Ladungstransports sowie der Grenzflächenladungsinjektion bei der Behandlung mit äußeren Stimuli ausgenutzt. Um ein leistungsfähiges und multifunktionales Gerät herzustellen ist es unabdingbar zu verstehen wie sich die elektronischen Eigenschaften von Photoschaltern beim Umschalten ändern und wie das Schalten die Ausrichtung der Energieniveaus an der photochromen Schnittstelle eines Geräts verändert. Daher beschäftigt sich ein Großteil dieser Dissertation mit der Untersuchung der grundlegenden elektronischen Eigenschaften von Photoschaltern, u.a. molekulare Konjugation, Dipolmoment, Energielücken und Grenzniveaus. Ein besonderer Fokus liegt auf der dynamischen Anpassung der Energienieveaus zwischen den (in)organischen Halbleitern und den Photoschaltern mit externen Stimuli (z. B. Licht, Wärmeenergie). DAE- und DHP-Moleküle werden aufgrund ihrer hohen Schaltleistung und Ermüdungsfestigkeit als prototypische Photoschalter ausgewählt.

Zuerst werden die elektronischen Änderungen von DAE-Photoschaltern bei Lichtbeleuchtung durch direkt und inverse Photoemissionsspektroskopie und Dichtfunctionaltheorie nachgewiesen. Beispielsweise zeigt das höchste besetzte Molekülorbital (HOMO) von DAE-Dünnfilmen eine Differenz von 800 meV zwischen ihren beiden isomeren Zuständen. Ähnliche Änderungen lassen sich auch bei den niedrigsten unbesetzten Molekülorbitalen feststellen. Mit diesen lichtgesteuerten Eigenschaften werden dann DAE-Moleküle verwendet, um die elektronische Struktur an

Grenzflächen mit organischen und anorganischen Komponenten (z. B. P3HT, N2200, ZnO, ITO) zu modifizieren. Es wird gezeigt, dass DAE-Moleküle bei Lichtbeleuchtung die Energieniveauanordnung an der Grenzfläche um Hunderte von meV dynamisch und reversibel ändern können.

Um Erkenntnisse über mehrere stimulationsinduzierte Schaltungen, z. B. Licht und Wärme, zu erhalten, wird hierfür ein Photoschalter Pyridyl-DHP (Py-DHP) vom T-Typ synthetisiert, da Py-DHP mit Licht in eine Richtung geschaltet und mit Wärmebehandlung zurückgeschaltet werden kann. Die elektronischen Eigenschaften an der ZnO/Py-DHP-Grenzfläche werden sowohl experimentell als auch theoretisch untersucht. Es hat sich herausgestellt, dass die schaltinduzierten elektronischen Änderungen durch ein Fermi-Level-Pinning aufgrund der Anwesenheit von molekularen Dipolen beeinflusst werden. Diese Studien bieten eine solide Grundlage für die Verwendung von Photoschaltern zur dynamischen Änderung der Energielevelanordnung für Ladungsinjektionen an Grenzflächen mit organischen und anorganischen Komponenten und werden die Entwicklung verbesserter photoschaltbarer (opto-) elektronischer Geräte unterstützen.

Stichwörter: Photoschalter, Diarylethene, Dihydropyrole, Energienieveaus, Photoemissionsspektroskopie, Dichtfunctionaltheorie

Contents

Abbreviations and Acronyms

AFM	Atomic force microscope
BE	Binding energy
CBM	Conduction band maximum
CLS	Core level shift
DAE	Diarylethene
DFT	Density functional theory
DOS	Density of states
EA	Electron affinity
ELA	Energy level alignment
ESCA	Electron spectroscopy for chemical analysis
E_{vac}	Vacuum level
EXAFS	Extended X-ray absorption fine structure
ϕ	Work function
FWHM	Full width at half maximum
GGA	Generalized gradient approximation
HF	Hartree-Fock
HOMO	Highest occupied molecular orbital
IE	Ionization energy
IMFP	Inelastic mean free path
IPES	Inverse photoelectron spectroscopy
ITO	Indium Tin Oxide
KPFM	Kelvin probe force microscopy
LCAO	Linear combination of atomic orbitals
LDA	Local density approximation
LUMO	Lowest unoccupied molecular orbital

N2200	Poly{[N,N'-bis(2-octyldodecyl)naphthalene-1,4,5,8-bis(dicarboximide)-2,6-diyl]-alt-5,5'-(2,2'-bithiophene)}
NEXAFS	Near edge X-ray absorption fine structure
OFET	Organic field effect transistor
OLED	Organic light emitting diode
OPV	Organic photovoltaic cell
P3HT	Poly(3-hexylthiophene)
PA	Phosphonic acid
PA-DAE	Phosphonic acid diarylethene
PBC	Periodic boundary conditions
PBE	Perdew-Burke-Ernzerhof functional
PDOS	Projected density of states
PES	Photoelectron spectroscopy
Py-DHP	Pyridyl Dihydropyran
SAM	Self-assembled monolayer
SECO	Secondary electron cut-off
SP	Surface potential
TEY	Total electron yield
TD-DFT	Time dependent density functional theory
UHV	Ultra high vacuum
UPS	Ultraviolet photoelectron spectroscopy
VBM	Valence band maximum
XAS	X-ray absorption spectroscopy
XPS	X-ray photoelectron spectroscopy
ZnO	Zinc oxide

1. Introduction

Organic (opto-)electronic devices such as organic field effect transistors (OFETs),[1] organic light emitting diodes (OLEDs),[2] and organic photovoltaic cells (OPVs)[3,4] have attracted a great deal of attention in the past decades due to their potential advantages of compatibility with large-area and flexible substrates, low-cost processing and ease of fabrication (see structures in Figure 1.1).[5–11] By definition, in all of these devices there are interfaces between the organic layers and inorganic electrodes.[12,13] The functionality and efficiency of devices are highly dependent on the electronic structure at interfaces. As illustrated in Figure 1.1, for OFETs and OLEDs electrons and holes are injected from both sides of electrodes into organic layers. This requires that the energy level offset at the electrode/organic interface has to be tuned to be favorable for efficient electron and hole injections.[14] While in the case of OPVs, excitons are generated upon light absorption and separated at the organic donor/accepter interface, thus the energy barrier at the donor/accepter interface has to be minimized for the exciton separation and extraction.[15,16] To optimize these interface energy level alignment (ELA) and to achieve optimal charge injections as well as charge transport, great efforts have been devoted to engineering the interface energy levels with organic functional molecules.[17] For example, the use of interfacial organic layers (as thin as monolayers) composed of strong electron accepter molecules have been proven feasible to substantially tune the hole injection behaviors by changing the energy barriers between the highest occupied molecular orbitals (HOMO) levels,[18] *vice versa* for tuning electron injections using a layer of electron donor molecules.[19] However, the abovementioned approach is limited to a static modification of energy level alignment at the interface. More recently, it has been shown that the use of photochromic switches (photoswitches) enables a dynamic energy level tuning;[20,21] this gives rise to multifunctional properties of the interface as the interfacial

energy level alignment can be controlled and programmed via external stimuli such as light and heat, even in fully processed and encapsulated device stacks.[20,22]

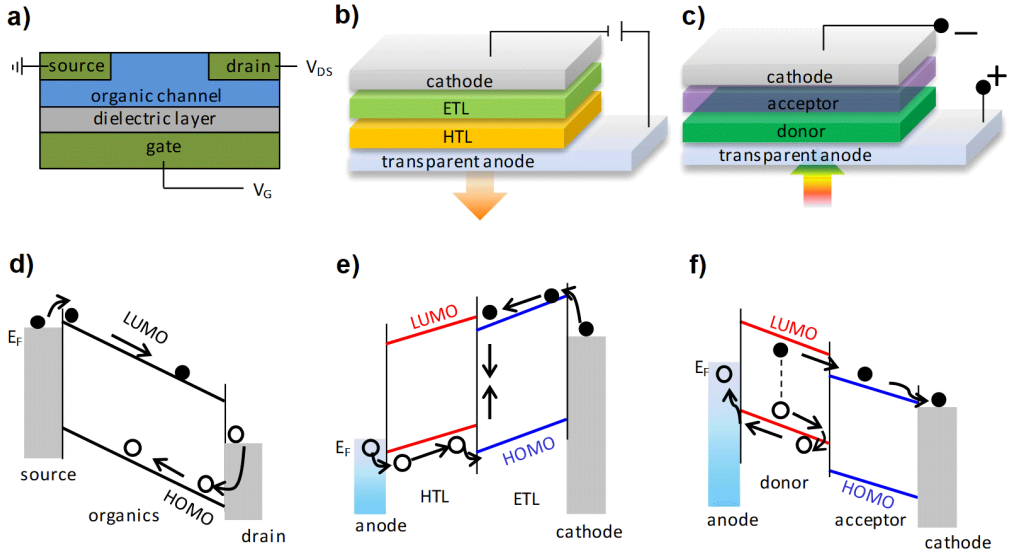

Figure 1.1. Schematic of typical organic devices that are composed of organic layers and metallic electrodes. a) Organic field effect transistors (OFET). The corresponding energy level alignment in the device is shown in Figure d), where charge injection processes are depicted. The structure of an organic light emitting diode (OLED) is plotted in b), the device active layers consist of an electron transport layer (ETL) and a hole transport layer (HTL). The energy level alignment in e) shows that charges are injected into the organic layer and recombine at the HTL/ETL interface. The structure of organic photovoltaic cells (OPV) is shown in c); the organic donor/accepter layers are the key components for charge generation, as shown in the energy level diagram in f), excitons are created in the donor layer, and they are separated at the organic/organic interface.

To achieve a multifunctional nature in organic devices, for example, for OFET the device can be remotely controlled between its on and off states by simple external light illumination with different wavelengths,[23–27] a key point is to decorate the organic and inorganic surface in the device with multifunctional molecular layers, thus tuning the interface electronic properties in a dynamic and reversible manner (see Figure 1.2a). Therefore, photoswitches are perfect candidates for satisfying this requirement since these molecules can change their electronic and structural properties upon external stimuli treatment,[28,29] e.g., light, heat, and PH values. Currently in the family of photoswitches, diarylethenes (DAEs), dihydropyrenes (DHPs), azobenzenes and spiropyrans have been mostly investigated regarding their different switching and optical properties.[30–32]

However, from a device application point of view, the photoswitches must exhibit optimal switching properties, including selective excitation in the desired wavelength range, high photoisomerization quantum yields, high fatigue resistance and control over the thermally back isomerization. Additionally, they require a maximum change in the desired property between the two interconverting states, related to ionization/affinity levels, shape/aspect ratio, absorption/emission, etc. Therefore, DAE and DHP photoswitches have been chosen in this work as typical study cases since these two molecules fulfill mostly the abovementioned properties (detailed descriptions will be shown in the second chapter). It has been proposed observed previously that,[21,33] due to the photochromic reaction, these molecules can switch reversibly between two (meta-)stable isomers. Switching between the two isomers fundamentally changes the electronic properties of the molecules, e.g., the optical gap, molecular dipole moment, molecular electron affinity, and ionization energy.[21] Therefore, using the photoswitches as photo-addressable interlayer between an (in)organic semiconductor and an electrode, the photo-induced switching can tune charge transport as well as charge injection (extraction) properties in organic devices, which have multifunctional characters (see Figure 1.2b). The underlying mechanism is that the energy level offset between the HOMO level of photoswitches and either the Fermi level (E_F) of the electrode or the valence band of the organic semiconductor in the device is minimized for one isomer state and maximized for the other. Analogous arguments apply when considering the lowest unoccupied molecular orbital (LUMO) level and the conduction band. Consequently, the electrical properties of the devices are modulated by either the formation of photoswitchable "trap states" or energy barriers for charges at interfaces,[20] and multifunctionality is realized as the device can be addressed electrically and optically. Thus the investigation of the electronic properties of photoswitches as well as the understanding of their impacts on the interfacial energy level alignment tuning upon switching is of high importance for developing and achieving high-performance, multifunctional devices. With this in mind, the present work in this thesis will focus on studying the electronic properties of photoswitches mainly using photoemission spectroscopies and density functional theory (DFT). The purpose of this work is to

understand *i*) switching-induced electronic changes in the photoswitchable molecules, i.e., frontier levels, dipole moments, HUMO-LUMO gaps; *ii*) electronic structure at organic/photoswitch and hybrid inorganic/photoswitch interfaces, particularly to understand how the photoswitch can dynamic tune the interface energy level alignment.

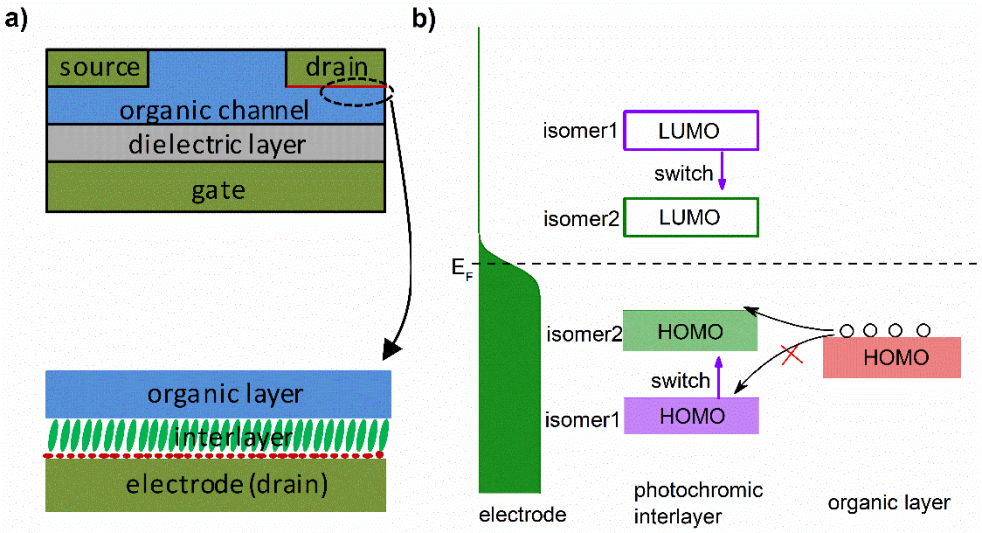

Figure 1.2. a) Device structure of an OFET with its electrode decorated by a layer of photoswitches, with which the energy level alignment between the electrode and the organic layer can be dynamically manipulated via external stimuli. As shown in Figure b), upon switching from isomer1 states to isomer2 states, the HOMO (LUMO) levels of photoswitches shift upwards (downwards) dramatically. Thus the injection/extraction of holes (electrons) from the organic layer to the electrode becomes possible.

The thesis is structured in the following way: First, to get familiar with the properties of organic molecules and their relevant interfaces, in chapter 2 the fundamental properties of conjugated organic semiconductors are introduced, the main discussion is about the conjugated nature in organic molecules and the change of molecular gaps when going from single molecule to solids. Then photoswitches is particularly discussed regarding to these fundamental properties. In section 2.2, electronic theories and models in dealing with electrons in solids is outlined, later the concept of density of states and electron occupation is introduced, which is important for understanding this work. Section 2.3 is about the fundamentals for organic semiconductors at interfaces; the interactions of molecules at interfaces are first described, then the energy level alignment at interfaces as well as the underlying mechanisms is detailed introduced. The following chapter 3

describes various experimental techniques and theoretical methods that are related to this work. The working principles of photoemission spectroscopy, X-ray absorption spectroscopy and atomic force microscope will be the main focus for the experimental setups and a general introduction of the density functional theory is also included. Details about materials used in this work and experimental setups are described in chapter 4. The sample preparation and measurement with different setups, as well as the data processing are detailed explained. The following chapter 5 is the main part of this thesis; this chapter is divided into four parts. To understand the electronic properties of photoswitches, DAE molecules under the form of thin films were first investigated due to their high fatigue resistance and thermal stability. Upon switching *in situ* with UV and visible light, respectively, the electronic properties of DAE, such as optical gaps dipole moments ionization/affinity energy, are fully revealed with its two isomeric states. Subsequently, to verify the feasibility of dynamic energy level tuning with photoswitches at the metal/organic and organic/organic interfaces, DAE thin films were deposited onto both an Au and two polymer surfaces (subsection 5.1.2). it was shown that DAE molecules can switch with light not only in the bulk but also at the interface. After light illumination, the interfacial energy level alignment becomes totally different, meaning that DAE molecules can indeed switch the energy level alignment at the metal/organic and organic/organic interfaces. However, due to the lack of an anchoring group in the DAE molecule, DAE molecules cannot bind to the inorganic substrate in the form of chemisorption. This is problematic for fabricating a photochromic interlayer (see Figure 1.2) in devices, since the photoswitches will be "washed away" when depositing organic layers on top. To investigate the possibility of functionalizing electrode surfaces via chemisorption, a strong anchoring group has been implemented to DAE molecules, namely phosphonic acid DAE (PA-DAE). In literatures the PA anchors have been proved to bind chemically on metal-oxide surfaces,[34,35] thus to study the interface of chemisorbed photoswitches, we choose zinc oxide (ZnO) as the inorganic component; PA-DAE was then deposited under the form of self-assembled monolayers (SAM) on polar ZnO surface. This work is shown in section 5.2. Given the feasibility of PA-DAE for dynamic

modification of ZnO, it is expected that such molecules will have similar effects on indium-tin-oxide (ITO), which has been mostly used as a transparent electrode. Thus the PA-DAE modified ITO surface has been further investigated in section 5.3. After getting familiar with the light-triggered photoswitches, it is then necessary to understand the impacts of different stimuli, such as light, and heat or PH on the switching and electronic properties of photoswitchable molecules. To address this multiple switching property, a negative T-type switch pyridyl-DHP (Py-DHP) was introduced to switch the ZnO surface. This work can be found in section 5.4. Finally, in chapter 6 conclusions and an outlook about the present work are given.

2. Fundamentals

In this chapter, the fundamental physics about organic semiconductors and interfaces will be elaborated on, since they are necessary to help understand the present work. The chapter starts with an introduction of conjugated organic semiconductors with special focus on photoswitches. Then followed by the electronic structure theory which deals with electrons in solids. Furthermore, a detailed discussion of the organic semiconductor electronic properties at interfaces will be presented.

2.1 Conjugated Organic Semiconductors

Organic semiconductors are playing an important role in organic (opto-)electronic devices in recent years due to their unique electronic properties, such as strong light-matter coupling, easily tunable electronic levels.[36–38] The nature of intermolecular bonding in organic semiconductors is fundamentally different from that in inorganic counterparts. Organic molecular solids are *van der Waals* bonded, which indicates a considerably weaker intermolecular bonding compared to covalently bonded inorganic semiconductors, e.g., silicon. Consequently, the weaker bonding results in a weaker delocalization of electronic wave functions amongst neighboring molecules. In general, there are two major classes of organic molecules: low-molecular weight molecules and polymers;[39] both of them consist of conjugated π-electron systems formed by the *pz* orbital of sp^2-hybridized carbon atoms (see Figure 2.1 for example). Compared to σ bond, which constitutes the molecular backbones, the energy of π bonding is relatively weaker. Thus the π orbital is located higher than the σ orbital. While for the unoccupied orbitals, σ* is located higher than π* orbitals (see Figure 2.1b). This results in a lowest electronic transition from the bonding to antibonding orbitals, that is the π-π* transition. The energy difference between the π energy level and the π* energy level is the energy gap or band

gap (E_{BG}) of organic molecules. Typically, the magnitude of E_{BG} for most of organic molecules is between 1.5 and 3 eV.[40]

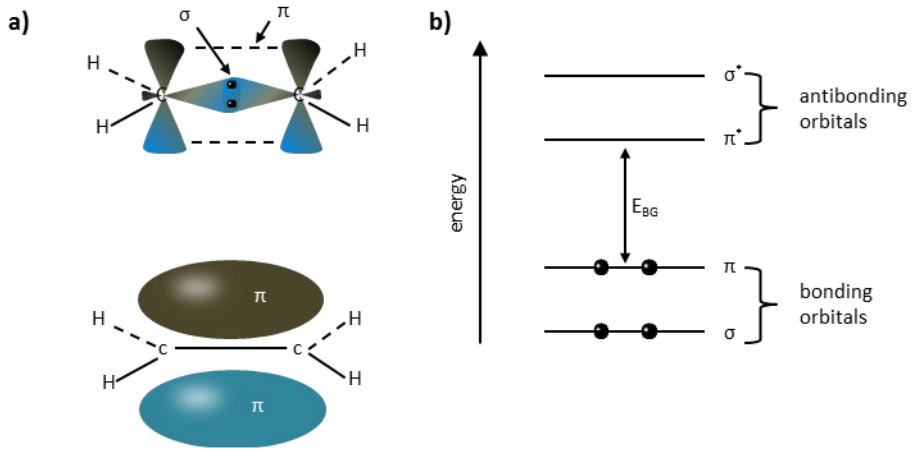

Figure 2.1. a) σ and π bonds in a typical organic molecule ethene, which is the simplest conjugated π electron system. b) Energy levels of a π-conjugated molecule. The unoccupied states (σ, π*) form antibonding orbitals, while the occupied states form bonding orbitals. The gap between the highest occupied and the lowest unoccupied levels is defined as the band gap E_{BG}.*

The evolution of molecular levels going from the gas phase to solids is depicted in Figure 2.2. For a gas-phase molecule, the energy difference between the HOMO level and the vacuum level (E_{vac}) is defined as the ionization energy (IE_{gas}). Likewise, the energy difference between the LUMO level and the vacuum level (E_{vac}) is defined as the electron affinity (EA_{gas}). When many single molecules are brought together to form organic solids, the gap of the solid between the HOMO and LUMO is much smaller compared to that of single molecules. This is mainly due to the polarization effect,[41] which can be understood by considering that an electron (hole) is introduced into the LUMO (HOMO) of solids, the electronic polarization of molecules surrounding the ionized molecules stabilize the ion by electrostatic screening, thus resulting in an increase of EA by P_- and decrease of IE by P_+.[42] The IE and EA in a solid is expressed as:

$$IE_{solid} = IE_{gas} - P_+, \; EA_{solid} = EA_{gas} + P_- \tag{2.1}$$

Moreover, the polarization effect of surrounding molecules can be impacted by other factors, such as structural order of molecules.[43] When going from ordered crystal to amorphous solid, the local variation of polarization energies, due to the different local

environments, plays a role in the distribution of the transport sites that lead to a Gaussian distributed density of states.[44]

However, regarding the energy gap of organic solids, it is generally found that the gap measured by optical means (as referred to optical gap), such as UV-vis absorption, is usually hundreds of meV smaller than that measured by photoemission spectroscopy (which is the so-called transport gap).[45] This is due to the presence of exciton binding energies. The relationships between the optical and transport gaps is thus given by: $E_{trans} = E_{opt} + E_{exciton}$.

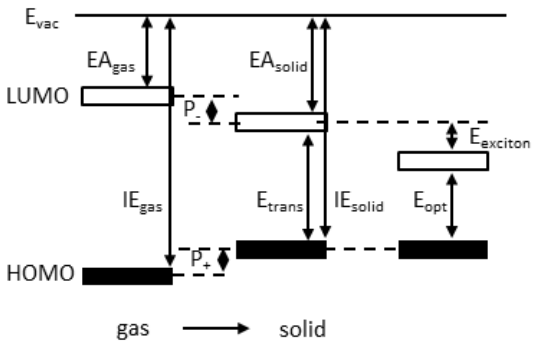

Figure 2.2. Schematic energy diagram of frontier levels for molecules going from the gas phase to solid states. The energy gap between the LUMO and HOMO of the gas molecules is originally very large, after forming solids, the EA level is lowered while the IE level is lifted up due to the polarization effect. Accordingly, this results in a smaller energy gap. Adapted from reference 42.

2.1.1 Photoswitches

Photoswitches are a type of conjugated organic molecules that are mostly studied in this work. Generally, such switches can undergo reversible, photo-triggered isomerization between at least two (meta)stable states. Figure 2.3 schematically illustrates the switching mechanism for commonly used photoswitches, whose two isomeric states are depicted by the local minima in the ground state. It is shown that the photo-isomerization of isomer1 occurs by the excitation of electrons with photon energy of hv' from the isomer1 ground state to its excited state. Then the excited electrons undergo a relaxation process in the excited level and finally fall back to the isomer2 ground state. *Vice versa* for the photo-isomerization of isomer2 with an excitation energy of hv. In some cases, when the potential barrier (ΔE_{act}) between the two isomers are relatively low in the ground states, the switching can be triggered upon proper thermal energy; this provides a possibility to thermally controlling the photoswitch isomerization process.

Hitherto, a variety of photoswitches have been designed and synthesized.[46] Depending on the type of chemical process involved in the switching process, photoswitches can be classified into several families:

i) pericyclic reactions including electrocyclizations like spiropyrans/-oxazines, fulgides and diarylethenes, or cycloadditions in aromatic compounds;

ii) E/Z isomerizations such as azobenzenes, stilbenes and so on;

iii) intramolecular hydrogen/group transfer such as anils and polycyclic quinones;

iv) photo-induced bond cleavages such as triarylmethanes and perchlorotoluene;

v) electron transfers (redox) such as viologens.

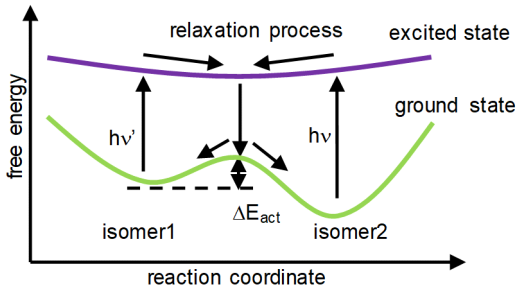

Figure 2.3. Potential energy surface of photoswitches with their two (meta-) stable states. The x-axis is the reaction coordinate, whose parameter can be a distance between two atoms or angle they have with respect to each other. The y-axis shows free energy. The excitation of ground states to excited states is triggered by light illumination, while the two states can also be switched thermally if the activation energy (ΔE_{act}) is relatively low.

Among all photoswitches, azobenzenes, dihydropyrenes (DHPs), diarylethenes (DAEs) and spiropyrans are the most widely used photochromic molecules (see Figure 2.4); among these four, the photoisomerization is accompanied either geometrical changes or electronic level reorganizations. To enable an effective energy level alignment tuning in photoswitchable devices, the investigation of photoswitch electronic changes is of particular interest in this work. Therefore, two of typical photoswitches are used in this work, that is DAE and DHP molecules. Both of them have two (meta)stable isomeric states, i.e., open and closed isomers. Upon light illumination with different wavelength, they undergo not only small geometrical changes but also significant electronic property reorganizations; these physical properties will be revealed later experimentally and theoretically.

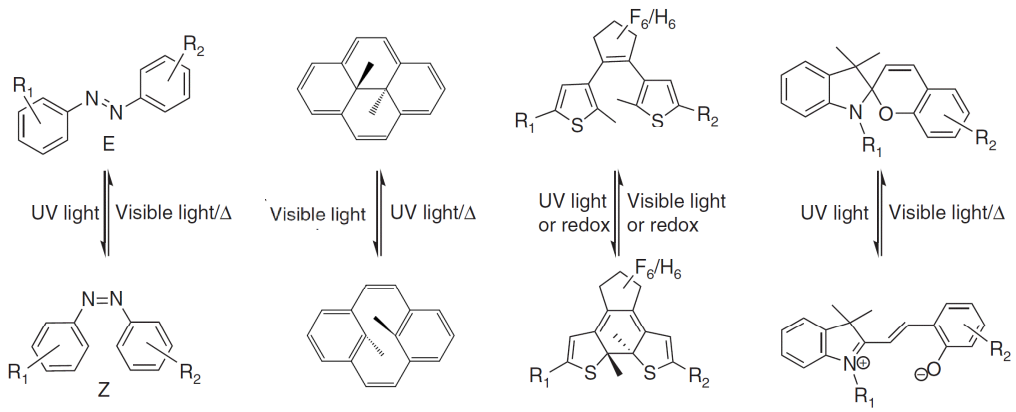

Figure 2.4. Chemical structures of the mostly used photoswitches. Azobenzenes, dihydropyrenes and spiropyrans (from left to right) are reversibly switched either optically or thermally. While diarylethenes can be reverted photochemically or electrochemically. Figure was adapted from Nat Commun.2016, 7, 11118.

Depending on their thermal stability, photoswitches are classified into two different types, that is P-type (thermally irreversible, but photochemically reversible) and T-type (thermally reversible) photochromic molecules.[33] The diarylethene families are typical P-type photoswitches, the DAE switches are derivatives of stilbene.[33] When phenyl rings of stilbene are replaced with five-membered heterocyclic rings with low aromatic stabilization energy, e.g., thiophene, furan rings, both open- and closed-ring isomers become thermally stable, meanwhile, coloration/decoloration cycles can be repeated many times. Thus the advantages of DAEs as photoswitches are: *i*) Both isomers are thermally stable: well-designed derivatives have a half-life time at room temperature longer than 400000 years;[47] *ii*) switching cycles can be repeated more than 10000 times;[48] *iii*) the quantum yield of coloration is close to 100%; *iiii*) photochromic reactions can take place even in the single crystal phase.[49] Regarding the electronic properties of DAE, the π-conjugation of the open-ring isomer is localized in the thiophene ring, and the HOMO-LUMO gap is usually large. After switching to the closed-ring isomer, the π-conjugation delocalizes throughout the molecule, thus resulting in a smaller HOMO-LUMO gap. Moreover, the density of states (DOS) in the valence region is fully reorganized. In contrast, the DHP molecules fall into T-type photoswitches, since the ring-closure reaction can be triggered both photochemically and thermally (as shown in Figure 2.4, second molecule). With this property, it enables us to study the switching-induced

electronic changes using different external stimuli. Similar to DAE, the switching of DHP also leads to changes in the molecular conjugation as well as the DOS. The advantage of DHP compared to other photoswitches is that it can be submitted to a wide range of substituents aiming at either tuning its photochemical electronic properties or at allowing its integration with (in)organic components. For example, when DHP is decorated with a specific anchoring group, it can be adsorbed to inorganic semiconductors; this system can be applied to photoswitchable devices (detailed discussion will be in chapter 5).

2.2 Theory of Electrons in Solids

A theoretical understanding of the electronic properties in (organic) solids is introduced and discussed in this chapter. Based on the quantum mechanics, the discussion will mainly focus on single electron approximations in a periodic solid structure. This will be helpful for understanding the physical properties of (in)organic semiconductors. Furthermore, the formation of the band (energy) gap as well as the density of states will be elucidated.

2.2.1 Nearly Free Electron Approximation

For a metallic solid, electrons in the highest occupied levels are weakly interacted with the nuclei. Thus the behavior of such electrons can be treated as free electrons perturbated by a weak periodic potential.[50] For an electron in a constant potential field (here is the zero order approximation), the time independent Schrödinger equation is written as:

$$\widehat{H}_0\Psi = E\Psi, \ \ \widehat{H}_0 = -\frac{\hbar^2}{2m_e}\nabla^2 + V_0 \tag{2.2}$$

Apparently, the eigenvalues of equation 2.2 are $E_0 = \hbar^2 k^2/2m_e + V_0$, which is based on the free electron model. The wave function of an electron is in the form of plane waves. By applying periodic boundary conditions (PBC) to the solid, the wave vector k is calculated to be:

$$k = n\frac{2\pi}{Na}, \ \ n = 1,2,3 \ldots \tag{2.3}$$

where a is the lattice constant of the crystal solid. Then by applying a periodic potential to equation 2.2, the Hamiltonian $\widehat{H}$ is expressed as:

$$\hat{H} = \hat{H}_0 + \hat{H}', \;\; \hat{H}' = V_p - V_0 \tag{2.4}$$

where V_p is the periodic potential caused by ions in a periodic structure of the solid, and it is considered as a perturbation as the interaction between the electron and nuclei is very weak. Thus equation 2.2 is rewritten as:

$$\left(-\frac{\hbar^2}{2m_e}\nabla^2 + V_0\right)\psi + \left(V_p - V_0\right)\psi = E\psi \tag{2.5}$$

Equation 2.5 is the Schrödinger equation of the nearly free electron approximation model. The wave function of an electron in a periodic solid is the form of Bloch waves. The periodic potential $(V_p - V_0)$ that an electron can feel in the atom is actually inversely proportional to the electron to atom distance. One simple way is to consider such a potential as a constant; this is the so-called Kronig-Penney model that has been discussed intensively in textbooks.[51] Here, the focus is on the electron energy distribution and the resulting band gaps. According to the perturbation theory, the eigenvalue of an electron in equation 2.5 can be expressed as:

$$E(k) = E_0(k) + E_1(k) + E_2(k) + \cdots \tag{2.6}$$

Equation 2.6 describes that the electron total energy $E(k)$ is a summation of the energy of a free electron and the energy due to perturbation. If one considers a second order of perturbation, $E(k)$ is given by:

$$E(k) = \frac{\hbar^2 k^2}{2m_e} + V_0 + \sum_n \frac{|V_p(n)|^2}{\frac{\hbar^2}{2m_e}[k^2 - (k + 2\pi\frac{n}{a})^2]} \tag{2.7}$$

$$V_p(n) = \frac{1}{a}\int_0^a e^{-i(2\pi n/a)\xi} V_p(\xi) d\xi, \;\; \xi = x - na \tag{2.8}$$

Therefore, at zero order approximation, the electron energy is dealt with the free electron model, and its energy becomes quasi-continuous. After considering the perturbation, there exists band gaps (E_{BG}) when $k \sim n\pi/a$.

$$E_{BG} = 2|V_1|, 2|V_2|, \ldots 2|V_n| \tag{2.9}$$

2.2.2 Linear Combination Atomic Orbitals Approximation

For a non-metallic system, e.g., semiconductors, insulators, electrons are strongly interacted with the potentials created by atoms. This to some extent cannot be considered as a nearly free electron approximation. On the other hand, a different model, which is

the so-called linear combination of atomic orbitals (LCAO) approximation (also tightly bound model), will be suited for describing such a system. The LCAO states that the electron in an isolated atom is considered as a zero-order approximation; while the interactions between the electron and the rest of atoms in a *N*-atom system are considered as a perturbation. The zero-order approximation Schrödinger equation is given by:

$$\widehat{H}_{at}\varphi_i(r) = E\varphi_i(r) \tag{2.10}$$

where $\widehat{H}_{at}$ is the Hamiltonian for an atom. Before bringing *N* atoms into contacts, the wave function of an electron is mostly localized to an isolated atom. After the *N* atoms are brought close to each other to form a solid, the Schrödinger equation of the i^{th} electron is written as:

$$(-\frac{\hbar^2}{2m_e}\nabla^2 + V_i)\varphi_i(\vec{r}) + (V_p - V_i)\varphi_i(\vec{r}) = E_i\varphi_i(\vec{r}) \tag{2.11}$$

Note that in equation 2.11 the potential difference between V_p (the potential of the system) and V_i (the potential of the i^{th} atom) is the perturbation part. Taking this perturbation into consideration, the wave function of the i^{th} electron in the interacting system becomes the sum of the wave functions of electrons belonging each atom in the system and is thus written as:

$$\varphi(\vec{k},\vec{r}) = A\sum_R c_i w(\vec{r},\vec{R}) \tag{2.12}$$

Equation 2.12 describes the principle of LCAO. $w(\vec{r},\vec{R})$ is the so-called Wannier type function, which describes the wave function of localized electrons in real space, c_i is the Bloch factor, which describes the wave function modulation. To make the wave function of the electron in the interacting system in the form of Bloch waves, equation 2.12 can be rewritten as:

$$\varphi(\vec{k},\vec{r}) = \frac{1}{\sqrt{N}}\sum_R \varphi(\vec{r},\vec{R})e^{i\vec{k}\cdot\vec{R}} \tag{2.13}$$

In the tight binding model, the eigenvalues of *N* electrons are dispersed by the periodic potential perturbation. One typical example is that, considering the electrons in the *s* orbital, one solves the equation 2.11 with a wave function $\varphi(\vec{k},\vec{r})$ that is composed of

Wannier functions (see equation 2.13). The eigenvalues of electrons are finally calculated to be:

$$E(k) = E_i + \sum_R J(\vec{R}) e^{i\vec{k}\cdot\vec{R}} \tag{2.14}$$

where $J(\vec{R})$ is the function which is related to the position between two atoms. Note that E becomes non-degenerate and exhibits a dispersion with respect to k for an interacting system. A simple case is that, when the electron is in a simple cubic unit cell, the energy of electrons can be expressed by considering the perturbations with neighboring atoms:

$$E(k) = E_i + 2J[\cos(k_x a) + \cos(k_y a) + \cos(k_z a)] \tag{2.15}$$

where the band gap is calculated to be 12*J*.

2.2.3 The Density of States

The dispersion relationship yields how the energy of electrons depends on the k vector. In the following it will be discussed how many states that are allowed to be occupied at a given energy interval. This quantity is called the density of states (DOS), which is written as *D(E)*. In general, the DOS is related to eigenvalues of a Hamiltonian; it is a simple count of states at any given energy interval:

$$D(E) = \sum_{n=1}^{\infty} \delta(E - E(\vec{k}_n)) \tag{2.16}$$

where a delta function is used for describing the distribution of the states. In some cases, the delta function is broadened with a Gaussian profile to describe a real system in experiments. The sum of the DOS gives the total number of states. Equivalently, the DOS can also be expressed as the derivative of the microcanonical partition function $Z(E_{\vec{k}})$ in $\vec{k}$ space with respect to the energy:

$$D(E) = \lim_{\Delta E \to 0} \frac{\Delta Z(E)}{\Delta E} = \frac{V}{4\pi^3} \int \frac{dS}{\nabla_k E} \tag{2.17}$$

where $Z(E)$ is the number of states, S is the area of the constant energy surface. For simplicity, the DOS of free electrons is only discussed as S is easy to calculate. However, for nearly free electrons and tight-binding electrons, their constant energy surfaces are far more complicated, and will not be discussed here. Considering the free electrons in three-

dimensional $\vec{k}$ space, the constant energy surface is a sphere, that is $S = 4\pi k^2$. It is not difficult to calculate the DOS per volume:

$$D(E) = \frac{1}{2\pi^2}\left(\frac{2m_e}{\hbar^2}\right)^{3/2}\sqrt{E} \tag{2.18}$$

Electron population

Base on the above discussions about the DOS, it will be necessary to further discuss the population of electrons at a given energy per volume. Intrinsically, the density of electrons at a given energy is expressed as:

$$n(E) = \int f(E)D(E)dE\,,\ \ f(E) = \frac{1}{1+\exp((E-E_F)/K_BT)} \tag{2.19}$$

where $f(E)$ is the Fermi-Dirac distribution. Inserting equation 2.18 to equation 2.19 gives rise to the expression of the density of electrons in the conduction band and the density of holes in the valence band, respectively.

$$n_c(E) = N_c exp\left(-\frac{E_c-E_F}{k_BT}\right),\ \ n_V(E) = N_V\, exp\left(-\frac{E_F-E_V}{k_BT}\right) \tag{2.20}$$

with N_C and N_V the effective density of states of conduction and valence bands, respectively. Note that equation 2.20 is derived according to the Boltzmann statistics, meaning that the description of charge densities only applies for a non-degenerate semiconductor ($|E - E_F| \gg 3K_BT$). While regarding a degenerate semiconductor, one has to follow strictly the Fermi-Dirac distributions.

2.3 Organic Semiconductors at Interfaces

When two different materials are brought into contact with each other, an interface is formed between the two. Depending on the nature of the constituent molecules of the two materials, the interfacial interactions between molecules can be either physisorbed (dominated by *van der Waals* forces) or chemisorbed (in the form of chemical bonds). This gives rise to dramatically different interfacial charge distributions, energy level alignments and molecular orientations. The complicated physical phenomena existing at the interface affect significantly the interface electronic properties and will be shortly discussed in the following sections.

2.3.1 Physisorption and Chemisorption

2.3.1.1 Physisorption

Generally speaking, physisorption is a process in which the electronic structure of the molecule or atom is hardly impacted upon adsorption. The corresponding mechanism in molecular physics is the *van der Waals bonding*, whose attractive force is due to correlated charge fluctuations in the two bonding partners, i.e. between mutually induced dipole moments (the so-called dipole-dipole interactions). The attractive potential of the *van der Waals* interaction between mutually induced dipoles is described with the *Lennard-Jones potential*:[52]

$$U(r) \propto [(\frac{r_0}{r})^{12} - (\frac{r_0}{r})^{6}] \tag{2.21}$$

with r_0 the position where the potential energy is at its minimum. This equation describes the change of potential energy as a function of the distance between two molecules or atoms. The first part is the short-ranged repulsive forces; and the second apart is the attractive force contributions of the *van der Waals* potential.

Image Charge Model for Lateral Interactions

When a layer of molecules is physisorbed on a substrate, the induced interface dipoles are formed due to charge redistribution. The potentials created by these dipole moments are highly impacted by the lateral dipole-dipole interactions between two (or more than two) adjacent molecules. This can be modeled classically in the framework of image charge model.

As illustrated in Figure 2.5a, at the interface of two different molecular layers (different dielectric constant in this case), the dipoles are considered to be formed by one negative charge in dielectric ε_1 and its image charge image part in dielectric ε_2. The interaction energy between two dipoles is then expressed as:[53]

$$U(d) = \frac{(q^-)^2}{4\pi\varepsilon_1 d} + \frac{2q^-q^+}{4\pi\varepsilon_1\sqrt{4z^2+d^2}} \tag{2.22}$$

where z is the distance between the surface and the point charges, d is the horizontal distance between two dipoles. The first part describes the repulsive contributions of dipoles caused by the negative charge q^-; the second part describes the attractive

contributions with the modified image charges $q^+ = q\frac{\varepsilon_1-\varepsilon_2}{\varepsilon_1+\varepsilon_2}$ due to different dielectric constants.

A simple case is to consider a metallic substrate, thus the image charge in the substrate is: $q^+ = q$. Figure 2.5b depicts the effect of dipole-dipole interactions on the potential energy *U(d)*, which is plotted as a function of *d* for different fixed *z* distance. The plotting shows that *U(d)* is dominated by the repulsive force in the low *d* limit, and it turns to be attractive when *d* increases. Moreover, by calculating the first order derivative of *U(d)*, the energy minimum is derived at $d \approx 2.6z$. It is noted that, this energy mumimum shifts towards larger distance (*d* becomes larger) when the molecule to surface distance *z* increases, meaning that the packing density of charged molecules will be smaller for larger *z*-distance.

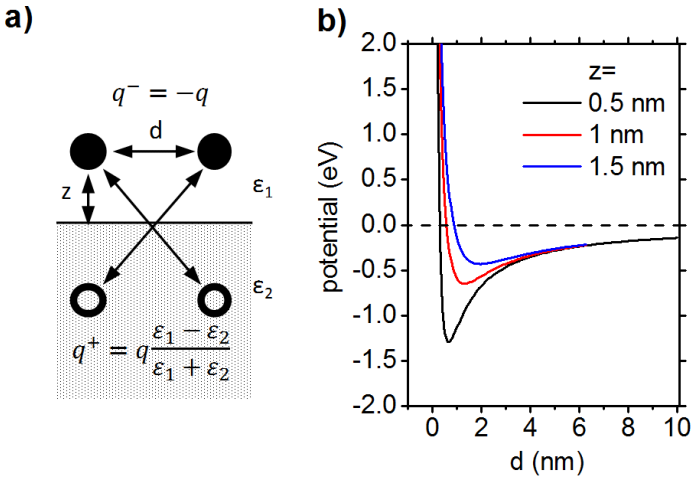

Figure 2.5. a) Schematic illustration of two adjacent dipoles that are formed by electrons and their image charges in the substrate with the same distance z to the surface. b) Interaction potentials between the two dipoles as a function of distance d. For different electron-image charge distances 2z, ranging from 0.5 to 1.5 nm, the minimum energy of the system shifts towards higher d. Figures are adapted from reference 53.

Based on the image charge model, it is of importance to discuss further the potential change created by such dipoles at the interface. As discussed above, the arrangement of

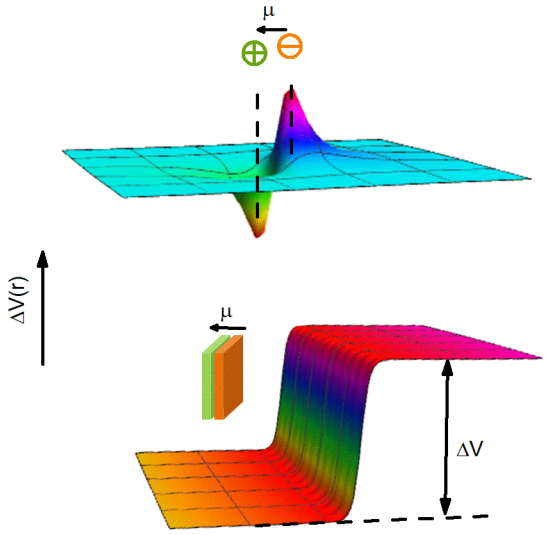

Figure 2.6. Potential change created by a single dipole μ (top Figure) and a layer of dipole mesh (bottom Figure). In both cases, the direction of the potential increase is opposite to the direction of dipoles. Figure was adapted from reference 54.

charged molecules is dominated by the dipole-dipole interactions, and the molecular packing is given at the energy minimum ($d = 2.6z$). In this case, the potential drop (ΔV) above the surface can thus be considered as the sum of potentials created by these dipoles, i.e., negative charges in the molecule and their image parts in the substrate. Therefore, ΔV is written as (detailed derivation see appendices C):

$$\Delta V(\vec{P}) = \frac{1}{4\pi\varepsilon_1}\sum_{i=1}^{N}\left(\frac{q_i}{\vec{r}_i-\vec{P}} + \frac{q_i'}{\vec{R}_i-\vec{P}}\right), \quad q_i' = q_i\frac{\varepsilon_1-\varepsilon_2}{\varepsilon_1+\varepsilon_2} \tag{2.23}$$

with N the number of dipoles considered, q_i the charge above the surface, and q_i' the image charge. In Figure 2.6, the potential drop is plotted with respect to the number of dipoles. It shows that the potential is higher in the negatively charged region compared to that in the positively charged region. In the case of single dipole moment μ (see top Figure), the created potential vanishes very rapidly,[54] when it comes to a dipole layer (bottom Figure), the potential ΔV beyond the dipole mesh becomes rather constant. As a consequence of this step-like potential at the surface, not only the adsorbed molecules in the first monolayer, but also the entire bulk materials in contact with the surface lie at the higher potential energy region.

2.3.1.2 Chemisorption

Chemisorption of molecules (or atoms) to the surface describes the interactions as the formation of a chemical (usually covalent) bond. The adsorption energy for chemisorption is usually ten times higher than that of physisorption. Practically, the adsorption energy (E_{ad}) can be expressed as:

$$E_{ad} = E_{sys} - (E_{mol} + E_{sub}) \tag{2.24}$$

where E_{sys} denotes the energy of the adsorbed system, E_{mol} denotes the energy of the molecule before the adsorption, E_{sub} denotes the energy of the substrate. Chemisorption is accompanied by a rearrangement of the electronic orbitals, i.e. of the electronic shell of the adsorbate atoms or molecules; the geometry of the adsorbate is thus changed due to its new chemical bonds to the substrate. In the case of chemisorption of molecules, this rearrangement of the electronic shell can lead to dissociation and formation of new adsorbate species at the interface. This is the so-called *dissociative adsorption*.[55] Chemisorption is also accompanied by a process of charge transfer.[56] Depending on the formation of covalent or ionic bonding, the extent of charge transfer can be either pronounced (i.e., integer),[57–59] or shared between atoms (i.e., partial).[60,61] The potential drop at the interface created by charge transfers can be elucidated with Poisson's equation, which will be discussed in details in the following section.

2.3.2 Energy Level Alignment

The energy level alignment (ELA) at the organic/organic or inorganic/organic semiconductor interface plays a very important role in charge injection as well as extraction processes. Manipulating the interfacial level alignment and optimizing the energy barriers are thus of high importance for achieving efficient charge injection with minimized energy loss in devices. It has been proved that the interfacial level alignment does not always obey the Schottkey-Mott limit,[62] but mostly a dipole exists on the surface that modifies the surface potential and thus tunes the ELA. In the following it will be shown that how the formation of dipoles is effectively created by forming ordered molecular assemblies; how the surface potential is formed by the created dipoles, and in the last how the surface potential impacts the energy level alignment at interfaces.

2.3.2.1 Self-Assembled Monolayers

Upon the formation of self-assembled monolayers (SAMs), organic molecules are distributed on the surface homogeneously in ordered domains. Thus the formation of SAMs allows to align the surface dipole moment in an ordered manner and modify the surface potential.[63,64] The organic molecule used in the SAM can be considered as

comprising of an anchoring group, a spacer and a tail group. Among them, the anchoring group determines the strength of the interaction between the molecule and the substrate. Depending on different type of anchoring moieties, the molecules adsorb on the surface through either a weak physisorption or a strong chemisorption. For example for phosphonic acid (PA) anchors,[34,65] they can form strong chemical bonds to metal oxides and can lead to a variety of organic monolayers that tune the electronic properties of metal-oxide surfaces. The bond formation mechanism between the PA group and metal oxides can be described in the following:[66]

$$OH - MO + R - PO_3H_2 \longrightarrow R - PO_3H - M + H_2O \qquad (2.25)$$

In the reaction formula 2.25, it is generally known that the surface of metal-oxides is passivated by a layer of hydroxyl groups (-OH). Thus upon the formation of one covalent bond P-O-M at the interface, one water molecule is released. As reported in literatures,[67–69] the above chemical reaction usually forms two or three chemical bonds between the PA and metal-oxide surfaces, which is the so-called bidentate or tridentate bindings. Due to such strong chemical bonding of PA, the molecules can form easily a densely covered monolayer, e.g., for alkyl and aromatic PA molecules, a density of ca. 4 molecules nm^{-1} [34,67] has been observed on zinc-oxide (ZnO) or indium-tin-oxide (ITO) surfaces. Therefore, the PA anchors have been proved to be an effective anchoring group for SAMs and they will also be used in this work for preparing SAMs that containing photoswitches (details of sample preparation can be found in chapter 4.1.3). In contrast, for molecules with pyridine anchors, the formation of SAMs is usually physisorbed on the metal oxides, which is weaker than that of PA SAMs. An example of physisorption of the pyridine group[70,71] is shown in Figure 2.7. Due to weak physisorption, the charge transfer at interface is weaker than that of chemisorption. Thus the surface potential modification in some cases can be mostly originated from the molecular dipole moment.

Regarding the spacer group, a direct understanding about it is that it defines the separation between the anchoring and the tail group. The spacer can play a role in determining the intermolecular interaction between neighboring molecules on the surface; this further impacts the molecular packing densities. Typically, spacer groups are either alkane chains

or conjugated moieties that have specific functionalities. For example, for Py-DHP SAM in Figure 2.7, the spacer group is composed of photochromic moieties, where the frontiers orbitals of the molecule are primarily localized. Therefore, the interfacial frontier level alignment that determines charge injection behaviors can be tuned by the photochromic spacer groups when they are illuminated by light. In the case of the tail group, it is consisted of either an inert capping group or a chemically reactive moiety. Tail groups will determine the surface wettability (hydrophilic or hydrophobic) of the modified surface as well as contribute to a surface potential modification.

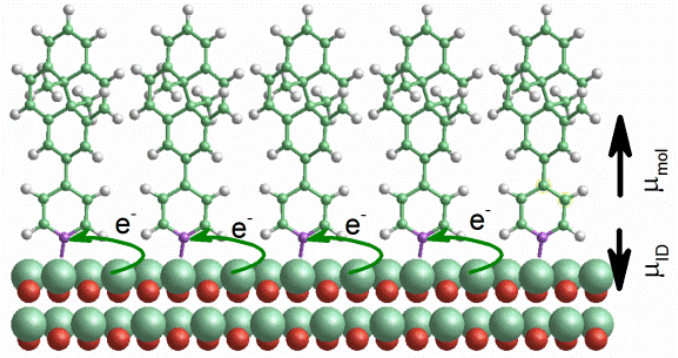

Figure 2.7. Self-assembled monolayer of pyridine based molecules (Py-DHP) chemisorbed on an atomically flat ZnO surface. Due to the adsorption, charge transfer occurs from Zn atoms to pyridine moieties, thus resulting in interface bond dipoles (μ_{ID}) that are perpendicular to the surface. In this ordered monolayer, the presence of molecular dipoles (μ_{mol}) also contributes to the surface potential modification.

Indeed, after SAM modification, the surface potential can be modified[72] due to the formation of an interface bond dipole μ_{ID} and ordered molecular dipoles μ_{mol}. μ_{ID} is formed due to interface charge transfer, while μ_{mol} usually results from permanent molecular dipoles. It is worthwhile to note that the two dipoles can be either in the same direction or in the opposite direction. Thus it is very important to control these two parameters to acquire desired modifications. Furthermore, by controlling the parameters such as immersion time, heating temperature experimentally, one can control the molecular density of the SAM, this also allows modifying the surface for different requirements.

2.3.2.2 Electrostatic Potential Induced by Adsorbates

Interface dipole

Upon adsorption of a monolayer of molecules, a vertical rearrangement of charge distribution will take place at the interface; this leads to an induced dipole moment existing at the interface. Theoretically, the plane averaged charge density ($\Delta\rho(z)$) distribution as a function of z-axis perpendicular to the surface can be derived using the following expression:[73–75]

$$\Delta\rho(z) = \rho_{sys}(z) - \rho_{sub}(z) - \rho_{mol}(z) \tag{2.26}$$

where ρ_{sys} is the charge density distribution of the adsorbed system, ρ_{sub} and ρ_{mol} are the charge density of the bare substrate and the isolated molecular layer, respectively. The redistribution of charges at the interface yields an electrostatic potential change $V_{ID}(z)$ according to Poisson's equation:[76,77]

$$\nabla^2 V_{ID}(z) = -\frac{\Delta\rho(z)}{\varepsilon_0} \tag{2.27}$$

Therefore, the contribution of interface dipole moment to the potential energy change ϕ_{ID} is expressed using the following boundary condition:

$$\phi_{ID} = eV_{ID}(z) - eV_{ID}(z = 0) \tag{2.28}$$

Obviously, the value of ϕ_{ID} is dependent on the direction of net charge transfer. ϕ_{ID} is positive when the net charge transfer is from substrates to molecules, and is negative *vice versa*.

Molecular dipole moments

Organic molecules under the form of SAMs generally adopt an ordered arrangement on the surface of a substrate; this creates a periodic array of intrinsic molecular dipoles. In consequence, the electrostatic potential ϕ_{mol} in z-direction perpendicular to the surface is formed. ϕ_{mol} is given by the Helmholtz equation:

$$\phi_{mol} = -\frac{e\mu_z}{\varepsilon_0 A} = -\frac{en\mu_0}{\varepsilon_0} \tag{2.29}$$

with $\mu_z$the total dipole moment in z-direction, n the number of molecules per unit area. In DFT, the dipole moment of a single molecule μ_0 in the gas phase (here $\mu_0$is assumed to be perpendicular to the surface) can be directly computed. However, when going from single molecule to a monolayer, μ_0 will be reduced due to depolarization effect, namely, the electric field generated by the dipole of a molecule tends to perturb the charge distribution and thus the dipole moments of its neighboring molecules and vice versa.

Such interactions reduce the dipole of the single molecule, which have been treated classically:[78]

$$\mu_{mol} = \mu_0(1 + 9\alpha n^{3/2})^{-1} \tag{2.30}$$

with μ_{mol} and μ_0 the dipole moment of a single molecule in the monolayer and in the isolated state, respectively; α the polarizability of the molecule. Thus equation 2.29 can be rewritten as: $\phi_{mol} = -en\mu_{mol}/\varepsilon_0$. However, this approach describes the dipole moment in a point representation, which works well only when the size of the molecule is smaller than the intermolecular separation.[79] A more practical description of molecular dipole moments is the computation at a quantum mechanical level, which has been largely studied in literatures.[79]

So far, it is concluded that, in the monolayer range, the adsorption induced potential change $\Delta\phi$ can be expressed as (based on Figure 2.7):

$$\Delta\phi \approx \phi_{ID} + \phi_{mol} \tag{2.31}$$

The equation 2.31 works well for most of systems such as SAMs chemisorbed on the substrate, it reflects that interface charge transfer and molecular dipole moments play a very important role in the modification of surface potential. However, the equation is still simplified, since the adsorption process is far more complicated. The adsorption induced push back effect and surface band bending also contribute to the potential change. These will not be the focus of this thesis.

Energy level bending in thick films

After getting familiar with the monolayer adsorptions, it is thus necessary to further discuss the electronic properties in multilayer coverages. Regarding the energy level alignment in multilayers, two different alignment scenarios are typically observed in both molecular and polymeric semiconductors in experiments, that is flat energy levels and band bending (see Figure 2.8).[80,81] Depending on the position of Fermi level of the substrate with respect to the HOMO and LUMO levels of organic layers, charge density distribution $\rho(z)$ in the multilayers can be described as:[82,83]

$$\rho(z) = nq(\int f_H(E)D_H(E + eV(z))dE - \int f_L(E)D_L(E + eV(z))dE) \tag{2.32}$$

Similar to equation 2.19, the above equation 2.32 considers the charge transfer to be related to both a Fermi-Dirac distribution and DOS of frontier levels. The DOS can be simply approximated to a continuous Gaussian profile due to energy splitting of neighboring molecules through mutual electronic interaction and impacts of inherent structural disorders. Note that, the energy shift of frontier levels ($eV(z)$) is also dependent on the transferred charges in the space charge region, which is described with Poisson's equation (see equation 2.27). Therefore, to solve these two equations, one possible approach is described in reference [82], in which $\rho(z)$ is set to a constant (homogeneous charge distribution) as the initial guess, then $eV(z)$ is calculated out based on $\rho(z)$ according to Poisson's equation. With the calculated $eV(z)$ one can find the next $\rho(z)$. This self-consistent process is iterated until the change of $eV(z)$ reaches a convergence.

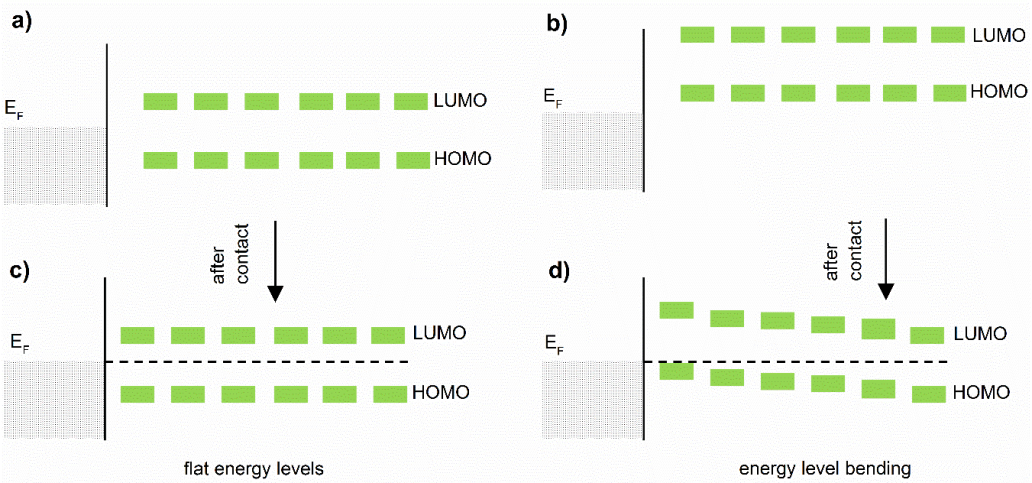

Figure 2.8. Energy level alignment for multilayer coverages. In the case of substrate E_F located inside the gap of organic layers before the contact (Figure a), no obvious charge transfer occurs at the interface after the contact (Figure c); this results in a flat energy level alignment in multilayers. In contrast, when the substrate E_F is located below the HOMO level of organic layers (Figure b), charges are transferred from organic layers to the substrate after the contact, thus leading to a Fermi level pinning at the interface and an energy level bending in the multilayers (Figure d).

Therefore, the energy level alignment in the multilayers can be easily understood based on above-mentioned electrostatic models (equation 2.32 and 2.27): if the E_F of substrate is located in the HOMO-LUMO gap of organic layers, the resulting $\rho(z)$ will be extremely low and nearly a constant with respect to *z*-distance. This leads to a negligible

shift of $eV(z)$, meaning that flat energy levels prevail in the multilayers (see Figure 2.8a, c). However, if the E_F of substrate is located below the HOMO of organic layers (see Figure 2.8b, d), a Fermi level pinning is created at the interface due to a more pronounced charge transfer; such a charge transfer prevails in the multilayers and it forms a space charge region. This leads to an observable potential shift by solving Poisson's equation. The potential shift is translated into an energy level bending in organic multilayers.

2.3.2.3 Vacuum Level Alignment vs Fermi Level Pinning

Based on the above discussions, general interfacial energy level alignment schemes observed experimentally are summarized in Figure 2.9. A commonly observed scenario at the interface is the so-called vacuum level alignment (see Figure 2.9a, also Schottkey-Mott limit);[84] this can be simply understood by considering that the surface potential is not modified after the adsorption of top layers. The underlying mechanism is *i*) according to equation 2.31, the interface bond dipole cancels with the molecular dipole, leading to $\Delta\phi = 0$; *ii*) for a non- or weakly interacted interface, charge transfer is neglected when the Fermi level of the substrate is located in the band gap of top layers. Therefore, the energetic position of organic frontier layers, i.e., HOMO and LUMO with respect to E_F, can be directly derived using the following equation:

$$E_{LUMO} = \phi_{sub} - EA, \;\; E_{HOMO} = IE - \phi_{sub} \tag{2.33}$$

where EA and IE are the electron affinity and ionization energy of organic layers, respectively. It is noted that this model predicts that the positions of E_{HOMO} and E_{LUMO} are linearly proportional to the work function (ϕ_{sub}) of the substrate, which is defined as the energy difference between the vacuum level (E_{vac}) and the Fermi level of the substrate. Thus for the scenario of vacuum level alignment, the energetic positions of the organic frontier levels is possible to be predicted when ϕ_{sub} is known.

Another different scenario is the observation of a Fermi level pining at the interface. As shown in Figure 2.9b and c, there are two different scenarios of level pinning regarding different direction of interface dipoles (ID). In the case of the substrate E_F located above the LUMO of organic layers before the contact, charge transfer will occur from the substrate to organic layers in order to establish a thermal-dynamic equilibrium. As a result,

this gives rise to an ID that shift the vacuum level upwards; this phenomenon is LUMO level pinning.

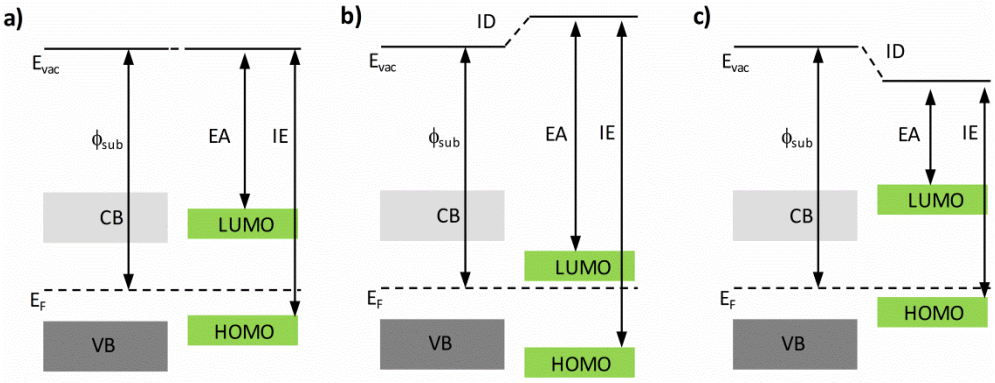

Figure 2.9. Different scenarios of energy level alignments at the hybrid inorganic and organic semiconductor interfaces. a) Vacuum level alignment, b) Fermi level pinning to the LUMO with a positive interface dipole (ID), c) Fermi level pinning to the HOMO with a negative ID. The plotting does not consider energy (band) bending on both sides.

Conversely, when the substrate E_F is located below the organic HOMO energy before the contact, a HOMO level pinning will occur that shift the vacuum level downwards. The pinning of organic semiconductors is commonly observed few of 100 meV away from the HOMO or LUMO level in experiments, and it is an important physical phenomenon regarding applications at the interfaces in a device, since it minimizes the energy barriers for charge injections/extractions.

3. Experimental and Theoretical Methods

In this chapter, the working mechanisms as well as fundamental physics of the experimental setups and theoretical tools that are mainly used in this work will be detailed introduced. Photoemission spectroscopy will be first discussed since it has been mostly used in this work for measuring the electronic properties of photoswitches. Then X-ray absorption spectroscopy (XAS), which is used for measuring the molecular orientation in ordered self-assembled monolayers, will be the next focus. A general introduction of ultraviolet-visible (UV-vis) absorption spectroscopy for determining molecule optical gaps will also be given. For visualizing the surface topography, atomic force microscopy (AFM) will be then introduced. Finally, a brief introduction of density functional theory (DFT) is presented.

3.1 Photoemission Spectroscopy

Photoelectron spectroscopy (PES), which is also known as electron spectroscopy for chemical analysis (ESCA), is currently the most widely used surface analysis technique. With light as an excitation source, it can be used to visualize the occupied electronic structure of atoms, molecules, solids and adsorbates at the surface or interface.[85] Depending on the excitation energy, PES is generally classified into X-ray (e.g., Al K_α light) photoelectron spectroscopy (XPS) and ultraviolet (e.g., He I light) photoelectron spectroscopy (UPS). Among them, XPS is used to detect the core level electrons, while UPS is used to scan the valence electrons, from which information about the frontier molecular orbitals is derived. Conversely, with electrons impinged onto the sample, one can measure the unoccupied electronic structure of molecules by detecting the light signal. This is the so-called inverse photoemission spectroscopy (IPES), since the working principle of IPES is the inverse process of the normal direct PES, thus in the following the main focus will be on introduction of the direct PES.

3.1.1 Working Principle

According to the external photoelectric effect proposed by Einstein, the electrons can be excited out from occupied levels upon illumination of photons when the energy of incident photons is higher than the binding energy (BE) of electrons. Under this condition, electrons enter into the vacuum with a kinetic energy and are finally detected. Figure 3.1a illustrates the process of photoemission and detection of photoelectrons. The sample is placed in an ultra-high vacuum chamber (UHV, base pressure < 10^{-10} mbar) and is irradiated by a (monochromatic) electromagnetic radiation with an energy of hv; then the out-coming electrons excited by the radiation enter into a lens system of the spectrometer. Such electrons are deflected with a fixed pass energy in the hemispherical analyzer (see Figure 3.1a).

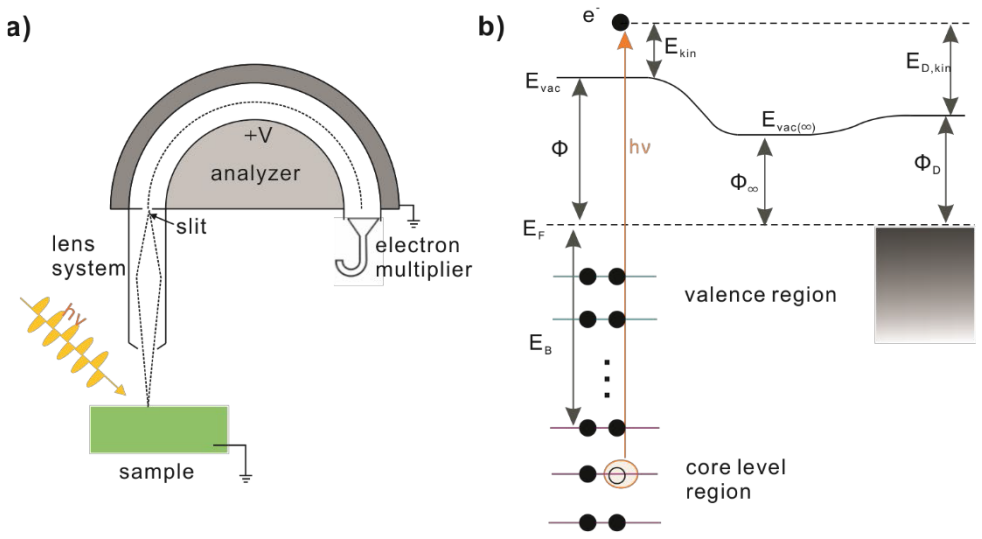

Figure 3.1. a) The experimental setup of the photoelectron spectroscopy. The process of light irradiation, photoemission, electron analyzation and the detection of out-coming electrons are illustrated. b) Excitation of electrons from occupied core level regions upon illumination with a photon energy of hv. The kinetic energy E_{kin} of out-coming electrons is with respect to the vacuum level on the surface, which is not accessible experimentally. The measured kinetic energy for electrons is $E_{D,kin}$.

The voltage applied between the inner and outer hemisphere is for deflecting the electrons, whose trajectory is indicated by a dashed line in Figure 3.1a. After passing through the hemispherical analyzer, electrons are finally collected by a channel electron multiplier

(CEM or channeltron). Principally, the kinetic energy of out-coming electrons satisfies the following equation which abides by energy conservations (shown in Figure 3.1b):[86]

$$E_i + h\nu = E_f + E_{kin} \tag{3.1}$$

where E_i is the energy of the initial states for an N electron system, E_f the energy of the final states of the ionized system (one photon hole is produced due to photoexcitation), E_{kin} the kinetic energy of photoelectrons. According to Koopman's theory,[85] the electron's binding energy on a given orbital can be defined as the energy difference between final state energy E_f and the initial state energy E_i (here the theory adopts a frozen orbital approximation for the final states):

$$E_B = E_f - E_i \tag{3.2}$$

Therefore, inserting equation 3.2 to equation 3.1 gives rise to:

$$E_B = h\nu - E_{kin} \tag{3.3}$$

However, E_{kin} with respect to E_{vac} (here refers to the vacuum level on the surface) cannot be accessible experimentally. The fact is that the kinetic energy of photoelectrons ($E_{D,kin}$) is measured with respect to the vacuum level of a detector (illustrated in Figure 3.1b), since electrons are collected by such a detector. Thus, experimentally E_B (with respect to E_F) is expressed as:

$$E_B = h\nu - \phi_D - E_{D,kin} \tag{3.4}$$

According to equation 3.4, the prerequisite for measuring E_B is to know the work function (ϕ_D) of the detector. Normally, for a measurement with a known excitation source (e.g., He I = 21.2 eV), ϕ_D can be directly determined by measuring the Fermi edge of a metal surface. By detecting the maximum kinetic energy of electrons ($E_{D,kinmax}$), ϕ_D is the given by:

$$\phi_D = h\nu - E_{D,kinmax} \tag{3.5}$$

$$\phi = \phi_D + (E_{D,kin} - E_{kin}) \tag{3.6}$$

It is noticed that the work function of the sample (ϕ) can also be determined as long as E_{kin} is known. A possible way is to collect the scattered secondary electrons whose kinetic energy are zero with respect to the vacuum level on the sample surface. These electrons are non-detectable when the sample is grounded due to that they cannot escape from the

vacuum level of the sample (here the vacuum level means on the surface). However, when applying a negative bias ($U_{bias} > \phi_D - \phi$), the secondary electrons are able to overcome the energy barrier $\phi_D - \phi$ and are finally collected by the detector with kinetic energies of $E_{D,SE}$. Therefore, ϕ is calculated as:

$$\phi = \phi_D + (E_{D,SE} - U_{bias}) \tag{3.7}$$

Equation 3.7 is reformed from equation 3.6. In this photoemission process, the Fermi level of the analyzer is aligned to that of the sample, because they are in contact by being electrically grounded. A typical spectrum measured with He I as an excitation source is shown in Figure 3.2. It can be seen that, at the low kinetic energy (or high binding energy) region, one can observe the secondary electron cut-off (SECO). As electrons in this region are from the vacuum level of the sample, thus by using equation 3.5 and 3.7, the ϕ of the sample can be derived. At the high kinetic (low binding energy) region, the electronic features of occupied states of the sample are visualized. The cut-off region at the high kinetic onset is the HOMO onset of the sample. Loosely speaking, PES reflects the information about the occupied DOS, thus it is possible to derive the electronic properties of organic materials from the PES spectrum, e.g., band structure, HOMO level position. However, the problem is, the measured spectrum can be far more complicated as it is broadened due to a convolution of the setup response function (including broadening of excitation light and analyzer) with the natural distribution of energy states. Furthermore, the spectral intensity is strongly impacted by the electron inelastic mean free path and photon ionization cross section (these will be further discussed later). Thus attentions need to be paid when evaluating or quantifying the measured PES data (this will be discussed later).

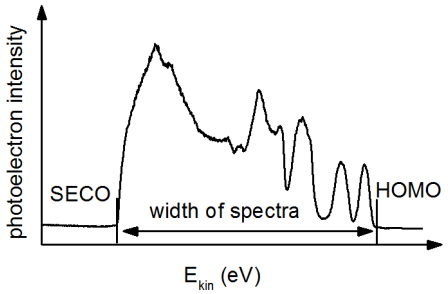

Figure 3.2. Prototypical PES spectrum of an organic film. The spectrum is measured with the excitation of 21.2 eV (He I). The positions of SECO and HOMO level of the film are labeled out in this spectrum.

3.1.2 Theory of the Photoemission Process

The photoemission is a complex process. In order to interpret the experimental spectra, it is necessary to quantitatively compare them with the theoretical calculations. This demand has given rise to the development of various models for calculating the photocurrent in the past decades. The models range from many body theories to single-electron approximations. Among them, the most commonly used model for describing the photoemission process is the so-called three-step model, which is based on a single-electron formulation. The model was originally developed by Berglund and Spicer.[87]

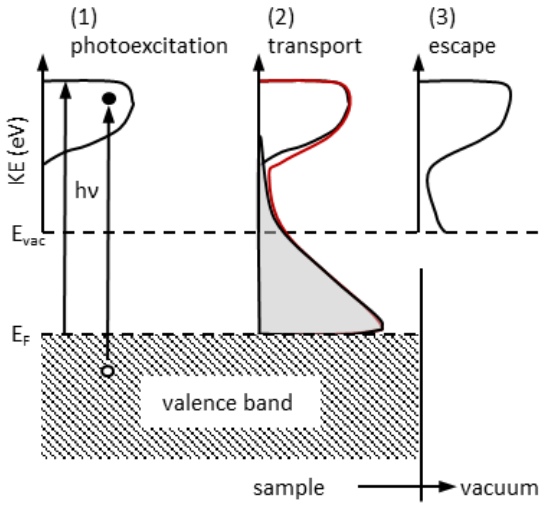

Figure 3.3. Typical three step process of photoemission: (1) photoexcitation of electrons; (2) travel to the surface with concomitant production of secondaries (shaded region) mainly below the vacuum level; (3) penetration through the surface and escape into the vacuum. Figure adapted from reference 85.

Figure 3.3 schematically describes the photoemission process of photoelectrons; the model breaks up the photoemission process of an electron into three steps: *i*) the photoexcitation of an electron in the sample; *ii*) the electron propagates to the sample surface; *iii*) it escapes from the sample to vacuum. In the following section, each step is discussed sequentially in details.

(i) In the photoexcitation process, the electron wave function in the ground states is defined as Ψ_i. After the photoexcitation, the electron is promoted to its final states and its wave function become Ψ_f. Thus the probability of the excitation is described according to Fermi's golden rule:[88]

$$w = \frac{2\pi}{\hbar}\left|M_{if}\right|^2 \delta\left(E_f - E_i - h\nu\right)$$

$$M_{if} = \langle \Psi_f \left| \widehat{H} \right| \Psi_i \rangle \tag{3.8}$$

where M_{if} is the transition Matrix; the delta function in equation 3.8 describes the energy conservation; $\widehat{H}$ is the perturbation operator and its general form can be given under external electromagnetic field irradiations:

$$\widehat{H} = \frac{e}{2m_e c}\left(\vec{A}\cdot\hat{p} + \hat{p}\cdot\vec{A}\right) + \frac{e^2}{2m_e c^2}\vec{A}\cdot\vec{A} \tag{3.9}$$

$$\vec{A} = A_0\vec{e}e^{i\vec{k}\cdot\vec{r}} = A_0\vec{e}(1 + i\vec{k}\cdot\vec{r} + \cdots) \tag{3.10}$$

where $\vec{A}$ is the vector potential of the incident light, which is described by the unitary vector $\vec{e}$ in the direction of light polarization times a complex amplitude of the field A_0; $\hat{p}$ is the momentum operator. Considering one photon process excitation, the last part $\vec{A}\cdot\vec{A}$ becomes negligible since the flux of incident photons is relatively low. $\widehat{H}$ can be further simplified when the wavelength of the incident light is larger than the atomic distances. According to the dipole approximation: $\vec{A} \approx \vec{A}_0 = A_0\vec{e}$, $\widehat{H}$ is finally given by:

$$\widehat{H} = \frac{e}{m_e c}\vec{A}_0\cdot\hat{p} \tag{3.11}$$

For a single atom, the dipole approximation leads to so-called selection rules in the symmetry of photo-emitted electron wave function. Since the operator $\vec{A}\cdot\hat{p}$ represents a polarization of incoming photons, for a given initial states Ψ_i, the transition to final states Ψ_f is only allowed for the states with a particular symmetry $\Psi_i \otimes \vec{E} = \Psi_f$, where $\vec{E}$ is the electric field vector of the incoming photons.

Consequently, the photoexcitation probability w is described as:

$$w = \frac{2\pi}{\hbar}\frac{e^2}{m_e{}^2c^2}\left|\langle \Psi_f \left| \vec{A}_0\cdot\hat{p} \right| \Psi_i \rangle\right|^2 \delta(E_f - E_i - h\nu) \tag{3.12}$$

As discussed above, the probability is limited to the selection rules. Considering that the initial states are in s orbitals, thus for a polarized light source the photoexcitation

probability is the largest when $\vec{E}$ lies in the direction of the final state of the p molecular orbitals. While for a non-polarized light, one does not have to consider this case.

(ii) Regarding the propagation of an excited electron to the surface, it can be scattered either with or without losing its kinetic energy before reaching the surface. Generally, for those whose energy is lost during the scattering will contribute mostly to the background of a spectrum; for those whose energy is conserved during the scattering will be detected in forms of a spectral peak, whose energetic position satisfies equation 3.4 as described above. Therefore, to understand the propagation of electrons in the solid, one important parameter is the probability of electron-electron scattering, which is given by:[89]

$$\frac{d^2\sigma}{dwdq} = \frac{2e^2}{\pi N\hbar v^2} Im\left(\frac{-1}{\varepsilon(w,q)}\right)\frac{1}{q} \tag{3.13}$$

where w is the frequency of the electron; q is the momentum transfer; N is the atomic or molecular density; ε is dielectric constant; Im(-1/ε) is the energy loss function. Note that the scattering probability is dependent on the velocity of electrons and materials dielectric. Another important parameter is the inelastic mean free path (IMFP) λ, which describes how far an electron on average travels in the sample before losing energy. The IMFP determines the information depth that is reached in the PES measurement. As shown in Figure 3.4, according to the equation $I = I_0\exp(-d/\lambda(E))$, one can find that 95% of signal is from the thickness of 3λ.

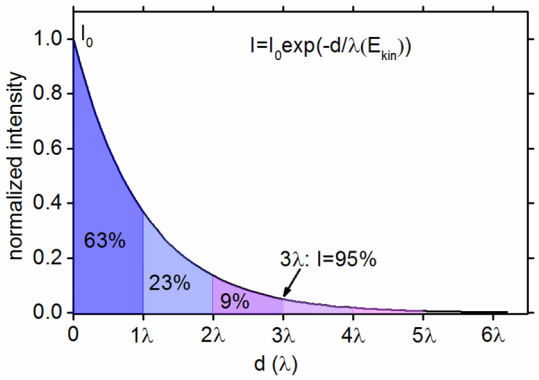

Figure 3.4. Evolution of the spectral intensity with respect to the signal information depth. The function is shown in the inset of the Figure. As one can see that 95% of signal has already been detected when the signal depth is 3λ.

A universal curve of IMFP has been summarized as a function of electron kinetic energy by measuring inorganic metals.[90] The data show that, for electrons with kinetic energies ranging from 10 eV to 2000 eV, λ is only of the order of a few Å. This means that PES

measurements on a solid sample are highly surface sensitive. However, a precise determination of λ is still difficult since it depends on both the kinetic energy of electrons and the property of materials, such as density, band gap, elements. A semi-empirical formula is used in this thesis in dealing with the quantification of XPS, that is the TPP-2M equation:[91]

$$\lambda = \frac{E_{kin}}{E_P^2[\beta \ln(\gamma E_{kin}) - (C/E_{kin}) + (D/E_{kin}^2)]} \quad (3.14)$$

where $E_{P=}\sqrt{28.8(N_V\rho/M)}$ is the free-electron plasma energy in eV; N_v is the number of valence electrons per atom; M is the atomic weight; r is the density and E is the electron energy. Values of the parameters b, g, C, and D were obtained from fitting to the computed IMFPs.

(iii) In the 3rd step, the electron escapes from sample surface, and it will be analyzed and collected by the spectrometer. As shown in Figure 3.5, for electrons that are capable of escaping from the surface, they have to satisfy the following condition:

$$\frac{\hbar^2 K_\perp^2}{2m_e} \geq E_{vac} - E_i \quad (3.15)$$

with m_e the free electron mass, $K_\perp$ the component of wave factor of an excited electron normal to the surface, E_{vac} the vacuum level, and E_i the initial state of an electron. Other electrons which do not satisfy equation 3.15 will be reflected back into the bulk. Thus this results in a minimum $K_\perp$ of $\sqrt{2m_e(E_{vac} - E_i)}/\hbar$.

While regarding the wave vector of an electron parallel to the surface ($\vec{K}_{||}$), it is conserved after entering into the vacuum. Therefore, according to the free electron model, the momentum component of an escaped electron ($\vec{p}$) parallel to the surface is expressed as:

$$\frac{\vec{p}_\parallel}{\hbar} = \vec{K}_\parallel = \vec{k}_\parallel$$

$$k_\parallel = \sin(\theta)\sqrt{\frac{2m_e E_{kin}}{\hbar^2}} = \sin(\theta')\sqrt{\frac{2m_e(E_f - E_i)}{\hbar^2}} \quad (3.16)$$

Equation 3.16 states the escape direction of an electron. This means that, there exists a maximum θ' that allows electrons to escape with only its $K_{||}$ component, i.e., θ=90°. The maximum θ' for the electron in its final states is:

$$\sin(\theta'_{max}) = \sqrt{\frac{E_{kin}}{E_f - E_i}} \tag{3.17}$$

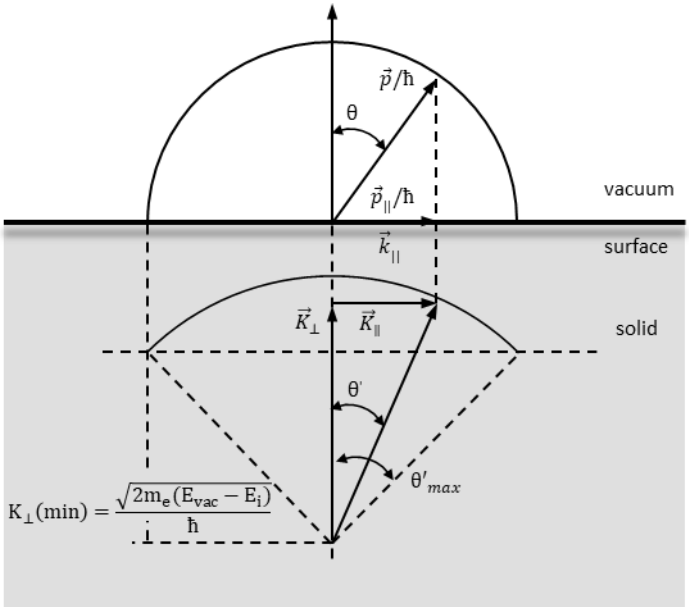

Figure 3.5. Escape cones of out-coming electrons. For the electrons going to the vacuum, the momentum parallel to the surface is conserved. The picture also shows that electrons only with an angle smaller than θ'max can escape from the solid to the vacuum. Figure is adapted from reference 85.

In equation 3.17, it indicates that electrons with an angle smaller than θ'_{max} can escape out of the sample. Otherwise, they cannot escape. Furthermore, combining $K_{||}$ with $K_{\perp}$, E_{kin} can be calculated: $E_{kin} = E_f - E_{vac}$.

Regarding the collection process by the spectrometer, the collection efficiency is described by the transmission function $T(E_{kin})$ of the spectrometer, which is dependent on several instrumental parameters, such as acceptance area, acceptance angle and detect efficiency. Finally, the external photoemission intensity is related to the whole process of the electron from photoexcitation to detection.

3.1.3 Qualitative Analysis of Spectra

Normally, for a recorded PES spectrum, its binding energy is calibrated, that is, the Fermi level is at zero binding energy. However, when a sample is poorly conductive or insulative, charging effect will prevail. In this case, specific attentions need to be paid for the calibration. One possible method is to use the energetic position of adventitious

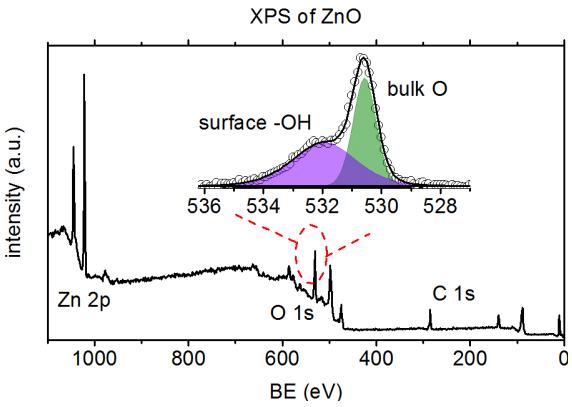

Figure 3.6. Prototypical XPS survey spectrum of a ZnO surface. From which different elements are resolved. Inset: Zoom-in of the O 1s core level spectrum, from which one identifies that there are two different oxygen components with different peak widths existing on the surface.

carbon as a reference, whose energy is at 284.8 eV BE for hydrocarbons.[92] While regarding a calibrated spectrum, one can get the information about both core level and valence level electrons. A typical spectrum is of XPS is shown in Figure 3.6: the survey measured with an Al K_α X-ray ranges from 1200 eV to 0 eV; the sharp peaks shown in the spectrum are primary electrons collected without losing their kinetic energies from different elements, i.e., C, O, and Zn. Therefore, one of the important functions for XPS is to identify elemental components in a sample. It is noted that there is a significant background beneath the survey spectrum. This is primarily caused by electrons that are inelastically scattered before leaving the sample surface. Such a scattering reduces the kinetic energy of electrons, and thus contributes to the spectral background. It is usually necessary to subtract the background in order to analyze the desired peak. There are several different types of background subtraction (Linear, Shirley, Touggard) methods that will be discussed in details in the data processing part. Furthermore, by taking a narrow scan on one specific core level, it is possible to determine the chemical composition (or chemical shift) of a specific element in the sample due to different energetic positions and peak intensities. For example, in the inset of Figure 3.6, one can identify multiple chemical components in the O 1s peak upon spectral fitting: the one with a higher binding energy is assigned to surface hydroxyl groups, while another profile is assigned to bulk oxygen atoms.[93–95]

3.1.4 Quantification of XPS Data

3.1.4.1 Photoemission from a Homogeneous Film

As mentioned in the last section, one of the merits of XPS is the identification of chemical composition in an unknown sample, while quantifying the XPS data is also of high importance for analyzing the content of different elements or estimating molecular surface coverages. To do this, it is necessary to recall the abovementioned three-step model, which describes in details the photoemission process. Based on that model, the photoemission signal (denoted as peak area) of a specific element in a homogeneous film can be described by the following formula:[96]

$$I_0 = n \cdot f_{ph} \cdot \sigma \cdot \lambda \cdot T(E_{kin})\cos(\theta) \tag{3.18}$$

where I_o denotes the background subtracted photoemission intensity. It is not difficult to understand that I_o is mainly dependent on the density of elements (n), incident photon flux (f_{ph}), photoionization cross-section (σ), electron inelastic mean free path (λ), spectrometer intensity/energy response function (also called transmission function $T(E_{kin})$, and acceptance angle (θ), since these parameters are closely related to the photoemission process. Assuming that the measurements are performed with a stable photon flux and a fixed acceptance angle, thus the measured signals for different elements (elements A, B) are only dependent on the following several factors:

$$\frac{I_A}{I_B} = \frac{n_A \cdot \sigma_A \cdot \lambda_A \cdot T(E_{A,kin})}{n_B \cdot \sigma_B \cdot \lambda_B \cdot T(E_{B,kin})} \tag{3.19}$$

Based on equation 3.19, it is possible to estimate the element ratios of A to B by knowing their relevant three parameters (i.e., λ, $T(E)$, σ). The estimation of λ relies on the TPP-2M equation (*vide supra*);[91] The spectrometer transmission function can be measured with the bias method.[97] However, when the kinetic energies of electrons from two different elements are close to each other (BE are energetically close), the impacts of $T(E)$ can be neglected since the intensity/energy response is almost the same. Regarding σ, the probability of photoionization to an ionic state is proportional to the photoionization cross-section [$\sigma(h\nu) = f_{absorb}(h\nu)/f_{incident}(h\nu)$]. Normally, in one atom, when more than one orbital level is excited, the cross-section can be written as: $\sigma = \sum_{nl} \sigma_{nl}$, where

σ_{nl} is the partial photoionization cross-section in the subshell. In a PES spectrum, electrons from a subshell excitation are usually collected at a specific angle. Thus σ_{nl} can be written in a differential form:[98]

$$\frac{d\sigma_{nl}}{d\Omega} = \frac{\sigma_{nl}}{d\Omega}[1 - \frac{\beta}{2}P_2\cos(\theta) + (\frac{\gamma}{2}\sin^2(\theta) + \delta)\cos(\theta)] \quad (3.20)$$

where $\frac{d\sigma_{nl}}{d\Omega}$ is called differential cross section, β is the asymmetry factor for photoelectron angular distribution, θ is the angle between the vectors of photons and the photoelectron propagation, and $P_2\cos(\theta)$ is the second order Legendre polynomial. Note that equation 3.20 is only for circularly polarized and unpolarized photons; more detailed consideration of the polarization of photons can be found in literatures.[98,99] Therefore, to be more precise, equation 3.18 for a subshell excitation is rewritten as:

$$I_0 = n \cdot f_{ph} \cdot \frac{d\sigma}{d\Omega} \cdot \lambda \cdot T(E_{kin})\cos(\theta) \quad (3.21)$$

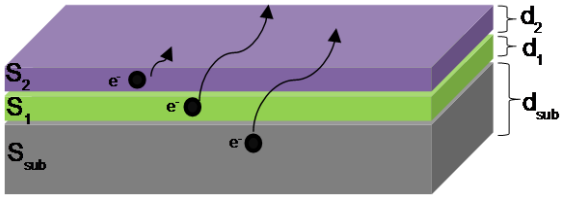

Figure 3.7. Illustration of the out-coming photoelectrons from a multilayer structure composed of S_1, S_2 layers and a substrate. For electrons coming from the substrate, they undergo attenuations by both S_1 and S_2; for electrons coming from S_1, they undergo attenuations only by S_2.

3.1.4.2 Photoemission from Multiple Layers

Regarding a multiple-layer system (as illustrated in Figure 3.7), the photoemission process from buried layers is inevitably attenuated by the top layer. Thus an exponential decay of photoelectrons has to be considered to the measured signal intensity. Such a decay is dependent on both the thickness (t) of the top layers and the IMFP of photoelectrons in the top material. Typically, the measured signal intensity for a thin film with a finite thickness measured by PES is described as:

$$dI = I_o \cdot exp(-t/\lambda cos(\theta))dt \quad (3.22)$$

where I_o is the intensity of the film with an infinite thickness. Therefore, for the top layer S_2 (see Figure 3.7), its peak intensity is calculated by integrating the thickness from zero to d_2 in equation 3.22; this gives rise to:

$$I_2 = I_{o,S_2}[1 - exp(-d_2/\lambda_2\cos(\theta))] \quad (3.23)$$

However, for the middle and bottom layers S_1 and S_{sub}, each of them is attenuated by top layers, thus one has to subtract the attenuated components in the calculation of intensities. The following gives the peak intensities for S_1 and S_{sub}, respectively:

$$I_1 = I_{o,S_1}[1 - exp(-d_1/\lambda_1\cos(\theta))]exp(-d_2/\lambda_{1,2}\cos(\theta)) \quad (3.24)$$

$$I_{sub} = I_{o,sub}exp(-d_1/\lambda_{sub,1}\cos(\theta))exp(-d_2/\lambda_{sub,2}\cos(\theta)) \quad (3.25)$$

By taking such attenuations into consideration, equations 3.23-3.25 are commonly used for determining the overlayer thickness and coverages. Further applications will be found in the results and discussion part.

Error analysis in XPS quantification

It should be aware that, the quantification of XPS data always gives uncertainties that are contributed by several factors, e.g., homogeneity of the distribution of corresponding atoms, IMFP of the photoelectrons λ, photoionization cross section σ,[100] analyzer transmission function *T(E)*…. Considering all the deviations given by each component, the total error of XPS quantification is expressed as:

$$\frac{\delta N}{N} = \sqrt{(\frac{\delta\lambda}{\lambda})^2 + (\frac{\delta\sigma}{\sigma})^2 + (\frac{\delta T(E)}{T(E)})^2 + \cdots} \quad (3.26)$$

The truth is that the final error is as high as 30% even only considering the deviations of λ and σ. Generally, λ is unknown and can only be estimated in theory; the TPP-2M formula for estimating λ shows an average root-mean-square deviations of ca. 20%.[91] For the partial photoionization cross section, a normal deviation of larger than 10%[100100] is usually considered. Therefore, one has to be careful when quantifying the XPS data. The error can be even higher for a spectrum with badly fitting procedures or unknown transmission function.

3.2 Absorption Spectroscopy

3.2.1 X-ray Absorption Spectroscopy

X-ray absorption spectroscopy (XAS) is widely employed to investigate the chemistry and structure of samples.[101] Upon X-ray irradiation, the inner shell excitation process of an atom is triggered when the photon energy is close to the atomic absorption edge. The inner shell to unoccupied level transition creates a resonant peak in the absorption spectrum that is generally composed of two parts: *i*) near edge X-ray absorption fine structure (NEXAFS, absorption features up to 30 eV above the absorption edge); *ii*) extended X-ray absorption fine structure (EXAFS), which can extend up to 1000 eV above the absorption edge. The working mechanism of XAS is schematically depicted in Figure 3.8. Upon light irradiation with an energy of *hv*, electrons in the core levels absorb the photons. The absorption process induces a transition of a K-shell electron into the unoccupied energy states. This transition obeys strictly dipole selection rules, that is: $\Delta l = \pm 1, \Delta j = \pm 1, \Delta s = 0$, where *l* is the angular momentum quantum number; *j* is the total momentum quantum number and *s* is the spin quantum number. Thus for K-edge excitations, the dipole transition should be from an initial *s* state to a final-state orbital that have a *p* angular momentum.

By gradually increasing the incident photon energy, the continuum or quasi continuum of final states is recorded due to the transition of electrons.[102–104,104] As shown in the right panel of Figure 3.8, the unfilled molecular orbitals are labeled as π^* and σ^* states. The absorption edge is usually found at the lowest unoccupied molecular orbital of a π-bonded molecule, that is a π^* orbital, while the σ^* is often found at higher energy levels, sometimes even above the vacuum level for a neutral molecule. The spectral intensity is proportional to the X-ray absorption cross section ($\sigma_{X\text{-}ray}$), for a single electron in the dipole approximation, $\sigma_{X\text{-}ray}$ can be described using Fermi Golden Rule:

$$\sigma_{X-ray} = \frac{4\pi^2\hbar^2}{m_e^2}\frac{e^2}{\hbar c}\frac{1}{h\nu}\langle\Psi_f|\vec{e}\cdot\hat{p}|\Psi_i\rangle^2\rho_f(E) \qquad (3.27)$$

where Ψ_f and Ψ_i are the wave functions of the final and initial states, respectively. Here the final states are electrons in the bounded or continuum states. $\vec{e}$ is the unit electric field vector, $\hat{p}$ is the dipole transition operator of the light, ρ_f is the density of final states.

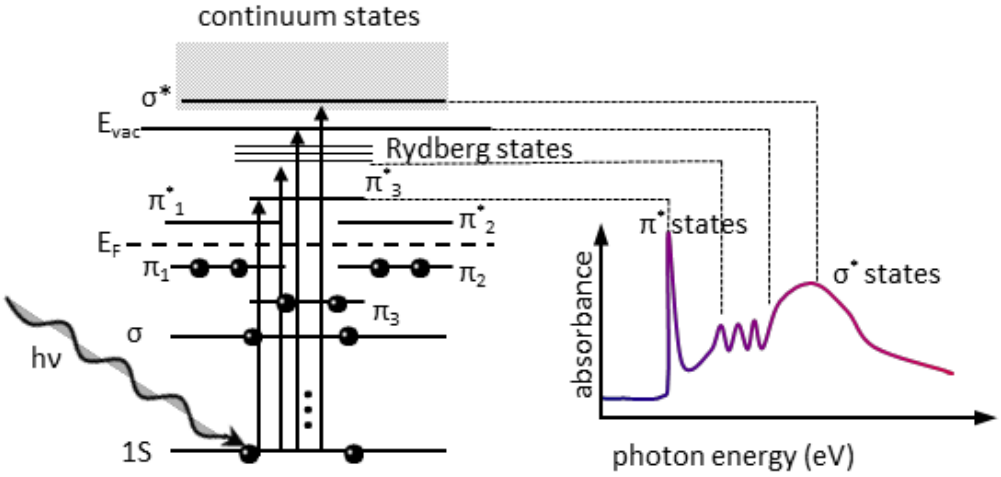

Figure 3.8. Schematic illustration of molecular electronic levels (left) and corresponding XAS K-shell spectrum (right). With X-ray irradiation, electrons from the 1s orbital are excited to unoccupied states, i.e., π^*, σ^* and Rydberg states. Thus the absorption is reflected in the spectrum, as shown in the right figure. The absorption width of unoccupied states is related to the life time of electrons in the states. Figures are adapted from reference 107.

Regarding XAS measurements, there are several ways of obtaining a XAS spectrum, such as total electron yield (TEY), Auger electron yield (AEY) and partial electron yield (PEY), etc. While the method used in the present work is the TEY mode, which measures all electrons (Auger electrons and secondary electrons) by monitoring the sample drain current. The TEY mode involves several inelastic scattering events of photoelectrons. Electrons created deeper in the sample lose too much energy to overcome the work function of the sample and therefore do not contribute to the TEY. The sampling depth in TEY measurements is typically a few nanometers, whereas it is often less than 1 nm for AEY measurements.

Angular Dependent X-ray Absorption

One of the merits of XAS spectroscopy is that it can measure the molecular orientations by performing angle-dependent XAS measurements. Linearly polarized X-rays are best suitable sources for determining the orientation of covalent systems like low-Z molecules, macromolecules and polymers, all of which possess directional bonds. In this case, the

directional electric field vector of X-rays allows for probing the direction of chemical bonds of the atom selected by its absorption edge. By taking XAS measurements at different angles, the spatial orientation of an unoccupied orbital, e.g., π^* or σ^* orbital, can be extracted. Before the discussion of angular dependence of the core shell excitation, it is important to divide molecules into general groups. Figure 3.9 shows diatomic molecules and aromatic groups with four different types of orbitals.[105] Depending on the chemical bonding, the spatial orientation of π^* and σ^* orbitals can be either vector-like or planar-like. For example, for an aromatic ring (Figure 3.9d), its atoms are arranged in a plane, and thus its σ^* system is characterized in the plane. The π^* orbitals are however represented by vectors perpendicular to the plane. Conversely, for a triple bond system, the σ^* orbital is vector type and π^* orbital is planar type due to the two orthogonal orbitals of each atom.

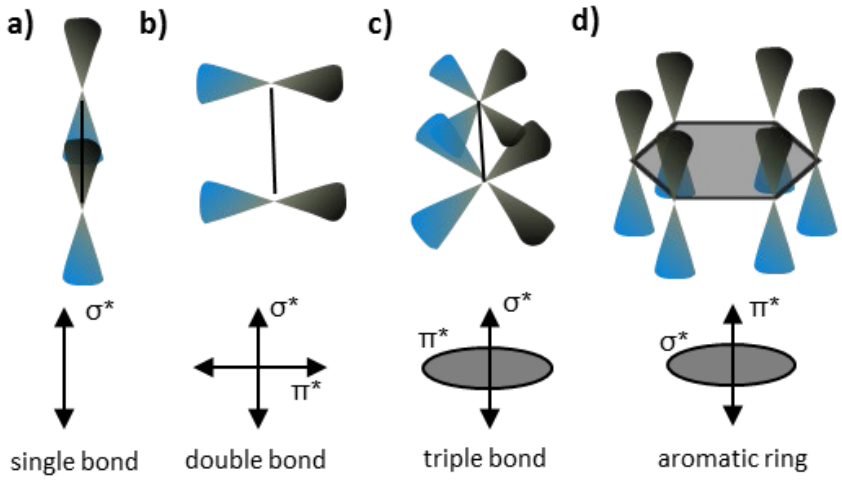

Figure 3.9. Spatial orientation of π^* and σ^* orbitals for molecules in a) single bond, b) double bond, c) triple bond, d) aromatic ring groups. The direction of π^* and σ^* orbitals is indicated below each figure, where molecular orbitals are divided into vector-type and plane-type. The figures are adapted from reference 106.

Therefore, the angular dependence of the resonance needs to be considered in two cases: *i*) vector type π^* and σ^* orbitals; *ii*) plane-type π^* and σ^* orbitals. Figure 3.10 displays the absorption of a typical plane-type orbital. Likewise, one can also replace the plane with a vector to deduce the vector-type absorption. The resonance intensity linked to the initial and final states in a matrix form is:[105,106]

$$I \propto \langle \Psi_f | \vec{e} \cdot \hat{p} | \Psi_i \rangle^2 \tag{3.28}$$

Equation 3.28 is reformed according to the vector- and plane-type orbitals:

$$I_v = A\cos^2\delta,\ I_p = B\sin^2\varepsilon \tag{3.29}$$

where *A* and *B* describe the angular integrated cross-section; ε and δ are the angle between the electric field (E) and the surface normal (N) for the plane- and vector-type orbitals, respectively. In practice, the incident X-ray beam in the (*x, z*) plane is not perfectly polarized (see Figure 3.10 a), resulting in an $E_{\parallel}$ component in the (*x, z*) plane and a weaker $E_{\perp}$ component in the (*y, z*) plane. The degree of linear polarization factor *P* is given by:

$$P = \left|E_{\parallel}\right|^2 / (\left|E_{\parallel}\right|^2 + |E_{\perp}|^2) \tag{3.30}$$

Thus the measured resonance intensity is composed of two parts:

$$I = C[PI_{\parallel} + (1-P)I_{\perp}] \tag{3.31}$$

where $I_{\parallel}$ and $I_{\perp}$ are the intensities in the $E_{\parallel}$ and $E_{\perp}$ planes, respectively. Their magnitudes are related to the spatial orientation of orbitals and the X-ray incident angle (θ). It is not difficult to find that $I_{\perp}$ does not depend on θ since $E_{\perp}$ is fixed in the *y*-axis direction. To precisely determine the angular dependence of resonance intensities of $I_{\parallel}$ and $I_{\perp}$, one has to consider the azimuthal angle and the symmetry of the substrate.

As shown in Figure 3.10a, the angular dependence of absorption intensities are not only related to the molecular tilt angle, but also to the azimuthal angle Φ. However, in some cases the azimuthal angle can be eliminated due to the symmetry of substrates. A detailed discussion on the surface symmetry for XAS can be found in some literatures.[105–107] Here, the focus is put on the quantification of molecular orientation based on different substrate symmetries.

Generally, for a two-fold or higher substrate symmetry, the resonance intensities for both vector- and plane-type of orbitals are summarized in equation 3.32. It is noted that the resonance intensity is still dependent on the azimuthal angle Φ. However, for a three-fold or higher substrate symmetry, such as a DHP molecule on the ZnO substrate (see Figure 3.10b), the contribution of Φ is neglected due to a 6-fold symmetry of ZnO. Thus the

resonance intensities are independent of the azimuthal angle Φ, but rather on the molecular orientation and photon incident angle (see equation 3.33).

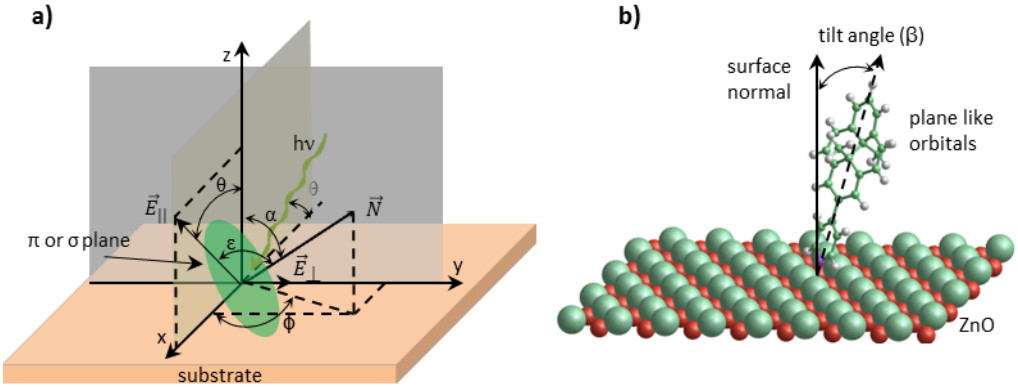

Figure 3.10. a) Coordinate system defining the geometry of a plane-type orbital. The orientation of the orbital is characterized by a polar angle α and an azimuthal angle Φ. The X-ray is incidence in the (x,z) plane which contains the major electric field vector component $E_{||}$. The X-ray incidence angle θ, which is also the polar angle of $E_{||}$, is changed by rotating the crystal about the y axis. The weaker component $E_{\perp}$ lies in the surface plane, along the y-axis. The z-axis is the surface normal and the azimuthal rotation axis of the crystal. b) Prototypical tilt angle of a DHP molecule adsorbed on the ZnO surface; its tilt angle (β) is defined as the angle between the surface normal and the axis along the molecular backbone.

Two fold or higher substrate symmetry:

$$\begin{aligned} I_v^{||} &= A(\cos^2(\theta)\cos^2(\alpha)+\sin^2(\theta)\sin^2(\alpha)\cos^2(\phi)) \\ I_v^{\perp} &= A\sin^2(\alpha)\sin^2(\phi) \\ I_p^{||} &= B(1-\cos^2(\theta)\cos^2(\alpha)-\sin^2(\theta)\sin^2(\alpha)\cos^2(\phi)) \\ I_v^{\perp} &= B(1-\sin^2(\alpha)\sin^2(\phi)) \end{aligned} \tag{3.32}$$

Three fold or higher substrate symmetry:

$$\begin{aligned} I_v^{||} &= A(\cos^2(\theta)\cos^2(\alpha)+0.5\sin^2(\theta)\sin^2(\alpha)) \\ I_v^{\perp} &= 0.5A\sin^2(\alpha) \\ I_p^{||} &= B(1-\cos^2(\theta)\cos^2(\alpha)-0.5\sin^2(\theta)\sin^2(\alpha)) \\ I_v^{\perp} &= 0.5B(1+\cos^2(\alpha)) \end{aligned} \tag{3.33}$$

In this work, the measured π^* states of our molecules, such as DAE photoswitches, exhibit a vector-type resonance and the employed substrates (e.g., ZnO, ITO) adopt a 6-fold

symmetry. Thus by measuring the angular dependence XAS on molecules, the absorption intensity can be fitted with a combination of equation 3.31 and 3.33.

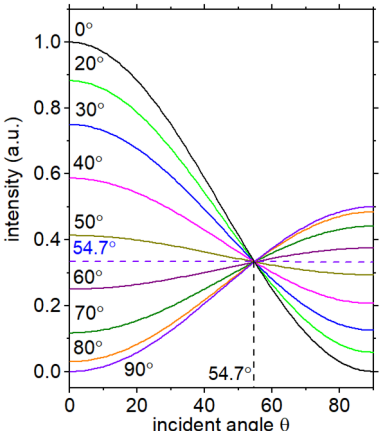

Figure 3.11. X-ray absorption resonance intensity for various polar tilt angles of a vector-orbital as a function of the incident angle θ, as described in Figure 3.10. The plotting is based on the polarization factor P with its value P=1. One can see that at 54.7°, there is not intensity change upon increasing the incident angles; the orientation of 54.7° is the so-called "magic angle".

A typical theoretical description of angle-dependent vector-type orbitals (see equation 3.33) is shown in Figure 3.11. Assuming an incident light is 100% linearly polarized ($E = E_{\parallel}$), one can observe that the resonance intensity of a vector-type orbital with its orientations ranging from 0° to 90° exhibits an angular dependence. This figure also displays the special role of the "magic angle" of 54.7°. For the distribution of molecules with their average orientation of 54.7°, all resonance intensities are independent of the incidence angle θ of X-rays. Likewise, when the incident angle of X-ray is at 54.7°, the resonance intensity is independent of the orientation of molecules.

3.2.2 Ultraviolet-visible Spectroscopy

Similar to the abovementioned X-ray absorption, the ultraviolet-visible (UV-vis) absorption spectroscopy is also related to light-matter interactions. However, in UV-vis spectroscopy, electronic transitions primarily occur in the frontier level of molecules. There are generally four types of electronic transitions involved in this process, that is *i)* σ to σ^* transition; *ii)* π to π^* transition; *iii)* n to π^* transition; *iiii)* n to σ^* transitions (see Figure 2.1 for energy levels). The working principle of UV-vis spectroscopy follows the Beer-Lambert law. The law states that whenever a beam of monochromatic light passes through a solution with an absorbing substance, the decreasing rate of the radiation intensity along with the length of the absorbing solution is proportional to the

concentration of the solution and incident radiation. The expression of the law is given by:

$$A = \log\left({}^{I_0}/_{I}\right) = \epsilon(\lambda)CL \tag{3.34}$$

where A stands for the absorbance; I_0 is the intensity of light upon a sample cell; I refers to the intensity of light departing the sample cell; C is the concentration of the solute; L stands for the length of the sample cell and $\epsilon(\lambda)$ refers to the extinction coefficient. Based equation 3.34, the UV-vis gives the information about molecular optical properties and it allows us to measure the lowest optical transitions, from which one can derive the optical gap of molecules. This is particularly important regarding the present work.

3.3 Atomic Force Microscopy

The Atomic Force Microscopy (AFM) is a kind of scanning probe microscopy in which a topographical image of the sample surface is visualized based on the van der Waals interactions between a tip and a sample surface. AFM was invented by Binning and his colleagues in 1986[108] at IBM Zurich based on the scanning tunneling microscope (STM) that was already presented in 1981. The main advantage of AFM compared to STM is that it can visualize the surface of non-conductive samples. Figure 3.12a displays the typical working principle of an AFM setup, which is composed of five components: a laser, a photodiode detector, a cantilever with a tip, a piezo scanner and a feedback loop. When the tip moves on the surface, the tip-sample interactions are monitored by the reflection of a laser beam, and finally the signal of the tip movement on the surface is detected by a photodiode. The tip-sample interactions[109,110] (Figure 3.12b) can be described by *van der Waals* forces (see equation 2.21), because of which, there are many operation modes of AFM, e.g., contact modes, tapping modes and non-contact modes. In this work the tapping AFM is of main interest.

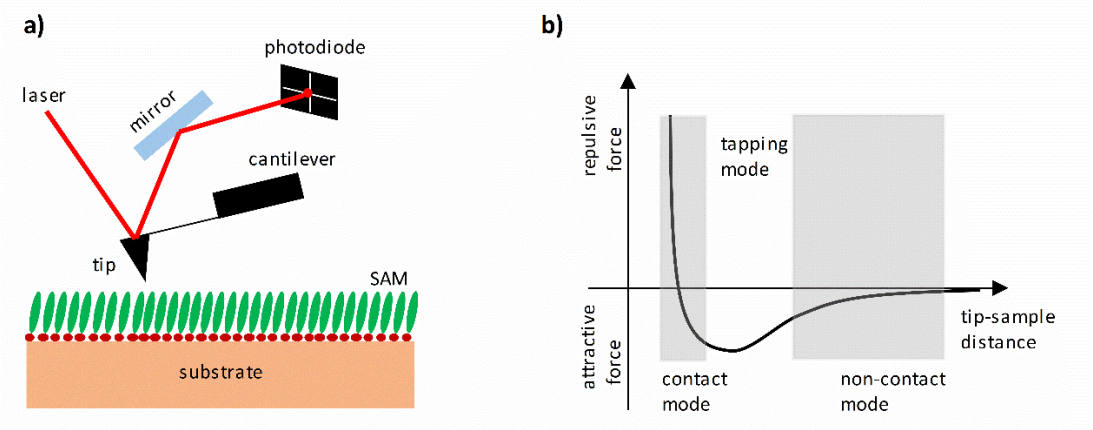

Figure 3.12. a) Schematic diagram of the basic working principle of AFM. During the measurement, the tip moves on the sample surface, and the signal change caused by the surface topography can be monitored by a laser beam, which is finally detected by a photodiode. b) Plotting of the force as a function of tip-sample distance. Figures are adapted from reference 109 and 110.

The tapping AFM is an important AFM technique, as it overcomes some of the limitations of contact AFM. By eliminating lateral forces that can distort or damage samples, Tapping AFM allows routine imaging of delicate and soft samples, as well as samples that are weakly attached to a substrate, that are often difficult to image in contact AFM. Moreover, it can be performed both in air and fluid. Regarding the working mechanism of tapping AFM, it is described in the following: a piezo excites the cantilever substrate vertically, which causes the cantilever to oscillate vertically. Due to such an oscillation, the reflected laser beam deflects in a regular pattern over a photodiode detector and generates a sinusoidal, electronic signal or "detector signal". Before the AFM tip is engaged on the sample, the cantilever oscillates in free air with the frequency close to its resonant frequency. As the probe approaches and encounters the sample surface, the amplitude of this oscillation usually decreases. By monitoring changes in amplitude and continuously feeding back on a user-specified amplitude setpoint, the tip moves up and down to maintain constant oscillation amplitude. By this means, a high-resolution three-dimensional image of the sample surface topography is obtained.

Kelvin probe force microscopy

Based on AFM techniques, the Kelvin Probe Force Microscopy (KPFM) gives information not only about the surface topography but also the surface contact potential difference (CPD). The CPD (V_{CPD}) between the tip and sample is defined as the following:

$$V_{CPD} = (\phi_{tip} - \phi_{sample})/-e \tag{3.35}$$

where ϕ_{tip} and ϕ_{sample} are the work functions of the tip and sample, respectively; e is the elementary charge. According to equation 3.35, ϕ_{sample} can be measured if ϕ_{tip} is known.[109] The underlying mechanism is that: V_{CPD} is created between the tip and the sample after they contact, since they have different work functions. Such a potential difference can be monitored by applying an external bias. When the amount of the bias equals V_{CPD}, the potential difference is thus mapped. With KPFM, one can map the local potential difference on the surface; this is complementary to the method of PES.

3.4 Density Functional Theory

Theoretical calculations in this thesis are performed at the Density Functional Theory (DFT) level. In the following, a brief overview about the central aspects of DFT as well as its approximations and methods for the resolution of DFT will be introduced.

3.4.1 Many Body Schrödinger Equation

In quantum mechanics, the electronic structure of an *N*-electron system is described by Schrödinger equation, thus the final goal of the quantum chemical analysis is to solve the time-independent Schrödinger equation for an *N*-electron system, whose form is given by:

$$\widehat{H}\Psi(r_1,...r_N,R_1,...R_n) = E\Psi(r_1,...r_N,R_1,...R_n) \tag{3.36}$$

where Ψ is the wave function of the total system including *N* electrons and *n* atomic nuclei; $\widehat{H}$ is the Hamilton operator for a molecular system and it can be described as:

$$\widehat{H} = -\frac{1}{2}\sum_i \nabla_i^2 - \frac{1}{2M}\sum_I \nabla_I^2 - \sum_i\sum_I \frac{Z_I}{|r_i - R_I|} + \frac{1}{2}\sum_{i\neq j}\frac{1}{|r_i - r_j|} + \frac{1}{2}\sum_{I\neq J}\frac{Z_I Z_J}{|R_I - R_J|} \tag{3.37}$$

Here, the first two terms represent the kinetic energy of the electrons and nuclei, respectively. The remaining three terms are the potential part of electron-nuclear, electron-electron, and nuclear-nuclear interactions. However, the problem is that the

operator $\hat{H}$ is too complicated to calculate its eigenstates and eigenvalues. A practical way is to consider the electrons as moving in the field of fixed nuclei, since the nuclei move much slower than electrons due to their relatively larger mass ratio. Thus $\hat{H}$ is simplified according to a Born-Oppenheimer approximation and is given by:[111]

$$\hat{H}_{ele} = \overbrace{-\frac{1}{2}\sum_i \nabla_i^2}^{\hat{T}} \overbrace{-\sum_i \sum_I \frac{Z_I}{|r_i - R_I|}}^{\hat{V}_{ext}} + \overbrace{\frac{1}{2}\sum_{i \neq j} \frac{1}{|r_i - r_j|}}^{\hat{V}_{ee}} \tag{3.38}$$

In equation 3.38, the kinetic operator of nuclei is neglected, and the potential operator due to nucleus-nucleus repulsion is merely a constant. Thus $\hat{H}_{ele}$ is dependent on the position of electrons relative to nuclei. Consequently, the solution of the Schrödinger equation with $\hat{H}_{ele}$ becomes the electronic wave function $\psi(r,R)$ and electronic eigenvalues E_{ele}. The total energy is then the sum of E_{ele} and the constant nuclear repulsion term E_{nuc}.

$$\begin{aligned} &\hat{H}_{ele}\psi(r,R) = (\hat{T} + \hat{V}_{ext} + \hat{V}_{ee})\psi(r,R) = E_{ele}\psi(r,R) \\ &E_{tot} = E_{ele} + E_{nuc}, \qquad E_{nuc} = \sum_{I \neq J} \frac{Z_I Z_J}{|R_I - R_J|} \end{aligned} \tag{3.39}$$

Still, the exact solution of equation 3.39 is a formidable work. A simple attempt for solving this many-electron system is the Hartree-Fock (HF) approximation, which was derived based on the variational principle. The HF method translates an N-electron system into one-electron Schrödinger equations. However, such method neglects electron correlations, and in the calculation one has to deal with $3N$-demensions.[112] Moreover, the wave function of one electron in HF equation cannot be accessed directly in experiment. To some extent, this is not very practical. Therefore, using the electron density as a primary variable provides a new insight into solving the Schrödinger equation.

3.4.2 Electron Density (Thomas-Fermi model)

As mentioned before, a practical approach for solving the Schrödinger equation is to use electron density as a variable. Since the electron density is a function of only three variables and has direct experimental relevance (e.g., can be detected by X-ray diffraction). The electron density ρ for N-electrons is defined as the integral of the square

of the wave function (here the spin is not considered) with all electron coordinates except for the coordinate of electron 1:

$$\rho(\vec{r}_1) = N\int ...\int \left|\psi(\vec{x}_1, \vec{x}_2, ...\vec{x}_n)\right|^2 d\vec{x}_2 ...d\vec{x}_n \tag{3.40}$$

$$\rho(\vec{r} \to \infty) = 0, \qquad \int \rho(\vec{r}) d\vec{r} = N \tag{3.41}$$

Note that ρ is a non-negative function and it vanishes to zero at infinity. The integral of ρ over the whole space gives the total number of electrons N. The first density functional theory is described by the Thomas-Fermi model,[113] which is proposed by Thomas and Fermi in 1927. Based on the uniform electron gas, they proposed the following functional for kinetic energy of the system

$$T_{TF}[\rho(\vec{r})] = \frac{3}{10}(3\pi^2)^{2/3}\int \rho^{5/3}(\vec{r}) d\vec{r} \tag{3.42}$$

The energy of an atom is finally obtained using classical expression for the electron-nuclear and electron-electron potentials, thus the Thomas-Fermi energy functional is given by:

$$E_{TF}[\rho(\vec{r})] = \frac{3}{10}(3\pi^2)^{2/3}\int \rho^{5/3}(\vec{r}) d\vec{r} - Z\int \frac{\rho(\vec{r})}{r} d\vec{r} + \frac{1}{2}\int\int \frac{\rho(r_1)\rho(r_2)}{|r_1 - r_2|} d\vec{r}_1 d\vec{r}_2 \tag{3.43}$$

For determining a correct density ρ, variational principles is applied. Under the constraint of equation 3.43, the minimization of energy in the ground state can be achieved.

3.4.3 Hohenberg-Kohn Theorems

The Hohenberg-Kohn theorems relate to all systems of many particles moving under the external potential $V_{ext}(\vec{r})$. They are given in two fundamental theorems.[114]

The first theorem demonstrates that the density of electrons $\rho(\vec{r})$ determines the Hamiltonian operator; it is expressed as follows:

The $V_{ext}(\vec{r})$ (within a constant) is a functional of $\rho(\vec{r})$; since, in turn $V_{ext}(\vec{r})$ fixes $\hat{H}$ we see that the full many particle ground state is a unique functional of $\rho(\vec{r})$.

Therefore, we can write the total energy in forms of ρ as:

$$E[\rho] = \overbrace{T[\rho] + V_{ee}[\rho]}^{F[\rho]} + V_{ext}[\rho] \tag{3.44}$$

Where *F[ρ]* is called the universal functional, which contains the contributions of the kinetic energy and electron-electron interactions.

The second theorem states that:

The ground state energy can be obtained based on the variational principle; the density that minimizes the total energy is the exact ground state density.

The fact is that for any trial density $\tilde{\rho}(\vec{r})$ with given boundary conditions, e.g., $\tilde{\rho}(\vec{r}) \geq 0$, $\int \tilde{\rho}(\vec{r})d\vec{r} = N$, the energy obtained from functional 3.44 is greater than or equal to the true ground state energy E_0:

$$E[\tilde{\rho}] = T[\tilde{\rho}] + V_{ee}[\tilde{\rho}] + V_{ext}[\tilde{\rho}] \geq E_0 \tag{3.45}$$

However, in practice, one needs to approximate $T[\rho]$ and $V_{ee}[\rho]$, which usually yields very large errors. Furthermore, the Hohenberg-Kohn theorems do not provide a way to computing the ground state density of a system in practice. The solution to fix this issue was proposed by Kohn and Sham about carrying out DFT calculations one year later. This method will be discussed in the next subsection.

3.4.4 The Kohn-Sham Equations

The Kohn-Sham ansatz considers a fictitious system including *N* non-interacting electrons,[115] the density of electrons is described as:

$$\rho_s(\vec{r}) = \sum\sum\left|\phi_i(\vec{r},s)\right|^2 = \rho(\vec{r}) \tag{3.46}$$

The kinetic energy of a single electron in the non-interacting system is given by:

$$T_s = -\frac{1}{2}\sum\left\langle \phi_i \left| \nabla^2 \right| \phi_i \right\rangle \tag{3.47}$$

Note that T_s is not equal to the true kinetic energy of the interacting system ($Ts<T$), thus the energy functional of Hohenberg and Kohn is given by:

$$E[\rho] = T_s[\rho] + \overbrace{V_{ee}[\rho] + V_{ext}[\rho] + V_{XC}[\rho]}^{V_s} \tag{3.48}$$

V_{ee} is the Hartree potential; the interaction of electrons is described by V_{XC}, which is the so-called exchange-correlation functional; it contains the unknown part.

$$V_{XC}[\rho] = (T[\rho] - T_s[\rho]) + (U[\rho] - V_{ee}[\rho]) \tag{3.49}$$

Combining equation 3.48 and 3.49, the Kohn-Sham equation of a single electron is given by:

$$(-\frac{1}{2}\nabla^2 + V_s(\vec{r}_i))\phi_i(\vec{r}) = \epsilon_i\phi_i(\vec{r}) \tag{3.50}$$

$$V_s(\vec{r_1}) = \int \frac{\rho(\vec{r_2})}{r_{12}} d\vec{r_2} - \sum \frac{Z_A}{r_{1A}} + V_{XC}(\vec{r_1}) \tag{3.51}$$

To solve equation 3.50, one needs to know the Kohn-Sham operator. Since the effective potential V_s is determined by the electron density $\rho(r)$, and $\rho(r)$ in turn depends on the wave function $\phi_i(r)$. Therefore, the equation can be solved self-consistently, as mentioned in the literature.[112]

3.4.5 Exchange and Correlation Functionals

To describe the exchange and correlation (V_{XC}) of electrons, two different approximations are generally developed for this purpose. First, the local density approximation (LDA) is the simplest way to approximate the exchange-correlation energy functional. In LDA, the central model is based on a homogeneous electron gas, it is considered that the density of electrons is uniformly distributed. So the exchange-correlation energy (E_{XC}) is written in the following form:

$$E_{XC}^{LDA}[\rho] = \int \rho(\vec{r})\epsilon_{XC}(\rho(\vec{r}))d\vec{r} \tag{3.52}$$

Here, $\epsilon_{XC}(\rho(\vec{r}))$ is the exchange-correlation energy per particle of an uniform electron gas of density $\rho(\vec{r})$. It can be further decomposed into exchange and correlation parts: $\epsilon_{XC} = \epsilon_X + \epsilon_C$. The accuracy of LDA for the exchange energy is typically within 10%, while the correlation energy is generally overestimated by up to a factor of two. The two errors typically cancel with each other partially.

However, in a real system, the density of electrons is not uniform. Thus one has to consider not only the electron density at a particular point, but also the information about the gradient of the charge density. We write the exchange-correlation energy termed as generalized gradient approximation (GGA):

$$E_{XC}^{GGA}[\rho] = \int \epsilon_{xc}^{GGA}(\rho, \nabla\rho)d\vec{r} \tag{3.53}$$

GGA has reduced the LDA errors of atomization energies of standard set of small molecules by a factor 3-5. This improved accuracy has made DFT a significant component of quantum chemistry. There are several different types of GGA functionals, in this thesis the PBE proposed by Perdew, Burke and Ernzerhof is mostly used.[116]

4. Methodology and Experimental Setups

In this section, relevant photoswitches as well as organic and inorganic materials used in the present work will be introduced in details. Later, the relevant setups, e.g., UPS, XPS, XAS, UV-vis and AFM, as well as theoretical DFT methods will also be presented, and the relevant data evaluation is also discussed.

4.1 Materials and Sample Preparation

4.1.1 Relevant Photoswitches

The main work of this thesis is to characterize the electronic properties of photoswitches and to dynamically tune the energy level alignment at photochromic heterojunctions via external stimuli. Therefore, several photoswitches have been synthesized (from Prof. Stefan Hecht group) for particular uses (e.g., the fabrication of SAM, switching both optically and thermally). The switches used in this work are all listed in Figure 4.1 and their relevant characterizations and functions will be presented and discussed in chapter 5. First, as described previously in chapter 2.1, DAE molecules exhibit excellent switching properties due to their high fatigue resistance and good thermal stability of both isomers. Moreover, upon photoswitching, they change both molecular conjugations and electronic properties. Therefore, DAE molecules are good candidates for the starting point of the present work. As shown in Figure 4.1a, one derivative of DAE, 1,2-bis(2-methyl-5-p-tolylthiophen-3-yl)cyclopent-1-ene (DAE1),[20,117] was synthesized in order to characterize the electronic properties in thin films. DAE1 molecules undergo ring opening and closure reactions upon light illumination with different wavelength, i.e., UV and green light. The photoswitching gives rise to dramatically different electronic properties between the open and closed forms, such as ionization energy, electron affinity, energy gap, and dipole moment. This will be discussed further in section 5.1.

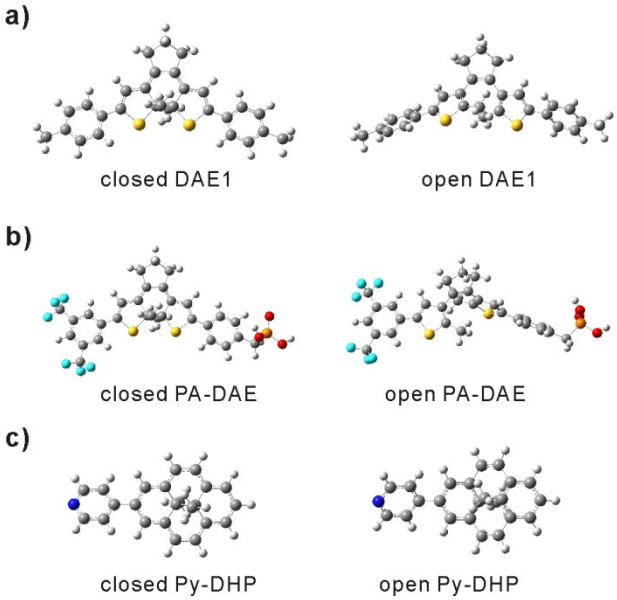

Figure 4.1. Chemical structures of photoswitches used in this work. The molecules for a) DAE1, b) PA-DAE, c) Py-DHP are shown with both of their open and closed forms. The DAE1 molecule exhibits symmetric structures; the PA-DAE is bonded with a phosphonic acid (PA) anchor on one side (As one can see the red O atoms of PA) and with six fluorine atoms on the other side to increase the fatigue resistance. The Py-DHP is connected with a pyridine group, which is expected to bond to ZnO surfaces.

Second, to chemically modify inorganic semiconductor surfaces, DAE molecules were synthesized with a phosphonic acid anchoring group connected on one side of the molecule, that is phosphonic acid DAE (PA-DAE) shown in Figure 4.1b. With such an anchor, PA-DAE is able to chemisorb on the metal oxide surface, thus forming SAMs. Moreover, the molecule comprises a dithienylcyclopentene for the DAE part, which is substituted with a benzylphosphonic acid as an anchoring group on one side and a bis(trifluoromethyl)phenyl group on the other side, presumably providing better fatigue resistance during multiple switching cycles.[118,119] The photoswitching properties of PA-DAE are similar to that of DAE1, i.e., upon UV and visible light illumination, PA-DAE undergoes ring opening/closure reactions. Detailed studies on the switching and electronic properties of this molecule and its dynamic modification of metal oxide (ZnO, ITO) will be present and discussed in section 5.2 and section 5.3. Third, to investigate the switching-induced electronic changes using other stimuli such as thermal energy, a different type of a negative T-type switch, that is Py-DHP (see Figure 4.1c), was

synthesized and employed to switch the hybrid ZnO/Py-DHP interface. As discussed earlier, DHPs are T-type photoswitches, whose ring opening reaction is triggered with visible light; while the ring closure reaction is achieved either with heat treatment or with UV illumination. The introduction of a pyridine group to this molecule enables us to modify the ZnO surface in the form of SAMs due to interactions between the pyridine anchor and the surface metal atoms, thus to study the impacts of molecular dipoles on the surface electronic properties as well as the switching induced electronic level changes. Detailed experimental and theoretical studies will be shown in section 5.4.

4.1.2 Substrates

In this work, both the organic/photoswitch and hybrid inorganic/photoswitch interfaces were systematically characterized for studying the light-induced energy level alignment tuning. For fabricating organic/photoswitch interfaces, two different organic components were used as substrates. One organic polymer is poly(3-hexylthiophene) (P3HT) (purchased from Aldrich),[120] which is a p-type semiconductor and is typically used as hole transport materials (shown in Figure 4.2a). Another polymer is an n-type organic semiconductor, i.e., poly{[N,N'-bis(2-octyldodecyl)naphthalene-1,4,5,8-bis(dicarboximide)-2,6-diyl]-alt-5,5'-(2,2'-bithiophene)} (N2200),[121] which functions as electron transport materials (shown in Figure 4.2b) in OFETs. By investigating both P3HT/photoswitch and N2200/photoswitch interfaces, one would expect that upon light illumination, the energy level change in photoswitches will influence the hole injection in P3HT and electron injection in N2200. Additionally, both of the two polymers are solution-processed, thus they are easy to be deposited in the form of films. This provides a non-cumbersome way for fabricating homogeneous organic films compared to vacuum evaporation.

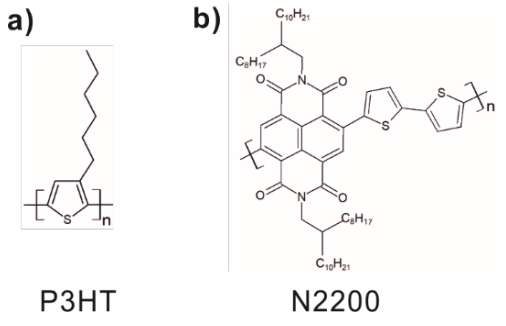

Figure 4.2. Chemical structures of organic semiconductors used in this work. a) p-type organic polymers P3HT, b) n-type organic polymers N2200.

Inorganic semiconductors

For studying the hybrid inorganic/photoswitch interface and for chemisorbing the photoswitches with a PA (that is PA-DAE photoswitch) anchor on the inorganic surface, two metal-oxides were chosen as substrates.

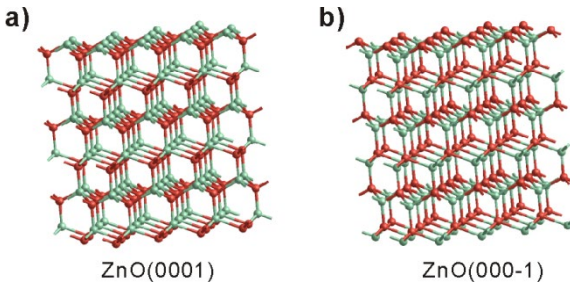

Figure 4.3. Inorganic semiconductor ZnO used in this work for a) Zn-terminated ZnO(0001), b) O-terminated ZnO(000-1).

The first one is ZnO crystal (purchased from CrysTec), which is a superior wide-gap semiconductor due to its high electron mobility, high structural quality and easy processibility, most importantly, can serve as transparent electrode when highly doped. ZnO with polar faces [i.e., Zn-terminated ZnO(0001) and O-terminated ZnO(000-1)], are mostly used in the experiment (see Figure 4.3). For as received ZnO crystals, they are intrinsically n-type doped; the polar surface is passivated by hydroxyl group for ZnO(0001) and hydrogen for ZnO(000-1) for the cancellation of polarity catastrophe.[122,123] Such hydroxyl groups actually play an important role in the formation of PA SAMs, as discussed in section 2.3.2.1. The cleaning of ZnO surface used for SAMs can be separated into two steps. *i)* ZnO was annealed in a furnace (Carbolite, TZF 12/38S) which is filled with clean air (20% O_2 in N_2, H_2O<3 ppm) atmosphere at 1000 ^{0}C for 2h in order to remove surface carbon contaminations and to obtain well-defined crystal terraces with ultra-smooth surfaces (see chapter 5.2 for ZnO AFM image); *ii)* after annealing, ZnO was sputtered with Ar-ions in the vacuum to remove surface phosphorous contaminations. This step is necessary since annealing in the first step cannot remove phosphorous atoms (as shown in Figure 4.4). However, after sputtering, the hydroxyl groups can still be reformed on both surfaces, as reported in literatures.[19,124] The abovementioned cleaning procedure thus ensures us to keep the completeness

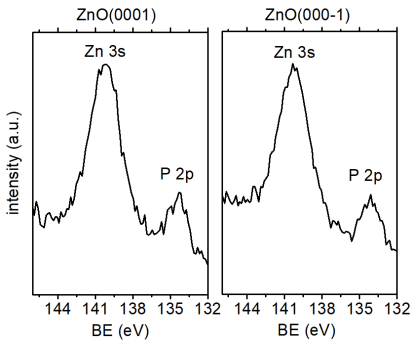

Figure 4.4. XPS of ZnO crystals after being annealed in a furnace at 1000 ^{0}C. One can see that there are still phosphorous residuals on both faces.

of the ZnO surface without any contaminations. Regarding the ZnO cleaning for vacuum deposition of photoswitches, i.e., Py-DHP, ZnO was directly sputtered and annealed at ca. 400 ^{0}C for multiple times. The surface cleanliness was confirmed by measuring C 1s signals with XPS.

Another metal oxide, indium-tin-oxide (ITO), is also used as inorganic counterparts for PA-DAE SAMs, since it is more commonly employed as a transparent electrode in (opto-) electronic devices compared to ZnO.[125,126] The investigation of the ITO/PA-DAE interface provide us a theoretical basis for fabricating ITO-based photoswitchable devices. And this system will be further applied to relevant devices. It is well known that ITO is a highly degenerate n-type semiconductor, which is composed of indium, tin and oxide elements in varying proportions. The ITO coated glass samples used in this work were purchased from the Thin Film Devices Inc. The ITO nominal thickness is 145 ± 10 nm and its sheet resistance is 20 ± 5 Ω, as determined by Four Point Probe measurements. For the purpose of SAM modification, the ITO surface is required to be smooth so that the surface potential modification can be effectively achieved by the sum of PA-DAE intramolecular dipoles. The topography of ITO will be shown latter in chapter 5.3, which exhibits ultra-smooth properties. The cleaning of the ITO surface is simpler compared to that ZnO. ITO was sonicated in isopropanol, acetone and deionized water sequentially for ca. 20 min. After this it is ready for the SAM deposition.

4.1.3 Sample Fabrication

For the preparation of DAE1 thin films, DAE1 solution was deposited by spin-coating methods. DAE1 molecules were first dissolved into the chloroform solvent with an original concentration of 5 mg ml^{-1}, the DAE1 solution was spin-coated on substrates on which thin films of organic materials P3HT or N2200 were pre-covered. The thickness of DAE1 films was varied by adjusting either the spin speed or solution concentration. Consequently, 2 nm and 10 nm DAE1 layers were obtained by spin coating 5 mg ml^{-1} and 1 mg ml^{-1} solution at the speed of 25 revolutions per second (rps) and 13 rps, respectively.[28] All subsequent sample preparation steps were performed in the N_2 atmosphere in a glove box.

The chemisorption of PA-DAE SAMs was carried out by following previous procedures,[124,127] which proved to be efficient for the fabrication of SAMs with phosphonic acid on metal oxides. According to the recipe, the ZnO crystal or ITO-coated glass was immersed into a 1 mM solution of the PA-DAE switch (originally in the open form) in tetrahydrofuran (THF) solvent for two hours, and subsequently annealed in air at 90℃ on a hot plate for 40 min and then sonicated in THF for 30 min. The preparation procedure was repeated for twice more in order to achieve a densely packed monolayer of PA-DAE. During the whole preparation process, samples were either kept in dark or exposed to low-intensity visible light to avoid unintended switching.

For *in situ* photoswitching of DAE, the samples were irradiated through a viewport on the UHV chamber with visible and ultraviolet (UV) light, respectively. Visible light (λ > 450 nm) was obtained either by putting a 450 nm cut-off filter in front of a white light lamp (SoLux, 4700 K, 35 W, 36°, EIKO) or by using a green light LED (λ centered at 565 nm); the measured photon intensity (I_0) was at ca. 200 mW cm^{-2} for both light source. UV light (λ centered at 365 nm) was provided by a high power UV-LED (Thorlabs, M365L) mounted with an adjustable collimator; the measured I_0 was ca. 100 mW cm^{-2}.

Regarding the preparation of Py-DHP switches, the evaporation of Py-DHP (originally in closed form) onto the clean ZnO surface was from a resistively heated quartz crucible. The evaporation rate was controlled at 1-2 Å min^{-1} by a quartz crystal microbalance. During the sample preparation and transfer, the samples were kept in dark (or exposed to low-intensity of visible light to avoid unintended switching) and without breaking the vacuum. For switching, the sample was *in situ* either illuminated with green light to switch the molecule from its closed to open form, or heated to the temperature of 50 ºC to switch back to its closed form. All measurements were performed at room temperature.

4.2 Experimental Setups

A large range of characterization techniques was used in this work, including PES, NEXAFS, AFM and UV-vis absorption. Further theoretical calculations were performed at the DFT level to support these experimental observations. Since the PES measurements

have been mostly performed in this work, thus the UHV setups both at the lab of HU berlin and in synchrotron center (Bear endstation at Elettra and SurIcat endstation at Bessy) will be the mainly focus.

4.2.1 Setups at the HU Berlin Lab

Most of this work was carried out at a custom-made multi-chamber UHV system at the HU Berlin lab. The system is equipped with UPS, XPS, and IPES and it consists of a fast load lock (base pressure < 1×10^{-7} mbar), a sample preparation chamber (< 5×10^{-9} mbar), and an analysis chamber (< 2×10^{-10} mbar). For measuring UPS on the photoswitches, photoelectrons were excited with Al-foil attenuated He I ($h\nu$ = 21.22 eV) radiation at very low excitation density (approx. 20 times attenuated compared to the standard sources), since organic semiconductors are sensitive to intense irradiation.[128,129] Under these conditions, radiation damage and charging of the samples were negligible (see Figure 4.5 for UPS on DAE1). Photoelectrons were collected and measured with a hemispherical spectrometer (SPECS Phoibos 100); the total instrumental energy resolution was 150 meV measured with a pass energy of 5 eV, as determined by measuring the Fermi edge (see further details in chapter 4.4.1). The secondary electron cutoff (SECO) spectra were recorded with a bias of –10 V to observe the clear cutoff region. For XPS measurements, Al K_α source (1486.6 eV) or Mg K_α (1253.6 eV) source were employed to study the core levels. The binding energy scale was calibrated by scanning the Au $4f_{7/2}$ peak position (XPS) and Fermi level edge of an Au film (UPS), which was cleaned by repetitive Ar^+ ion sputtering. The Fermi level is referred to the zero binding energy in all the UPS and XPS spectra in the setup. IPES was performed in the same system with a custom setup (incident electron energy range: 5-15 eV, NaCl coated photocathode, SrF-window).

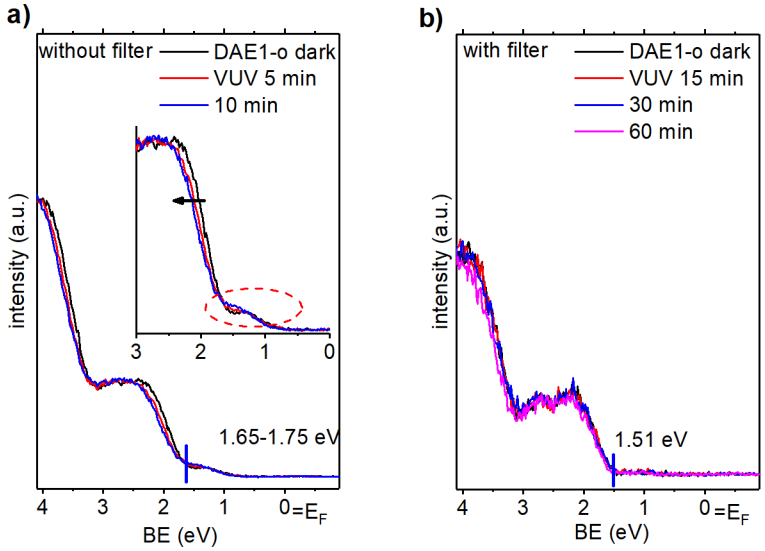

Figure 4.5. He I UPS spectra of a DAE1-o film (10 nm) on an ITO glass substrate before (DAE1-dark) and after prolonged He I light irradiation. a) He I light with a strong photon flux from a standard commercial light source; obvious radiation damages (shift, switching, charging) can be seen even in a short-time irradiation (5 min), which is almost the same as a typical acquisition time of UPS spectra. b) Photon flux of He I was attenuated to ca.20 times using an Al thin film filter (ca. 500 nm), with which no obvious spectra shift or switching were observed within one hour irradiation.

Except for UHV system, AFM and UV-vis measurements were also performed at HU Berlin. AFM was measured in tapping mode with a Bruker Dimension FastScan system. While UV-vis absorption was measured with a PerkinElmer Lambda 950 spectrometer.

4.2.2 Beam Station BEAR

Part of experiments was performed with synchrotron radiation at the Bending Magnet for Emission, Absorption and Reflectivity (BEAR) beam station in Elettra Trieste. For the BEAR station, it is located at a bending magnet that provides low dose photon flux (typical photocurrent at hundreds of pA). Moreover, the intensity of photon flux can be further attenuated by a series of removable filters (e.g., Ag, Sn). This allows measuring organic samples without notable damages. The photon energy was tuned by monochromators equipped with two different plane gratings (G1200 and G1800) in different energy regimes. With this function, we are able to tune the kinetic energy of out-coming electrons at minimum of ca. 100 eV, which is highly surface sensitive for the measured samples. Regarding the ZnO/PA-DAE SAM, the core level peaks of Zn 3s, P 2p, C 1s, and O 1s were thus measured with nominal photon energies of 265, 390, and

640 eV, respectively. The determination of the real photon energy is by measuring the kinetic energy of Au 4f core level spectrum with the 1st and 2nd order of photons, then the real photon energy is: $h\nu = E_{Au}^{2} - E_{Au}^{1}$.

To obtain information of molecular orientations, angle-dependent X-ray absorption spectroscopy experiments were measured in the TEY mode. The incident light was elliptically polarized with the dominating components in the horizontal plane. The corresponding ellipticity defined as $\epsilon = \left|\vec{E}_V\right|^2 / \left|\vec{E}_H\right|^2$ was 0.1. The incidence angle of the light with respect to the sample surface plane was fixed to 10º. The sample was then rotated around the beam axis to change the relative polarization of the light.

4.2.3 Beam Station SurICat

For the PES data about ITO/PA-DAE SAMs, they were collected at BESSY II, Berlin at the endstation for Surface investigation and Catalysis (SurICat). The beamline SurICat is equipped with a plane grating monochromator operated with collimated light in a range of 20 eV to 2000 eV. To lower the intensity photon flux, an Al filter was used for organic sample measurements. For the PES measurements, photoelectrons were collected with a Scienta SES 100 electron spectrometer. The angle between the incident beam and the spectrometer was fixed at 60º, while the sample can be rotated in two axes: *i)* the surface normal of a sample can be changed in the plane of photon beam and spectrometer; *ii)* sample azimuthal angle with respect to the surface normal can be rotated. This enables performing angle-dependent measurements, i.e., angle-dependent PES, angle-dependent XAS. The measurement of XAS was recorded with the TEY mode. The electrical signal was detected using a Keithley 6514 electrometer via a double shielded BNC cable.

4.3 Theoretical Methods

Theoretical calculations were performed at the DFT level. The optimized geometry and ground-state electronic properties (frontier orbitals and dipole moment) of the isolated molecules (e.g., DAE, DHP) were obtained using the Perdew-Burke-Ernzerhof (PBE) functional, both with pure (PBE)[116] and hybrid (PBE0)[130] functionals, and a 6-31G(d) basis set.[131] Time-dependent density functional Theory (TD-DFT) calculations were

performed to simulate the absorption spectra and assess the nature of the relevant electronic excited states using the same basis set and also the PBE and PBE0 functional. All calculations in the gas phase were performed with the Gaussian 09 software.[132] On the other hand, the electronic properties of photoswitch monolayer on ZnO or ITO were described using the SIESTA 4.0 (Spanish Initiative for Electronic Simulations with Thousands of Atoms) computational code,[76] with periodic boundary conditions (PBC) in order to generate an infinite two-dimensional slab.[76] The valence electrons are described here by using the LCAO approximation and a Double Zeta Polarized basis set; the valence-core interactions are described by Troulier-Martins pseudopotentials.[133] DFT calculations on interfaces were performed within the generalized gradient approximation (GGA) by using the PBE exchange correlation functional. The mesh cut off used is 190 Rydberg. For the calculation of ZnO, the surface and bottom part of the ZnO slab were covered with -OH group and H atoms with 50% of coverage to prevent the "metallization effect"[134] and reflect the actual experimental conditions. For all calculations, a (2×3×1) Monkhorst-Pack k-point grid[135] was used for describing the electronic structure in the first Brillouin zone. In order to fasten the geometry optimization, the bottom six layers were frozen and only the top six layers can be relaxed. While for the calculation of ITO slab, the plane wave cut off was 300 eV, a value of 10^{-6} eV was set for the total energy convergence; and a k-sampling of (2×2×1) and the tetrahedron integration method were used in the Brillouin Zone. The geometry optimizations were carried out following a damped molecular dynamics method with a force cut-off for the convergence equal to 0.04 eV $Å^{-1}$. In order to decrease the computational time, the coordinates of the last two (In-O)/(Sn-O) layers were frozen during the optimizations.

4.4 Data Processing

Data processing is of high importance for analyzing the experimental results, in the following, it will be introduced in details the methods used to process the raw data acquired from different kinds of experiments.

4.4.1 Photoemission Results

The photoelectron spectra measured with non-monochromatic light sources (e.g., He I, for the valence region, Al or Mg Kα for the core level region) have to be calibrated by subtracting the signal of corresponding satellites (see appendices A for X-ray and UV satellites). While for the SECO, one has to subtract the bias (in this work bias was -10 V) to obtain the sample work function. In order to evaluate the measured core level and valence spectra in details, spectral fitting as well as deconvolution was mostly used. The calibration of the binding energy and the determination of spectrometer energy resolution were derived by fitting the Fermi edge of a clean Au with a Fermi-Dirac (FD) function at room temperature (k_BT=0.026 eV) broadened by a Gaussian function:[136]

$$F(E) = \int_{-\infty}^{\infty} G(u)f(E-u)du \qquad (4.1)$$

Note that in equation 4.1, the energy broadening is primarily due to the analyzer, and the spectrum is virtually a convolution of the FD function with a Gaussian function. Figure 4.6 schematically describes the fitting of an Au Fermi edge, from which, the zero binding energy is determined at the center of the Gaussian peak. The analyzer resolution is derived from the full width at half maximum (FWHM) of the Gaussian broadening. For example, the analyzer resolution of UPS for the setup at the HU Berlin lab is 150 meV when measuring with a pass energy of ~5 eV.

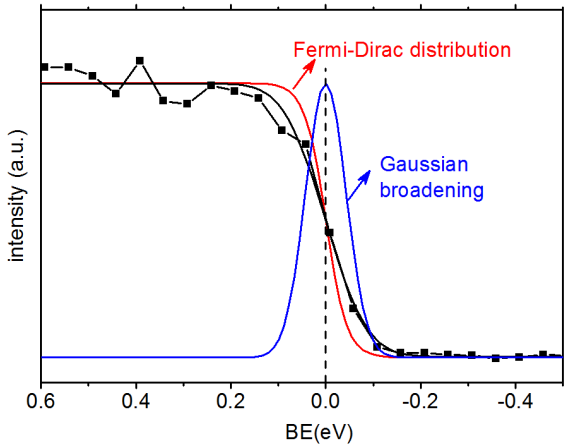

Figure 4.6. Deconvolution of the Fermi edge of Au measured from UPS. The experimental spectrum (dotted line) is convoluted by a Fermi-Dirac function with a Gaussian broadening. Thus zero binding energy is calibrated at the center of the Gaussian profile and the energy resolution of the analyzer is derived from the FWHM of the Gaussian broadening (150 meV for the home-made setup measured with a pass energy of 5 eV at HU Berlin).

The fitting of core level spectra enables a detailed analysis on the chemical composition of the sample, the background caused by the inelastic

collisions of primary electrons was described primarily with either a Shirley or a Tougaard function.[137,138] The Shirley regime (see detailed math in appendices B) considers the energy loss cross section as a constant, thus it is reasonable for the case of relatively narrow energy range since the cross section of inelastically scattered electrons is approximately the same. As shown in Figure 4.6a, a typical Au 4f peak can be well fitted with a Shirley background. While for a wide range of spectra (e.g., the XPS survey), the Touggard regime makes the most sense due to its consideration of energy loss cross section of inelastic electrons (Figure 4.6 b). The formula of Tougaard background is given by:

$$T(E) = \lambda(E) \int_E^{\infty} K(E, E' - E) I(E) dE' \tag{4.2}$$

$$\lambda(E) K(E, E' - E) = \frac{B(E' - E)}{(C + (E' - E)^2)^2} \tag{4.3}$$

For equation 4.3, it is the so-called universal cross section, and in this equation B and C are 2866 and 1643 eV^2,[139] respectively. It is noted that when the cross section (equation 4.3) approximates to a constant, equation 4.2 becomes the expression of Shirley background (as discussed above).

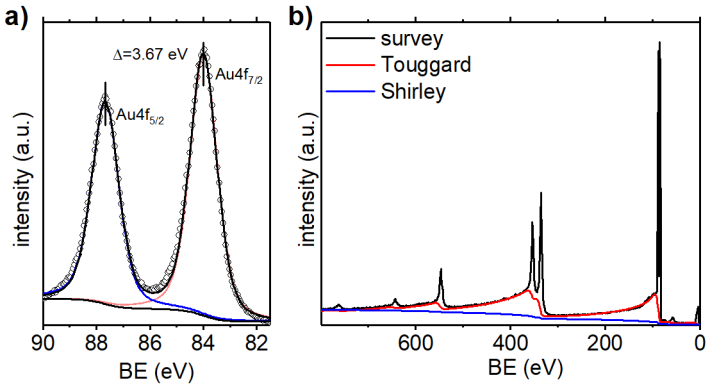

Figure 4.7. a) Narrow scan of Au 4f core level electrons with a Shirley background applied to the peak. b) XPS Survey of Au surface with both Shirley and Tougaard backgrounds applied to the spectrum, from which one can differentiate that the Tougaard regime describes better the background.

Principally, the measured PES peak is in fact a convolution of a Gaussian profile with a Lorentzian profile. The Gaussian profile in the peak describes the broadening resulting from the setup and temperature, e.g., instrumental broadening, Doppler and thermal

broadening. While the Lorentzian profile corresponds to UV/X-ray line-shapes as well as a natural broadening due to the uncertainty principle relating lifetime and energy of the out-coming electrons. Therefore, it is physically meaningful to fit the PES spectrum with a Voigt profile, which is expressed in the form of a convolution:

$$V(E) = \int_{-\infty}^{\infty} G(u)L(E-u)du \tag{4.4}$$

However, the convolution process of a Voigt function (equation 4.4) is far more complicated; this leads to very time-consuming fitting process for a computer, which is not practical. Mostly, it is common to use a summation of *G(E)* and *L(E)* profiles as a substitute to fasten the fitting:

$$SGL(E) = (1-m)G(E) + mL(E) \tag{4.5}$$

Equation 4.5 is the so-called Pseudo-Voigt approximation. The factor m is dependent on the FWHM of *G(E)* and *L(E)* profiles and its value is $0 \leq m \leq 1$.

Besides spectral fitting, another method used in the XPS data analysis is the spectra deconvolution,[136,140,141] which deals with unintended peak broadening caused by the setup. As described in equation 4.4, the measured PES spectrum is a convolution of an intrinsic spectrum (Lorentzian profile) with a setup broadening (Gaussian profile). To perform a deconvolution, one needs to know first the setup broadening function, which is the so-called response function. Then the task becomes to solve equation 4.4, where $V(E)$ is the measured spectrum. Principally, after the deconvolution, the final spectrum is only represented with a Lorentzian profile, whose FWHM is from the natural broadening and is thus narrow enough to identify different chemical components more pronouncedly. However, the deconvolution process is very complicated and is considered as an ill-posed problem mathematically in literatures. [136,140,142] A practical way was to apply an iterative "point simultaneous over-relaxed Jansson algorithm".[136] A detailed numeric description about the deconvolution can be found in Appendices B.

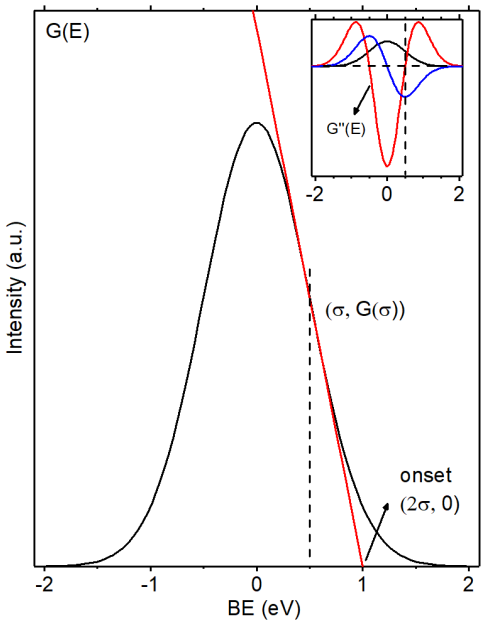

Figure 4.8. A HOMO peak described with a Gaussian approximation. The onset is determined with the line extrapolation method (details see the main text). The inset shows the first (blue line) and second (red line) derivative of a Gaussian function. For extrapolating the onset, one needs to know first the inflection point, which is derived from the zero point of the second derivative. Then one need to know the slope of the line that goes through this point; this is calculated from the first derivative. Once the equation of the line is determined, the crossing point with y=0 is easy to know.

After peak processing, it is of importance to analyze the position of the peak to get information about energy difference. For example, the HOMO onset of organic layers with respect to the Fermi level is of high interest in this work. By simply assuming that the broadening of HOMO is a Gaussian profile, thus the onset is defined by the crossing point between the tangent (this is determined by the first derivative of the Gaussian function) at the inflection point (derived by calculating the second derivative) and the baseline. Consequently, the onset of HOMO can be precisely determined to be 2σ (σ is the standard deviation of a Gaussian function). Details are plotted in Figure 4.8, where the inset shows the plotting of first and second derivatives.

4.4.2 X-ray Absorption Data

The processing of XAS spectra was based on the usual procedure described by Watts et al.[143] The initial signal was composed of offsets, both in energy and intensity coordinates. Therefore, the first step was to remove these offsets from as-measured results. To do so, the mirror current signals were recorded to calibrate the energy scale. After removing the energy offset, the spectra were normalized by dividing the spectra of a clean reference sample. For example, for the measurements of C 1s absorption, the reference sample should be free of carbon contaminations. By doing this, the effect due to vibrations in photon flux and contaminations is eliminated.

4.4.3 Atomic Force Microscopy Data

All the AFM images have been processed using the Gwyddion software. The data were leveled by either a mean plane subtraction or a linear background subtraction, then the horizontal scars of images were also corrected after the background subtraction. For the surface with terraces (e.g., ZnO surface), the plane was leveled by manually using three points. The minimum of the data is always fixed to zero. The color range of images was scaled based on the histogram profiles.

5. Results and Discussion

The main objective of this work is to study the electronic properties of photoswitches at their different isomeric states. In particular, the study is focused on dynamically tuning the interfacial energy level alignment upon photoswitching of photochromic layers. In the following section, the impacts of photoswitching on the electronic properties of DAE molecules, i.e., their optical gap, molecular dipole moment, electron affinity, and ionization energy, will be elaborated on. Furthermore, it will be presented that such switching-induced electronic changes can be employed to the hybrid interface to tune interfacial electronic properties in a dynamic manner. Finally, a T-type DHP switches is also proved to be able to reversibly modify the hybrid inorganic ZnO surfaces electronic properties upon both light illumination and heat treatment. These findings provide a pathway for developing photoswitchable devices.

5.1 Diarylethenes at Interfaces with Organic Semiconductors

To investigate the electronic change of photoswitches upon external stimuli, one DAE derivative, that is DAE1, was chosen since it is the most suited photoswitch not only due to its supreme switching properties but also due to its easy processibility (solution-processed). Thus the light-induced electronic changes (e.g., dipole moment, energy gap, IE, EA) of DAE1 thin films are characterized and discussed in details. To evidence the energy level tuning at the metal/organic and organic/organic interfaces due to such electronic changes, DAE1 thin films were sequentially deposited onto the Au and the polymeric P3HT and N2200 surfaces. detailed PES and DFT results will be presented in the following.

5.1.1 Electronic Properties of Diarylethenes

It is necessary to first understand the switching and electronic properties of photoswitches upon external stimuli so that one can get familiarized with their physical properties, and

can implement further implications, i.e., dynamically controlling the (hybrid) organic interface electronic properties. Therefore, DAE1 thin films were characterized both experimentally and theoretically. Figure 5.1a displays the UV-vis absorption spectra of DAE1 thin films (chemical structure see Figure 4.1a) on quartz. It is shown that for the closed form (DAE1-c), the absorption maximum is located at green region (ca. 550 nm or 2.2 eV). While after switching to open form (DAE1-o), the absorbance feature at green region totally disappears (corresponding to a nearly 100% switching efficiency), and the absorption maximum shifts to UV region (ca. 320 nm or 3.7 eV). This points to that the optical gaps of these two forms are dramatically different: the gap of DAE1-o is ca. 1.5 eV larger than that of DAE1-c.

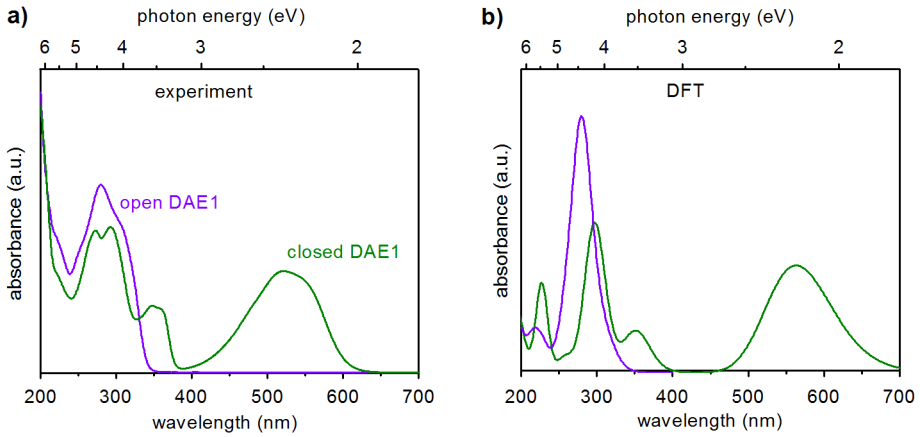

Figure 5.1. a) UV-vis absorption spectra of DAE1 thin films on a quartz glass substrate. The open (purple line) and closed (green line) forms show dramatically different absorption features: the absorption of closed DAE1 is (mainly) at the green region; while the absorption of open DAE1 is at the UV region. b) Time-dependent DFT (TD-DFT) calculations on the open and closed DAE1 single molecules in the gas phase.

TD-DFT calculations were further performed to validate these experimental observations. As shown in Figure 5.1b, the calculated absorption spectra for DAE molecules in the gas phase are in good agreement with the UV-vis absorption results, thus confirming that different absorption properties and different optical gaps exist between the two forms. To further stress the electronic changes upon switching between DAE1-o and DAE1-c isomers, DFT calculations on single molecules in the gas phase were performed to check the frontier orbitals and dipole moments of DAE1 molecules. The results are shown in

Figure 5.2. For the two forms, both of the HOMO and LUMO orbitals are distributed in the backbone of DAE1 molecules. However, the frontier orbitals of open form are less conjugated compared to that of closed form, thus pointing to that the ring-opening/closure reactions are accompanied by a change of molecular conjugations. Calculations on the molecular dipole moments (Figure 5.2c and f) show that the dipole of DAE1-c is ca. 1.2 D larger than that of DAE1-o; this is in line with the reported results.[21] Therefore, the electronic changes in the molecular conjugation and dipole moments of DAE1 switches upon switching are evidenced theoretically.

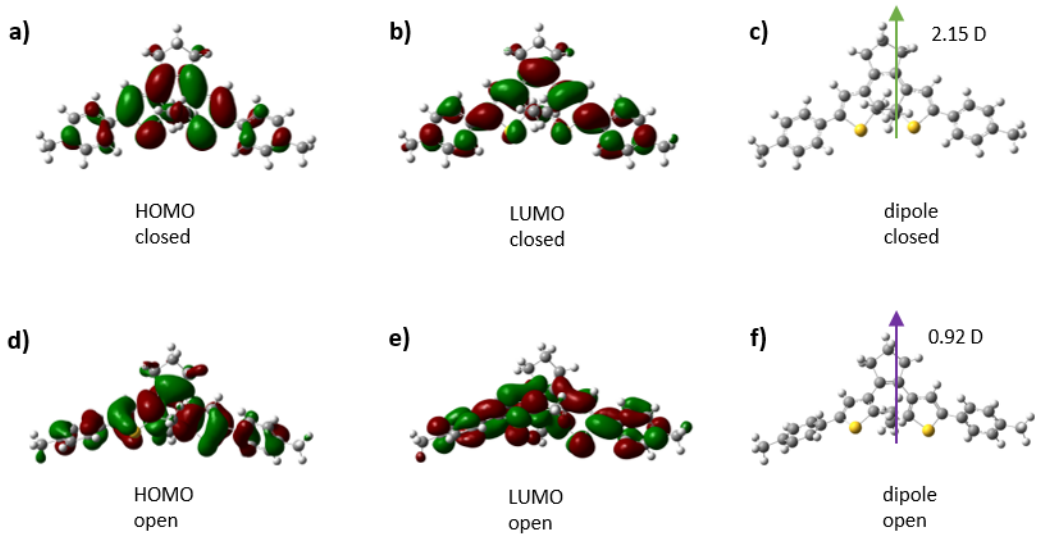

Figure 5.2. Calculated frontier orbitals for a) HOMO of closed DAE1, b) LUMO of closed DAE1, d) HOMO of open DAE1, e) LUMO of open DAE1. The isovalues used for the plotting are ± 0.02 a.u. for each of orbitals. DFT calculated dipole moments are shown in c) for closed and f) for open forms.

The changes in the DOS of DAE1 between its two forms were monitored in details with UPS and IPES. Upon UPS measurements, information about the valence occupied electronic levels and work function changes upon photoswitching were derived. While by performing IPES, the unoccupied electronic levels of DAE1 can be obtained. Figure 5.3 displays both experimental and DFT calculated frontier electronic properties of DAE1 thin films. Originally, DAE1 molecules were in closed states and they were measured in dark (Figure 5.3a). The onset of DAE1-c HOMO level is determined at 0.6 eV BE from UPS; and the DAE1-c work function is at 4.4 eV (see Figure 5.3a). Thus the IE value of

DAE1-c is calculated to be 5.0 eV (HOMO + work function), in line with reported literature values.[21] The film was then illuminated with a green light LED (565 nm) in order to trigger a ring-opening reaction. As a result of green illumination, the HOMO feature of DAE1-c in the valence region gradually attenuates and a new occupied feature at 2.0 eV BE appears at the same time.

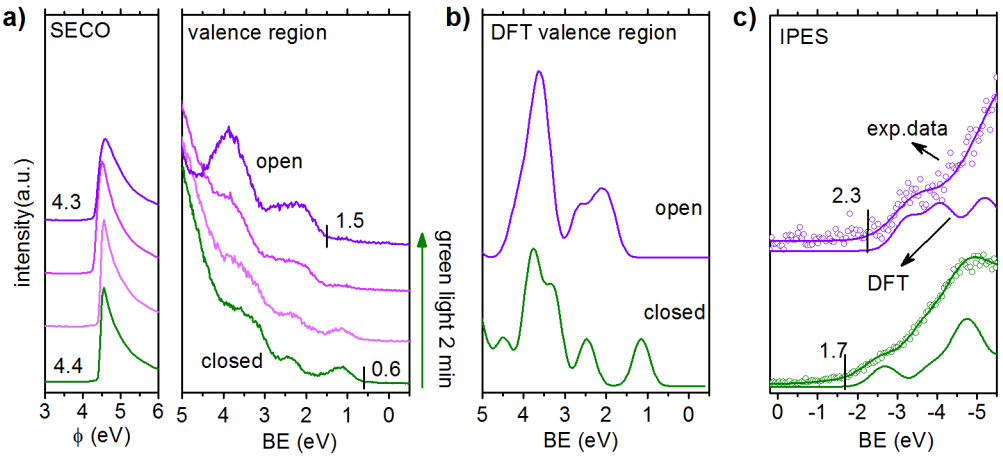

Figure 5.3. a) UPS spectra of DAE1 thin films on ITO (originally in closed forms) upon cumulative illumination of green light. The light-induced work function change and HOMO level shift are displayed in the left (SECO) and right (valence region) panels, respectively. b) DFT calculated DOS in the valence occupied region. The DOS was broadened by 0.4 eV to make a direct comparison with UPS data. In this calculation, photoemission cross sections are not considered. c) IPES spectra of DAE1 thin films for revealing the unoccupied electronic states. The spectra show good agreements with the DFT calculations.

After light illumination for 2 min, the measured spectrum exhibits dramatically different features compared to the original DAE1-c. This is the result of a ring-opening reaction, and thus the molecules are now in the open forms with their HOMO onset at 1.5 eV BE. Notably, only a 0.1 eV work function decrease is observed in the SECO region after photoswitching. Considering that there is a 1.2 D molecular dipole difference between the two forms as calculated from DFT (see Figure 5.2), one would expect an obvious potential change upon photoswitching. However, since the molecules are amorphously distributed in the film, a deep dipole cancellation will play a role in the potential change. Therefore, such a small work function change induced by photoswitching is primarily attributed to the dipole cancellation. From the spectrum after green illumination (in Figure 5.3a), the IE value of DAE1-o is calculated to be 5.8 eV, which is 0.8 eV higher than that

of DAE1-c. Additionally, the DFT calculated DOS is shown in Figure 5.3b, compared to the UPS spectra, the DOS is in good agreement with the experimental results, indicating that photoswitching virtually occurs upon light illumination.

The unoccupied electronic features measured with IPES are shown in Figure 5.3c, and the DFT calculated unoccupied DOS is also plotted in the same figure as a comparison. It is obvious that the IPES spectra are well reproduced by the calculated DOS, confirming different unoccupied electronic properties existing between the open and closed forms. Upon IPES measurements, the onsets of DAE1-o and DAE1-c LUMO levels are precisely determined at 2.3 eV and 1.7 eV BE, respectively. Finally, by summarizing the UPS and IPES results, the energy levels of both DAE1-o and DAE1-c films are extracted in Figure 5.4. As shown in this figure, the transport gaps (HOMO-LUMO gap) of DAE1 films are precisely determined, that is 2.3 eV for DAE1-c and 3.8 eV for DAE1-o, respectively. Compared to previously determined optical gaps from UV-vis measurements, it is found that the DAE1 transport gaps are ca. 0.3-0.5 eV larger than its optical gaps for both forms. As discussed in chapter 2, this is due to the presence exciton binding energies during the photoexcitation process (see discussions in Figure 2.2). Regarding the measured frontier levels of DAE1, the LUMO of DAE1-c is located lower than that of DAE1-o; while the situation is reversed for the HOMO levels. These properties play a very important role in the tuning of energy levels for effective charge injection as well as extraction.

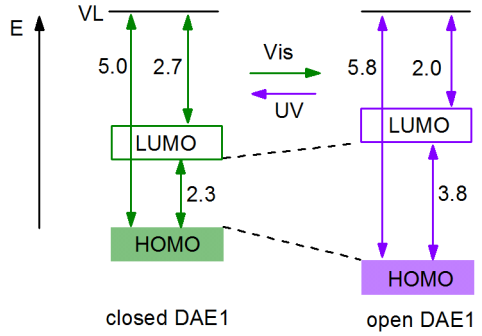

Figure 5.4. Energy level diagram of closed DAE1 and open DAE1 summarized from UPS and IPES measurements in Figure 5.3. The transport gap of closed form is 1.5 eV, which is smaller than that of open forms. Upon switching from closed to open DAE1, the LUMO level shifts upwards. Conversely, the HOMO level shifts downwards.

Conclusion

Combining experimental observations with DFT results, it is shown that switching DAE1 between its open and closed forms induces dramatic electronic changes: *i*) Both the optical gap and transport gap of DAE1-o are ca. 1.5 eV larger than that of DAE1-c; *ii*) DFT calculations show that the dipole moment of DAE1-o is 1.2 D larger than that of DAE1-c; *iii*) valence occupied and unoccupied DOS are dramatically different between the two forms; *iiii*) the IEs (EAs) of DAE1-o and DAE1-c are 5.8 eV (2.0) and 5.0 eV (2.7), respectively. These electronic changes are expected to modify the substrate surface and to tune the interface ELA; this will be the focus of the following section.

5.1.2 Metal/Diarylethene and Organic/Diarylethene Interfaces

After getting familiar with the electronic properties DAE1 films, DAE1 was then deposited onto the metal electrode and organic semiconductors in order to demonstrate the manipulation of interfacial ELA upon external light illumination. The following subsection is adapted from the published paper [28],

Exploring the ELA manipulation by photoswitches is of high importance for understanding the charge injection as well as transport behaviors and for optimizing photoswitchable devices. So far, for DAE1 molecules the ELA at the electrode/DAE1 as well as the organic semiconductor/DAE1 interfaces is still not comprehensively understood. Particularly with respect to metal electrodes, the energy position of DAE frontier levels is yet unknown, and even the ability to photoswitch the molecules in proximity to the metal can questioned due to dipole selection rules. Regarding the level alignment at interfaces, the traditional Schottky-Mott limit[144] often fails to predict the energy level difference, e.g., between the highest occupied and lowest unoccupied molecular orbital with respect to the Fermi level of the system at metal/organic and organic/organic interfaces. Therefore, a detailed analysis of the electronic properties and interface ELA of DAE-based (bulk and planar) heterojunctions is necessary for photoswitchable devices.

Therefore, the frontier electronic structure of interfaces with DAE1 thin films was investigated with UPS. The full electronic structure of DAE1 on a gold electrode was first

revealed, and the photo-induced switching on the surface was demonstrated. Furthermore, the ELA at the interface between DAE1 and a prototypical hole conducting polymer P3HT and an electron conducting polymer N2200 were determined, again including *in situ* switching. It is found that the photoisomerization process has a huge influence on interface energy level offsets, leading to photo-tunable hole (electron) injection as well as extraction.

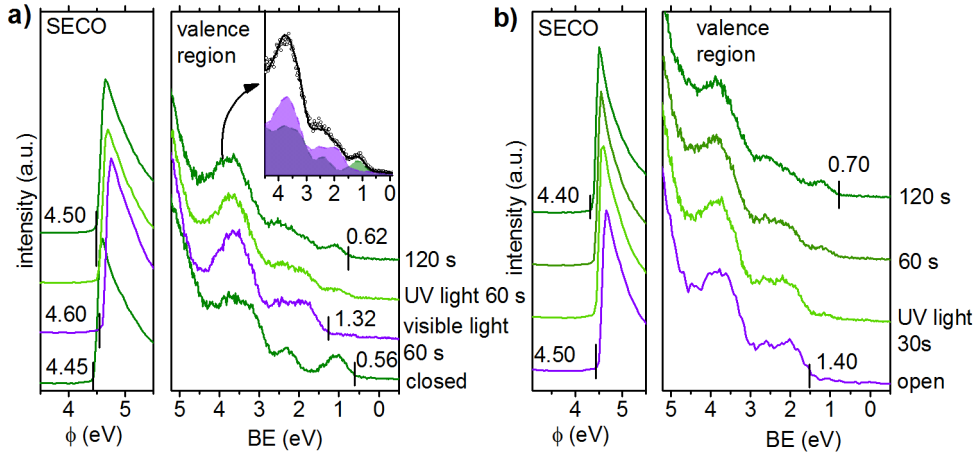

Figure 5.5. Electronic structure of 10 nm thick DAE1 films on Au substrates upon switching with UV and visible light. a) UPS spectra (valence and SECO regions) for initially DAE1-c. Inset: decomposition of the sample spectrum (open circles) after 120 s UV light irradiation with DAE1-c and DAE1-o contributions (sum given by the black line). b) UPS spectra of initially DAE1-o. After cumulative illumination with UV light, DAE1 switches to its closed form, as indicated by the appearance of HOMO centered at ca. 1 eV BE.

To probe the photoisomerization of DAE1 molecules on the gold substrate and their ELA at the Au/DAE1 interface, at first a DAE1-c film with a thickness of approximately 10 nm on a polycrystalline Au substrate was studied by UPS. During the measurements, visible ($\lambda > 450$ nm) and UV lights were employed to achieve photoswitching. As shown in Figure 5.5a, the measured onset of the HOMO level and work function ϕ for the DAE1-c film were 0.56 eV and 4.45 eV, respectively. Then its IE value is calculated to be 5.01 eV, which is the same as the results obtained on ITO in the 5.1.1. The subsequent, light-induced photochromic reaction is accompanied by both changes of the film color (from pink to transparent) and of valence region spectra. The HOMO feature of the DAE1-c film (centered at ~1 eV BE) completely disappeared after 60 s of visible light

illumination, and instead a new occupied feature with the onset at 1.32 eV BE emerged, indicating the formation of DAE1-o isomers on the surface. This new occupied feature is accordingly assigned to the HOMO of DAE1-o molecules. Considering the analyzed volume of the film (UPS surface sensitivity is ~3 nm), one can conclude that a switching efficiency for (at least near surface) DAE1-c molecules of almost 100% could be achieved.

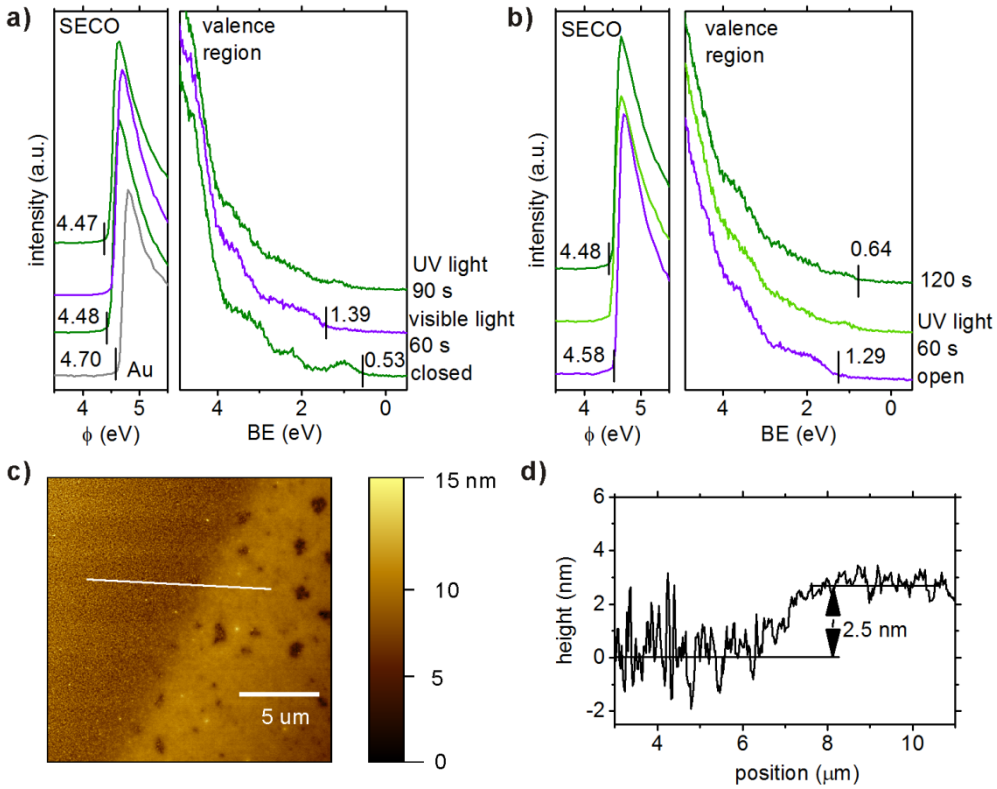

Figure 5.6. a) UPS spectra of a 2 nm thick DAE1-c film on Au, switching process was achieved by the irradiation of visible and UV light, respectively. b) UPS spectra of a 2 nm DAE1-o film, which was irradiated by UV light for switching. c) Topography image of ultra-thin DAE1-c layers on Au surface as measured by AFM. Film thickness was measured by partially wiping away surface molecules using ethanol solvents. d) Line profile extracted from Figure c.

Moreover, the photoisomerization process resulted in a SECO shift by 0.15 eV towards the higher work function. A similar work function change was also observed for DAE1 on ITO substrates,[21] but the shift was in the opposite direction. The ϕ change after photoswitching was attributed to an influence of the substrate ϕ and also the DAE1 molecular dipole moment (as discussed in detail further below). Subsequently, the illumination of the sample with UV light resulted in a ring-closure reaction, as indicated by the re-appearing DAE1-c HOMO feature with its onset close to the original position

at ~0.62 eV BE. Also ϕ was observed to be at its original position (4.5 eV) when the photostationary state was established after 120 s UV light irradiation. However, it is noteworthy that the spectrum in the valance region is still composed of both DAE1-o and DAE1-c contributions, according to the decomposition of measured UPS spectrum. A fraction of 45% DAE1-o and 55% DAE1-c molecules (see fitting results in inset of Figure 5.5a) suggests that the back transfer (from DAE1–o to DAE1-c) was not completely reversible. This can be attributed to a manifold of causes, such as steric hindrance,[145] radiation (UV, VUV) induced photo-quenching,[146] which prohibits such photoswitching of DAE1 molecules during light irradiation. Fully analogous photochromic switching was also observed for an ultrathin DAE1-c layer with only of a 2 nm thickness (Figure 5.6); the thickness was estimated by considering both XPS spectra and AFM images (Figure 5.6c). These results prove that the switching properties of DAE1 molecules retain not only in the bulk, but also in immediate proximity to the metallic Au substrate.

Figure 5.5b shows that *in situ* illumination of a film of initially pure DAE1-o using UV light as well gave rise to the attenuation of HOMO features of DAE1-o and the emergence of low BE-states (at ~0.7 eV). These states are accordingly assigned to the HOMO of DAE1-c molecules. As the ϕ stayed at the same value (within 0.1 eV), thus the IE values of the two isomers vary substantially (as was the case above), between 5.8 eV for the open and 5.0 eV for the closed form. As was the case for the ultrathin DAE1-c above, the switching process for the ultrathin DAE1-o layer (2 nm, indicated in XPS in Figure 5.6b) on Au is operative. Note that the position of HOMO onset, which is located at 1.29 eV BE in the valence region for the ultrathin film, is closer to the Fermi level compared to the HOMO position (1.40 eV) of the thicker (10 nm) film. This is a typical observation as the photohole screening further from the metal substrate is less efficient,[147] which is reflected in the higher BE for larger film thicknesses.[148]

A summary of the light induced energy level scenarios for DAE1 molecules on Au (thin and thick film) is depicted in Figure 5.7. Notably, the deposition of ultrathin DAE1-c and DAE1-o films reduced the ϕ of the metal surface (4.70 eV) by 0.22 eV and 0.12 eV,

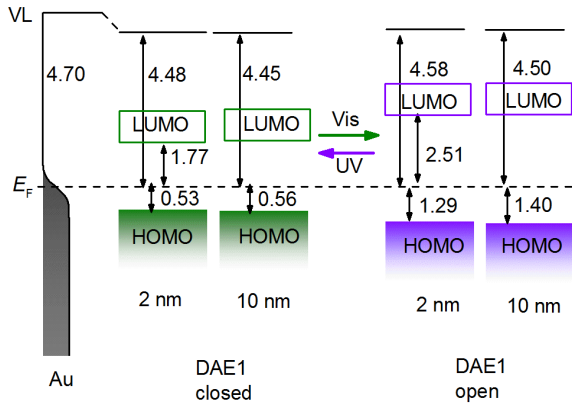

Figure 5.7. Switching-induced energy level alignment diagram of closed and open DAE1 films on Au surfaces, as determined from UPS in Figure 5.5 and Figure 5.6. The positions of LUMO levels were calculated using the transport gaps of DAE1 molecules.

respectively, which is ascribed to the "push-back" or "cushion effect".[59] For thicker films, no further changes in work function are observed, as a monolayer is sufficient to settle the push-back effect. By comparing the ELA between the Au/DAE1-o and Au/DAE1-c interface, one finds that the position of DAE-c HOMO onsets (0.53 eV BE) lies much closer to the Fermi level of the Au substrate, than that of DAE1-o (1.29 eV). The corresponding charge injection barriers, i.e., HOMO to E_F difference and LUMO to E_F difference at the Au/DAE1 interfaces can thus be efficiently controlled in a dynamic manner by illumination with light of appropriate energy (UV and visible light).

To study the ELA at the organic semiconductor/DAE1 interfaces, i.e., P3HT/DAE1 and N2200/DAE1, DAE1 molecules were sequentially deposited on top of the polymer layers. After each step of deposition, samples were measured with UPS, corresponding spectra shown in Figure 5.8. Figure 5.8a displays the thickness dependent UPS spectra of DAE1-o deposited on P3HT. The valence band onset of P3HT is at 0.25 eV BE (Fermi level pinned due to its low IE of 4.60 eV compared to the high work function of the PEDOT:PSS substrate (5.0 eV). The deposition of up to 2 nm DAE1-o on top of P3HT resulted in an attenuation of P3HT features, and the emergence of features centered at 2 eV and 3.8 eV BE, which are attributed to the valence levels of DAE1-o. Notably, the valence band onset of P3HT remained fixed at 0.25 eV BE and the ϕ remained constant, indicating weak interaction at the P3HT/DAE1-o interface. Increasing the coverage to 5 nm allowed the observation of a clearly discernible DAE1-o HOMO emission, with its onset at 1.51 eV BE, with yet constant ϕ. Given that the IE of DAE1-o, deduced from UPS above, is ~5.8 eV, its electron affinity, determined by considering the transport gap,

is ~2.0 eV. Prior to contact with P3HT, the Fermi level (P3HT work function: 4.35 eV) lies well within the band gap of DAE1-o, thus leading to the observed vacuum level alignment. Subsequently, the P3HT/DAE1-o sample was irradiated using UV light for 240 s, and DAE1-c molecules were thus formed with the HOMO level onset at 0.8 eV BE. By fitting the spectrum, it is possible to quantify the switching efficiency, which is the same as on Au substrate (inset of Figure 5.8a).

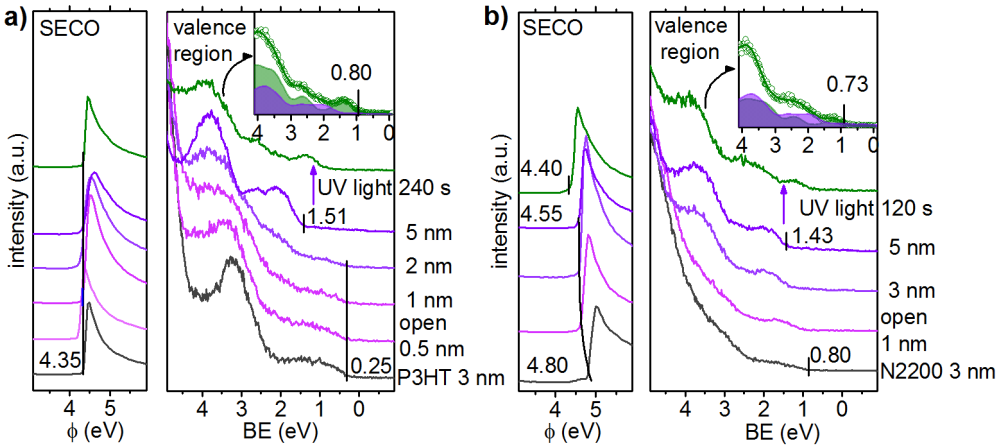

Figure 5.8. UPS spectra (valence and SECO regions) of DAE1-o films with incremental thickness on a) P3HT and b) N2200, and light switching induced changes. Inset displays the decomposition of the UPS spectra after UV light illumination as shown with arrows. The spectrum is fitted with the components of open and closed forms.

In contrast, the deposition of DAE1-o on N2200 (n type semiconductors) gave rise to a small shift of the sample work function (Figure 5.8b) towards lower values, indicating the formation of an interface dipole at the N2200/DAE1-o interface. However, no valence spectra shifts were observed with increasing deposition thickness. When the deposition thickness reached 5 nm, the obtained ϕ and HOMO onset position of DAE1-o were 4.55 eV and 1.43 eV, respectively. After UV light irradiation, DAE1-c conformers on N2200 were formed with a switching efficiency of 50% (inset of Figure 5.8b), and not only did the HOMO onset change from 1.43 eV to 0.73 eV (as expected), but also the ϕ further decreased by 0.15 eV to 4.4 eV. Since the HOMO level of DAE1 is quite far from E_F in both conformations, it is not very likely that Fermi level pining occurs (yet, it is not fully ruled it out), we estimate whether changes of the molecular dipole moment due to

the photochromic ring-opening/closure reaction could give rise to the observed ϕ change. We use the Helmholtz equation described in equation 2.29:

$$\Delta\phi = \frac{en\Delta\mu_{DAE}}{\varepsilon_0\varepsilon_r} \quad (5.1)$$

where e is the elementary charge, n is the surface dipole density (1 molecule nm^{-2}), $\Delta\mu_{DAE}$ is the change of the dipole moment perpendicular to the surface (1.2 Debye per DAE1 molecule, as shown in the last section), ε_0 is the vacuum permittivity, and ε_r is the relative dielectric constant. Assuming that all molecules are oriented with their dipole moments perpendicular to the surface, the calculated work function change ($\Delta\phi$) is 0.3 eV, only 0.1 eV larger than the experimentally observed value. This suggests that indeed a change of the molecular dipole can explain the observed ϕ change. However, it is unlikely that all the molecules have the same orientation, despite a preferential orientation that may persist.

To discuss the functionality of the two organic semiconductor/DAE1 interfaces, it was plotted in Figure 5.9 the energy level diagram, whose results were obtained from UPS and IPES.[121,149] In Figure 5.9a, it is observed that a vacuum level alignment prevails for both open and closed DAE1 on P3HT. From the estimation of molecular dipole moments above we conclude that no preferential orientation of the switches occurs. When DAE1-o is in contact with P3HT there is a huge energy difference (1.26 eV) between the polymer valence band edge and the molecular HOMO level such that hole-transfer from P3HT to DAE1-o is largely suppressed. When the molecule is switched into its closed form, the HOMO level moves much closer to the valence band and hole-transfer becomes improved, yet the energy offset (0.55 eV) is still substantial. Conversely, the conduction band edge of P3HT (2.35 eV above E_F) and the LUMO level of DAE1-o (2.34 eV above E_F) are in resonance, enabling good electron transfer; when switched to the closed form the LUMO level moves to 1.46 eV above E_F and electron transfer from the molecule to the polymer becomes inhibited. The N2200/DAE1-o interface is a Type-I heterojunction with substantial energy offsets (several 100 meV) between the hole and electron transport levels (see Figure 5.9b), implying very inefficient charge transfer from the polymer to the

molecule. However, upon switching DAE1 into its closed form, the respective transport levels become almost resonant in energy, i.e., the energy offset between conduction band edge and LUMO level is 0.6 eV and that between valence band edge and HOMO level is 0.07 eV, enabling facile electron and hole-transfer across the junction. Consequently, the energy level alignment between the organic semiconductors and the DAE1 photochromic switch can be altered over a very wide range by appropriate light stimuli.

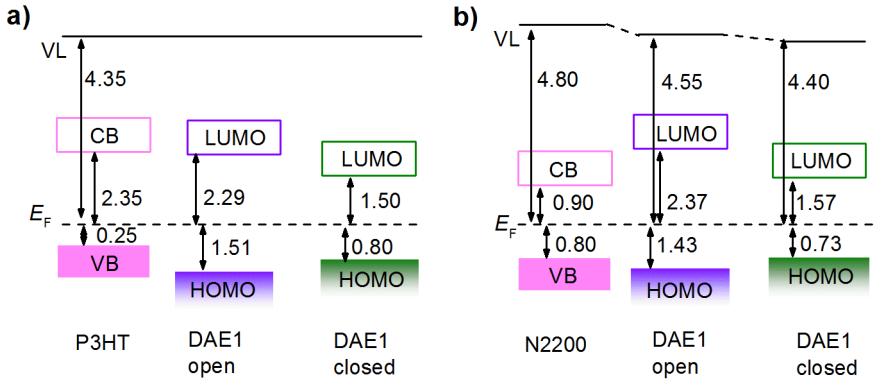

Figure 5.9. Schematic energy level diagrams of a) P3HT/DAE1 and b) N2200/DAE1 interfaces. The energetic positions of VL and HOMO (VB) onset relative to E_F were derived from UPS measurements; while CB onsets of P3HT and N2200 were calculated by considering the transport gaps. The LUMO onsets of DAE1-o and DAE1-c films were calculated by using their charge transport gaps, which were measured by UPS and IPES.

Conclusion

Using photoemission studies, it is shown that how the interfacial level alignment between thin films consisting of the photochromic molecular switches DAE1 and Au electrodes as well as two polymeric semiconductors (p-type P3HT and n-type N2200) can be modulated by light. Switching was achieved *in situ* by the irradiation with UV and visible light. First, it is demonstrated that switching between open and closed forms of DAE1 on Au is operative, with high switching yields for both bulk as well as approximately monolayer thin molecular films. While switching-induced work function changes are negligible, the HOMO level onset position of DAE1 varies by 0.8 eV with respect to the Au Fermi level between the two DAE isomers. Quantitative and fully reversible switching was also achieved for DAE1 on the two polymers. The charge transfer functionality of these junctions can be substantially modified by optical switching of DAE1, ranging from

charge blocking to almost resonant energy levels for both, electrons and holes (in the case of N2200).

5.2 Diarylethene Monolayer on Zinc Oxide

In the previous section, it was demonstrated that the application of DAE thin films can indeed tune the ELAs at both metal/organic and organic/organic interfaces. However, since DAE molecules are physisorbed onto the (in)organic surface, it will be problematic to apply such thin films into devices as they will be "washed away" when spin-coating organic layers on top. It is thus necessary to introduce an anchoring group to photoswitches so that they can chemisorb on the surface self-assembly. The deposition of chemisorbed SAMs is a powerful and universal approach to fine-tune the desired electronic properties of surface and interfaces.[150] As a result of SAM modification, molecules are covalently bound to the surface in an ordered manner. On the one hand, this enables tuning the surface potential with SAM-related surface dipoles,[67] thus leading to the optimization of interfacial energy levels favored for charge injection and extraction. On the other hand, the incorporation of photochromic molecules (e.g., diarylethenes, azobenzenes) into the SAM provides a dynamic method to switch the electronic properties through simple external stimuli.[20,151] The underlying mechanism is that, those molecules can switch reversibly between their two isomers upon illumination of light with different wavelength. As discussed in the last chapter, switching between the two forms fundamentally changes the electronic properties of the molecules.

In this contribution, the application of DAE photoswitches was extended to hybrid organic/inorganic interfaces by considering a metal oxide semiconductor as inorganic component. This part is adapted from the already published papers.[152] It is demonstrated that the energy level modification upon light-induced switching can be applied to ZnO, which is a superior wide-gap semiconductor due to its high electron mobility, high structural quality, and easy processibility, and can serve as transparent electrode when highly doped.[153–155] To form a layer a dense and stable SAM on the ZnO surface, a solution-based approach that has proven to result in covalently bound molecules on metal

oxides was employed. The PA-DAE derivative was synthesized (shown in Figure 5.10a, see also Figure 4.1 for molecular structures) for the assembly on ZnO crystal surfaces, i.e., ZnO(0001) and ZnO(000-1).

The interface composition, electronic structure, and switching properties were investigated by PES studies and substantiated by DFT calculations. The chemical bonding of the PA anchoring group was retrieved from the fitting of O1s core level spectra, indicating the formation of mixed bidentate and tridentate binding. The quantification of core level spectra supports the presence of a densely packed SAM on both ZnO surfaces. After the formation of the SAM, it was observed a significant work function increase, which is attributed to the introduction of a surface dipole, as supported by DFT calculations. Upon *in situ* illumination with UV and green light for inducing the switching process, respectively, the SAM valence levels change substantially, foremost, the HOMO level of PA-DAE shifts by 0.7 eV with respect to the Fermi level. These findings prove the feasibility of light-controlled energy level alignment tuning at hybrid organic/inorganic interfaces and open up the possibility to fabricate multifunctional optoelectronic devices based on ZnO that employ light as remote stimulus.

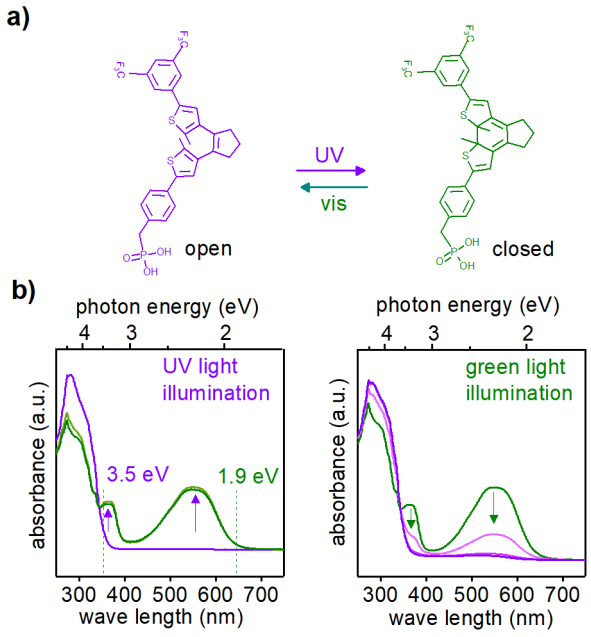

Figure 5.10. a) Chemical structure of the phosphonic acid diarylethene (PA-DAE) molecule in its open and closed form. b) Change of the UV-vis absorption spectra of PA-DAE in THF solution upon illumination with UV (λ=365 nm) and green (λ=565 nm) light until reaching the photostationary state; the illumination time for UV and green light was 60 s each.

5.2.1 Experimental Characterizations

The switching properties of PA-DAE was first characterized by UV-vis spectroscopy. As shown in Figure 5.10b in the bottom panel,

the spectrum of PA-DAE under its open form (PA-DAE-o) exhibits an absorption maximum in the UV region (violet line). Upon UV illumination with a wavelength of 365 nm for 60 s, the shape of the spectrum changes dramatically with the appearance of new absorption features in the green wavelength region (560 nm), indicating the formation of closed PA-DAE molecules (PA-DAE-c). The PA-DAE switches were then illuminated with green light (565 nm) in order to trigger a ring-opening reaction (see the right panel). After ca. 60 s of green light illumination, the absorption peak in the green region disappeared almost completely as indicated in green arrows. This points to that the PA-DAE was back to its open forms with very high switching efficiency. Therefore, it is proved that PA-DAE shows a reversible photoswitching upon UV and green lights illumination. The molecules are then deposited onto ZnO for further electronic characterizations.

Surface morphology of the SAM

The SAMs were fabricated by following previously established procedures (details see section 4.1.3).[127] Three deposition cycles of PA-DAE on ZnO were repeated to increase both the coverage and the homogeneity of the monolayer being formed. At the same time, this minimizes the surface etching effect due to short immersion time in solution (details see the sample fabrication section).[156]

Figure 5.11 and 5.12 show AFM images of the clean polar ZnO surfaces before (Figure a-c) and after (Figure d-e) SAM modification. On ZnO(0001) as shown in Figure 5.11, the height image of the clean ZnO surface in Figure 5.11a exhibits the presence of atomically flat terraces. A line profile over several terraces points to step-heights of multiple Zn-O layer heights (ca. 2-4 *h*, in which *h* is half of the unit cell height), as typically observed for polar ZnO crystal surfaces.[157] After SAM modification, the surface terrace features of the ZnO are still clearly observable in the height image (Figure 5.11d). This indicates that the surface modification is achieved without apparent etching of the surface. Furthermore, the homogenous phase image indicates a uniform coverage by the PA-DAE SAM.

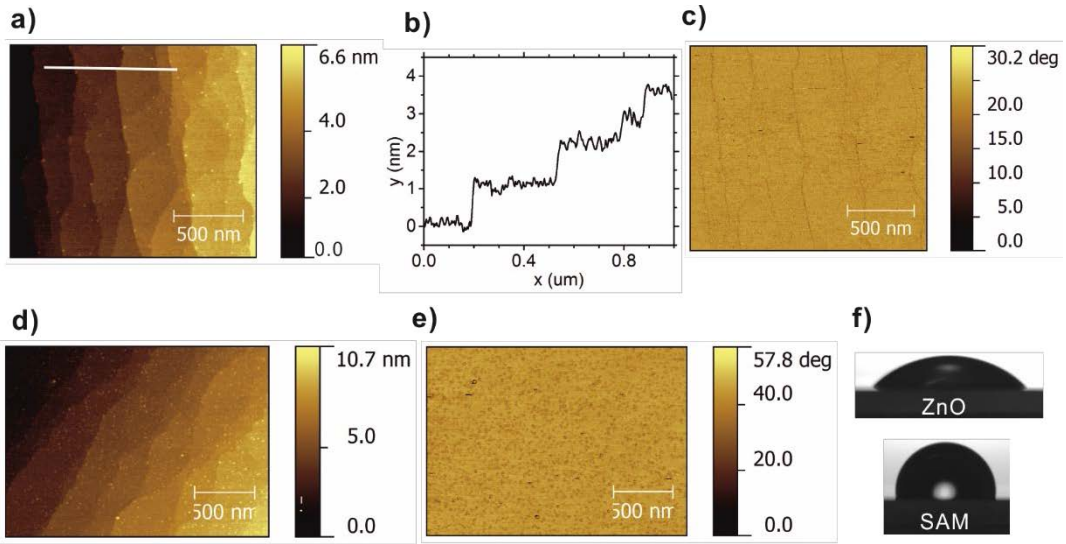

Figure 5.11. a) AFM height and c) phase images of the bare ZnO(0001) surface. b) Cross-section along the line in Figure 5.11 a. d) AFM height and e) phase images of the PA-DAE-o modified ZnO(0001) surface. f) Water contact angles on ZnO(0001) and PA-DAE SAM on ZnO(0001).

Water contact angle measurements were carried out in order to obtain further information on the coverage of the SAM on ZnO. As shown in Figure 5.11f, the contact angle of the ZnO surface is significantly modified by the SAM, and it is increased from 46.5° ± 1.5° to 101.3° ± 2.0°. According to Cassie's law, the static contact angle satisfies the equation (1):[158]

$$cos\theta_{SAM} = f\left(cos\theta_{ref} - cos\theta_{ZnO}\right) + cos\theta_{ZnO} \qquad (5.2)$$

where f denotes the surface fractional coverage of the SAM; θ_{SAM} the contact angle of the SAM modified ZnO, θ_{ref} and θ_{ZnO} are the contact angle of the complete reference layer and the bare ZnO, respectively. Since no reference data for a complete monolayer of the PA-DAE SAM exist, it is assumed a reference angle of dense SAMs of similar fluorine-terminated PA SAMs, which is more than 120°,[158,159] thus f is estimated of ca. 70% for PA-DAE SAM on ZnO(0001). Analogous results (with f = 68% coverage) were found for PA-DAE SAM on ZnO(000-1), for which the typical ZnO terraces also remain after PA-DAE modification (Figure 5.12). The estimated coverages for the PA-DAE SAMs on both polar ZnO surfaces are in agreement with those of other phosphonic acid based SAMs,[35,127] supporting a compact monolayer on both polar surfaces (note that the

molecular footprint area of DAE is larger than that of the reference SAM molecules used for estimating *f* above).

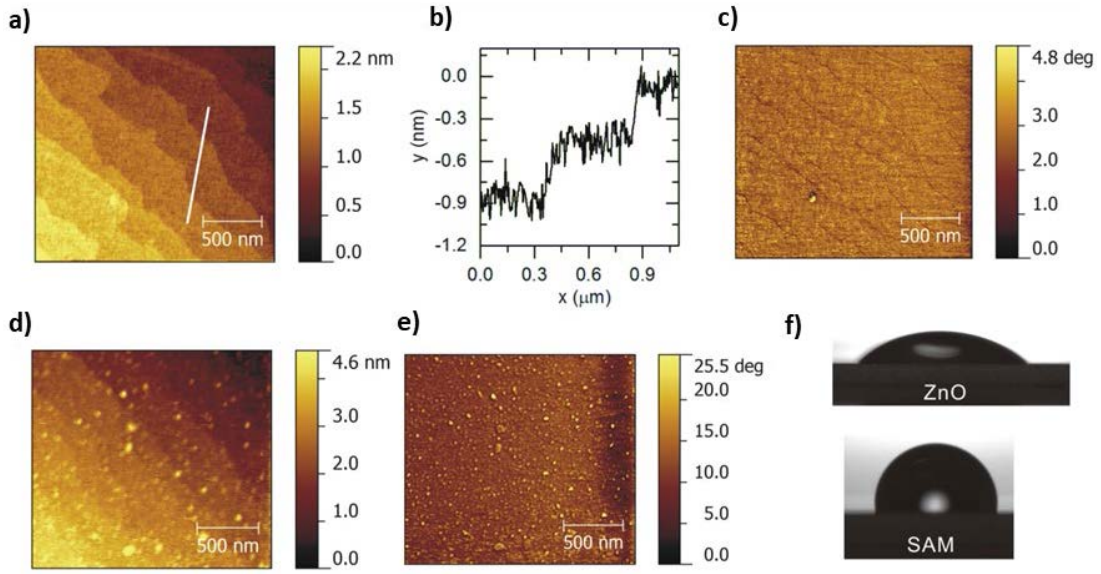

Figure 5.12. a) AFM height and c) phase images of the bare ZnO(000-1) surface. b) Cross-section along the line in Figure 5.12a. d) AFM height and e) phase images of the PA-DAE-o modified ZnO(000-1) surface. f) Water contact angles on ZnO(000-1) and PA-DAE SAM.

Bonding and electronic properties of the SAM on ZnO

XPS was performed to further quantify the coverage of the SAMs and to confirm a proper covalent bonding of the PA-DAE molecules on ZnO surfaces. The spectra were obtained using synchrotron radiation by setting the photon energy such that the photoelectrons are emitted with a kinetic energy of ca.100 eV; this ensures the highest surface sensitivity for the SAM. C 1s core level spectra were first recorded to check the effect of beam damage and photon-induced switching. As shown in Figure 5.13, the decomposition of C 1s spectra allows one to identify different chemical components of carbon existing in PA-DAE, i.e., carbon of the aliphatic chain (C-C/C-H) is located at 285.0 eV BE; carbon that binds covalently to P atoms of the phosphonate group (C-P) is at 285.8 eV BE; carbon that binds covalently to S (C-S) atoms is at 286.3 eV BE; carbon of the C-F3 tail group is at 293.3 eV BE. The calculated peak area ratios of the carbon components are in good agreement with the theoretical ones expected for PA-DAE on both faces, indicating no radiation damage during the XPS data acquisition.

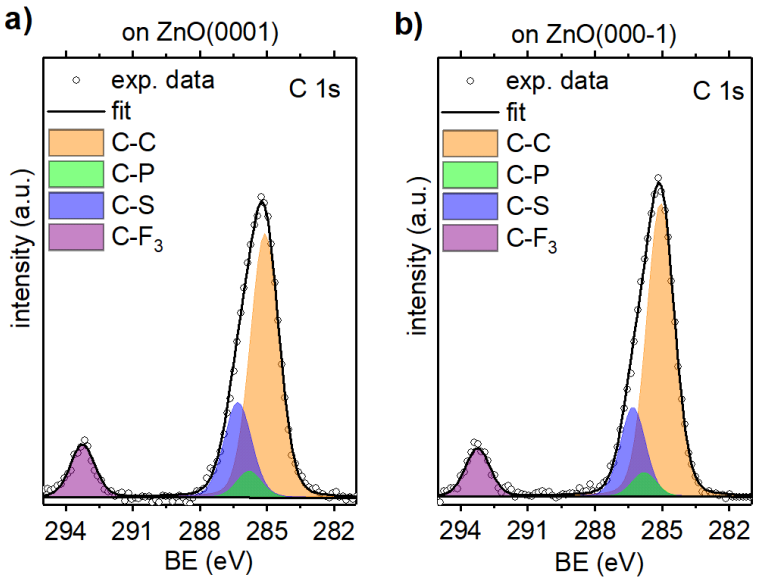

Figure 5.13. C 1s core level spectra of PA-DAE-o SAM on a) ZnO(0001), b) ZnO(000-1). The fitting of core level spectra (the dotted lines) shows that multi-chemical components (labelled with different colours) exist in the molecule.

Zn 3s + P 2p and O 1s spectra are shown in Figure 5.14. The bottommost Zn 3s spectrum is that of bare ZnO(0001); fitting of the spectrum locates the Zn 3s core level at 140 eV BE. For the sake of simplicity, only the Zn 3s core levels of ZnO(0001) are shown since for ZnO(000-1) the spectral features are fully analogous.[19] After SAM modification, the intensity of the Zn 3s peak is strongly attenuated for both polar ZnO surfaces (central and topmost spectra, respectively). The P 2p core level appears as rather sharp peak at 133.3 eV BE, attributed to the chemisorbed PA-DAE monolayer. An additional P 2p component is observed at higher binding energy (135.0 eV), which can be attributed to the presence of a small amount of physisorbed multilayers (both components fitted with Voigt profiles). Comparing the P 2p peaks for both ZnO surfaces, one observes a slightly lower contribution from physisorbed multilayers of PA-DAE on the ZnO(000-1) surface compared to ZnO(0001).

Moreover, by analysing the peak areas of Zn 3s and P 2p, one can estimate the molecular density of PA-DAE molecules on ZnO according to equation 5.3, which is based on a three-layer model (see 3.1 for theoretical details). This yields 2.2 $\pm$ 0.6 molecules nm^{-2} on ZnO(0001) and 2.1 $\pm$ 0.6 molecules nm^{-2} on ZnO(000-1), respectively.

$$\frac{I_P}{I_{Zn}} = \frac{N_P \sigma_P \lambda_{P,PA}}{N_{Zn} \sigma_{Zn} \lambda_{Zn,ZnO}} \frac{1-\exp(-d_{PA}/\lambda_{P,PA}cos\theta)}{\exp(-d_{PA}/\lambda_{Zn,PA}cos\theta)} \quad (5.3)$$

These values are reasonable in comparison to the packing density reported for dense alkyl and quaterthiophene phosphonic acid SAMs (with a smaller footprint area per molecule compared to DAE) on SiO_2 of ca. 5.4 molecules nm^{-2} and 4 nm^{-2}, respectively.[160] Also, the calculated densities are comparable to those of other phosphonic acid based SAMs, e.g., a ca. 2 molecules nm^{-2} coverage was reported for fluorinated alkyl and aromatic phosphonates on ZnO; due to the smaller footprint area of these molecules compared to DAE probably not densely packed SAMs.[35] The quantification of the core level spectra provides thus further evidence for densely packed SAMs on both polar ZnO surfaces.

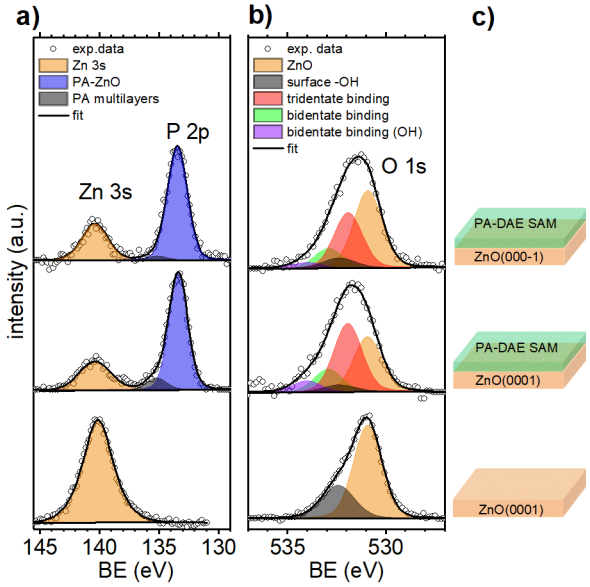

Figure 5.14. a) Zn 3s and P 2p b) O 1s core level spectra (background subtracted) of the unmodified (bottom panel), PA-DAE-o modified (middle panel) ZnO(0001), and PA-DAE-o modified (top panel) ZnO(000-1). The corresponding sample representation is illustrated in c). The fitting of spectra was based on pseudo-Voigt profiles.

O ls core level spectra were measured for studying the bonding of the SAMs on ZnO. As shown in Figure 5.14b, for identifying the different components in the O 1s core level region, we employed a fit model previously used by Timpel et al,[127] who observed differently bonded phosphonic acid on ZnO, i.e., mixed bidentate and tridentate. In analogy, the same binding energy for the individual core level components was adopted for this fit. The fitting of O 1s spectra reveals two coexisting binding modes of the phosphonate anchoring group to the ZnO surface. For the bare ZnO(0001) surface (bottom panel), one main peak at 531 eV BE with a shoulder at 532.5 eV is observed. The main peak is attributed to bulk oxygen, whereas the shoulder with

30 % of the peak area is attributed to surface hydroxyls (-OH).[19,161] After SAM modification, the intensity of O 1s from ZnO is markedly attenuated. The fitting of the O 1s spectrum (middle panel) identifies components at 532.0 eV and 533.0 eV BE, respectively, supporting the presence of both bidentate and tridentate binding. The peak area ratio of the tridentate to bidentate binding is ca. 2:1, indicating that the PA-DAE SAM on ZnO(0001) is preferentially bound as tridentate. Using the same procedure, for the PA-DAE modified ZnO(000-1), the same ratio (2:1) between tridentate and bidentate binding is obtained. However, the spectrum exhibits a relatively higher O 1s peak intensity from the bulk ZnO oxygen component compared to that of ZnO(0001). This indicates a weaker overlayer attenuation, which can be attributed to slightly lower SAM coverage in this case.

To characterize the valence electronic properties of the PA-DAE SAM, UPS measurements were performed. Figure 5.15 shows the UPS spectra of the bare and PA-DAE modified ZnO surfaces. The work function ϕ and onset of the valence band maximum (VBM) for the clean ZnO(0001) surface are 3.7 eV and 3.3 eV binding energy, respectively (see Figure 5.15a). The deposition of the PA-DAE SAM (originally in the open configuration) increases ϕ by 1.2 eV to 4.9 eV, as seen from the SECO; the low binding energy onset of the HOMO of the PA-DAE SAM is found at 1.5 eV BE. The SAM was then exposed *in situ* to UV light to induce switching from the open to the closed form. This resulted in substantial changes of the SAMs' valence features. A new low binding energy spectral feature with an onset at 0.8 eV BE emerged after 180 s UV light illumination (see the violet lines in Figure 5.15). This feature can unambiguously be attributed to the HOMO of PA-DAE-c molecules since similar changes were observed for the DAE1 films, as discussed in the last section. The HOMO level shift by 0.7 eV is also in quantitative agreement with the DFT calculated change of the HOMO level (0.7 eV) of a single molecule (*vide infra*). Subsequent illumination of the sample with green light results in a ring-opening reaction, which is manifested in UPS spectra by the disappearance of the peak with its onset at 0.8 eV, restoring the valence region spectral appearance to that observed initially with the HOMO level onset at 1.5 eV BE. Comparing

the two spectra of the open form (violet lines), it is unlikely that the switching efficiency reaches to unity, due to steric hindrance[28] or radiation (UV,VUV) induced photoquenching[162] in the densely packed monolayer.

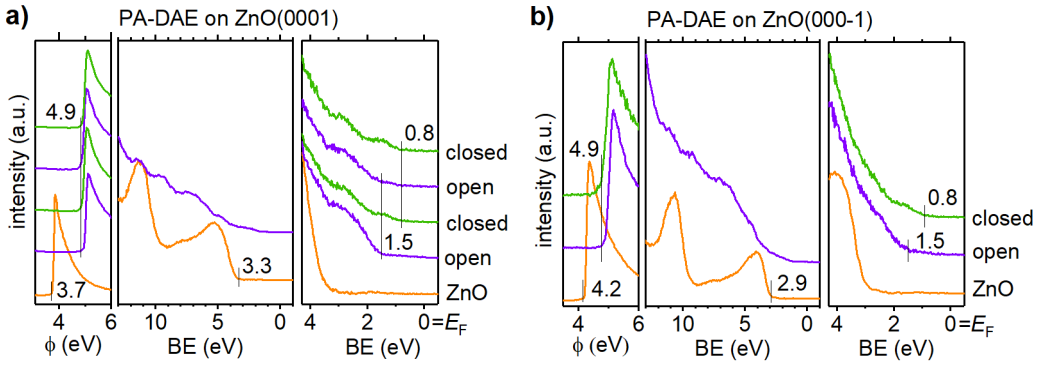

Figure 5.15. UPS spectra of the PA-DAE SAM on a) ZnO(0001) and b) ZnO(000-1). Upon illumination cycles of UV and green light (see main text). The left panel displays the SECO spectra, from which one can read the value of the sample work function (ϕ). The middle and right panels show the survey and zoom-in of the valence regions, respectively. The binding energy (BE) is set to zero at the Fermi level (E_F).

Notable SECO changes were not detectable during the photoswitching processes, which evidences that photoswitching has negligible impact on the work function. Subsequent repeating illumination by UV light (300 s) switched the SAM back to its closed isomer state as evidenced by fully reproducing the previously observed valence electronic features of PA-DAE-c. This implies that the SAM can be reversibly switched by simple light illumination at different wavelengths. The same switching also occurs for PA-DAE on ZnO(000-1) (see Figure 5.15b), for which the initial ϕ of the ZnO surface is 4.2 eV, and increases to 4.9 eV after the deposition of the SAM. Upon UV light illumination photoswitching is induced, resulting in a shift of the HOMO onset from 1.5 eV to 0.8 eV BE. However, the spectral features of the PA-DAE in the valence region are not as pronounced as on ZnO(0001). This might be related to some damage due to long time exposure to the He I light during these photoemission measurements, which could give rise to relatively poor switching yield on ZnO(000-1).

The interfacial ELAs derived from UPS for the frontier energy levels of PA-DAE with respect to the two polar ZnO surfaces was summarized in Figure 5.16.

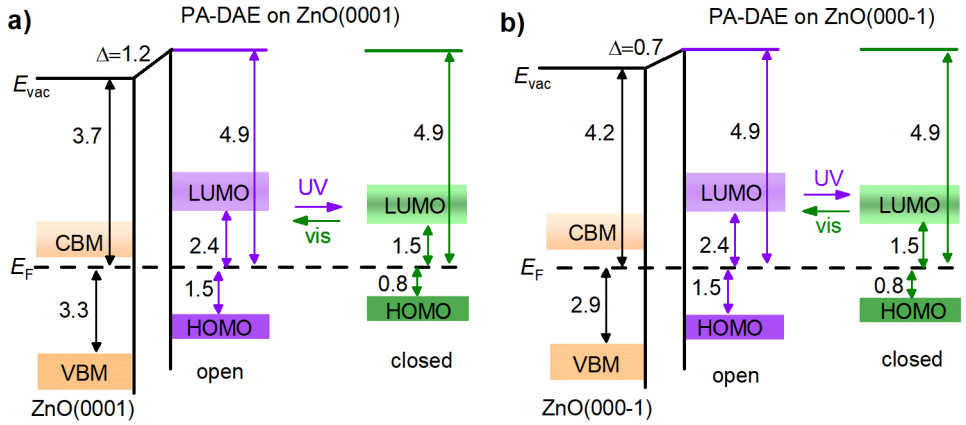

Figure 5.16. Schematic energy level diagrams of a) ZnO(0001)/PA-DAE and b) ZnO(000-1)/PA-DAE interfaces. The energy positions of the vacuum level (E_{vac}) and HOMO (VBM) relative to E_F were determined by UPS measurements; the CBM for both polar ZnO surfaces was obtained by adding the electronic gap. The LUMO onsets of PA-DAE-o and PA-DAE-c SAMs were obtained by assuming the known transport gap of related DAE derivatives reported in section 5.1.1.

For the unoccupied energy levels, the conduction band minimum (CBM) of the ZnO crystal is calculated according to its energy gap (3.4 eV);[163] the LUMO level of PA-DAE is obtained by referring to the transport gap of similar DAE1 as measured by IPES (see section 5.1.1). Since the molecular backbone is decoupled from the phosphonic acid anchoring group by a methylene unit, similar electronic properties are obtained for the molecules in solution and grafted on ZnO. The VBM of the bare ZnO(0001) and ZnO(000-1) is located 3.3 eV and 2.9 eV below the Fermi level, respectively, in line with literature values.[19] The deposition of the PA-DAE SAM increases the work function of ZnO(0001) by 1.2 eV and that of ZnO(000-1) by 0.7 eV due to interface dipoles (further discussed in the next section). For each isomeric form, PA-DAE exhibits the same level alignment with respect to E_F of the two ZnO polar surfaces. The energy offset between the HOMO of PA-DAE and the VBM on ZnO is significantly modulated by light illumination (increased by 0.7 eV going from the open to closed form). In parallel, the level offset between the PA-DAE LUMO and ZnO CBM is reduced by 0.9 eV when going from the open to the closed form.

5.2.2 Theoretical Calculations

Theoretical modelling was performed at the DFT level in order to further understand the electronic properties of the ZnO/PA-DAE SAM interface. The geometry optimization on the isolated PA-DAE molecules was carried out in Gaussian09 with the PBE functional. The total dipole moments (μ_{tot}) of the isolated PA-DAE-o and PA-DAE-c molecules are calculated to be -4.5 and -4.7 Debye (direction points downwards. See Figure 5.17), respectively. Such small changes should translate into a modest work function shift upon photoswitching, in line with previous findings in experiment that ϕ did not change notably upon switching. PA-DAE molecules were then grafted onto the ZnO surface to analyse the work function shift and valence electronic properties of the hybrid system in details.

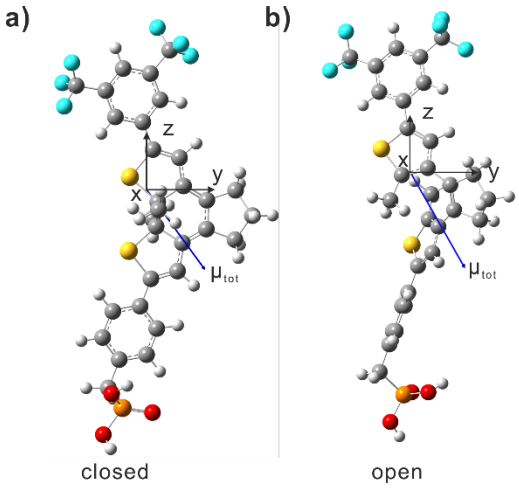

Figure 5.17. Molecular dipole moments for a) closed and b) open PA-DAE molecules, as calculated with the PBE functional and a 6-31G(d) basis set. The z-axis is along the direction perpendicular to the surface.

For the ZnO slab, according to the experimentally calculated coverage on both ZnO surfaces, an orthogonal structure made of 12 layers with its *a* and *b* lattice vectors of 9.75 Å and 5.63 Å, respectively, was built. The surface and bottom part of the ZnO slab are covered with -OH group and H atoms with 50% of coverage to prevent the "metallization effect"[134,164] and reflect the actual experimental conditions. Dipole-dipole interactions inside the unit cells possibly triggered by the use of PBC are also compensated by applying a dipole correction in the unit cell along the *z*-axis. This leads to a zero-electric field and a flat electrostatic potential in the vacuum region (see Figure 5.18). The calculated band gaps for ZnO(0001) and ZnO(000-1) slabs are 0.8 and 1.1 eV, respectively; this is too much smaller compared to experimental gaps around 3.4 eV, though without strong implications for the present purpose.

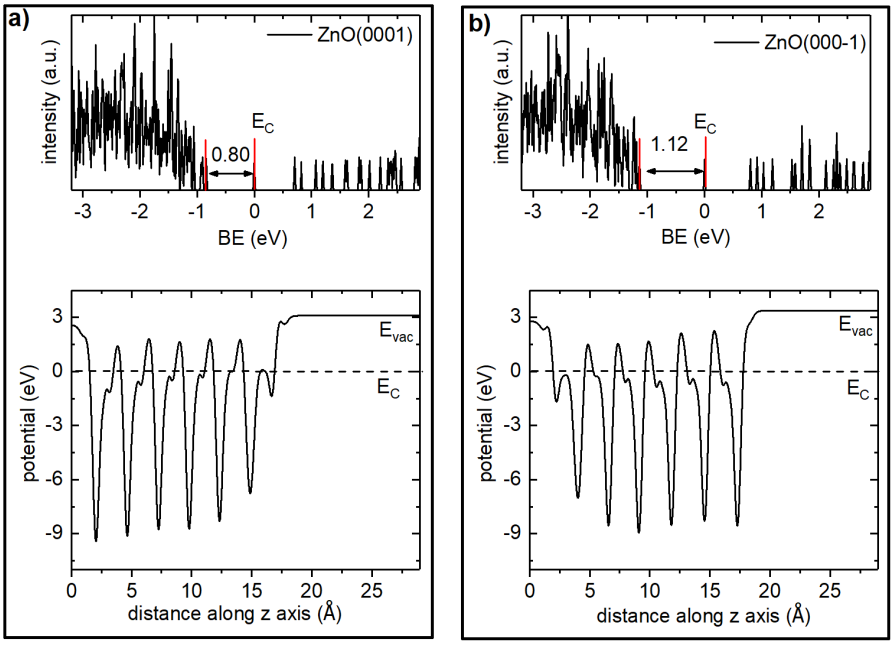

Figure 5.18. Total density of states (top) and plane averaged electrostatic potential (bottom) of a) ZnO(0001) and b) ZnO(000-1) unit cells. E_c serves as the reference of zero binding energy, the work function (ϕ_{bare}) of the slabs is given by: $\phi_{bare}=E_{vac}-E_c$.

Based on adsorption mechanisms of PA on metal oxides (equation 2.25), the adsorption of PA-DAE on hydroxyl-passivated ZnO(0001) or hydrogen passivated ZnO(000-1) is realized by removing one -OH and filling the vacancy with PA-DAE-o or PA-DAE-c molecule with a tridentate or bidentate binding. In this process, the leaving H from the PA reacts with the -OH desorbed from the surface to release a water molecule, as shown in Figure 5.19.[66] Thus, in the bidentate mode, one hydrogen atom remains attached to the phosphorous atom while the other is removed to form a water molecule. In the tridentate mode, the hydrogen left on the phosphorous atom migrates to the ZnO surface to generate three Zn-O bonds (see Figure 5.19).

First, the adsorption energies for different binding geometries were calculated in order to evaluate the stability of SAMs on ZnO. This was done at the DFT/PBE level using PBC in order to create an infinite two-dimensional slab. The adsorption energies are calculated according to equations 5.4 and 5.5 by comparing the difference between energies of the product (SAM + H_2O) and the sum of the energies of the free isolated molecule and free bare ZnO:

For bindentate:

$$\Delta E_{ads} = E_{SAM} + E_{H_2O} - (E_{mol} + E_{ZnO}) \quad (5.4)$$

For tridentate:

$$\Delta E_{ads} = E_{SAM-H} + E_{H_2O} - (E_{mol} + E_{ZnO}) \quad (5.5)$$

The calculation shows that the tridentate configuration is more stable by 1.4 eV per molecule than the bidentate form,[152] which is reasonable in view of the additional Zn-O bond formed. The higher stability of the tridentate bindings agrees with the O 1s spectra (see Figure 5.14), indicating that more tridentate species are observed. The co-existence of bidentate and tridentate motifs is thus probably driven by kinetic rather than thermodynamic effects.

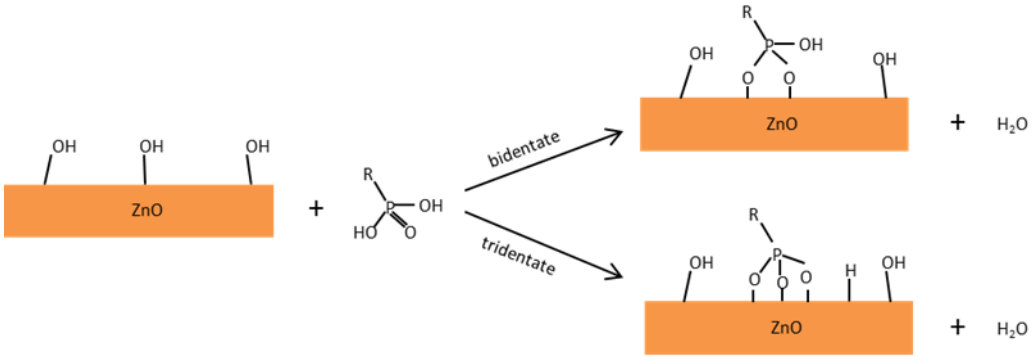

Figure 5.19. Schematic illustration of the surface adsorption of the PA molecule on polar ZnO surfaces. In the bidentate mode, two oxygen atoms are bonded to the ZnO surface; one hydrogen atom is lost via the formation of a water molecule, another one remians attached to PA. In the tridentate mode, three oxygen atoms are bonded to the ZnO surface. Two hydrogen atoms are removed from the PA; one reacts with the surface –OH to form a water molecule, while the other is attached to the surface.

As described in previous studies,[73,164] the modification of the work function originates from a vacuum level shift generated by a dipole moment perpendicular to the surface due to the adsorption of the SAM. The surface dipole can be attributed to three different contributions: *i*) the formation of a bond dipole (*BD*) at the ZnO/PA-DAE SAM interface due to charge reorganization; *ii*) the intrinsic dipole (ΔV_{SAM}) of the molecular backbone of the adsorbed SAMs, and *iii*) the desorption of the OH group and possible surface structural relaxation effects upon chemisorption ($\Delta\phi_{ZnO}$). Taking into account these

contributions, the total work function change $\Delta\phi$ between the SAM-covered ZnO and the bare ZnO substrate is given by:

$$\Delta\phi = BD + \Delta V_{SAM} + \Delta\phi_{ZnO} \quad (5.6)$$

Figure 5.20 summarizes the charge density distribution Δρ upon SAM formation along the *z*-axis and the resulting BD potential for PA-DAE on ZnO(0001) and ZnO(000-1). Δρ is calculated by the following Equation:[66,134]

$$\Delta\rho = \rho_{SAM} + \rho_H - \rho_{mol} - \rho_{ZnO} \quad (5.7)$$

where ρ_{SAM} represents the charge density of the full ZnO/PA-DAE interface in its final geometry; ρ_{ZnO} is that of the ZnO surface in its final geometry (without a hydrogen attached for the bidentate geometry and with for the tridentate binding) after removal of the SAM (and without the hydroxyl initially removed); ρ_{mol} is the charge density of the neutral molecule and ρ_H is the charge density associated to the hydrogen atom frozen in its position within the molecule prior to its elimination for the bidentate geometry, together with the density associated to the hydrogen atom transferred to the surface for the tridentate geometry. On that basis, the *BD* potential is evaluated by solving the Poisson's equation (see equation 2.27). The transfer profiles of $\Delta\rho$ show that a charge transfer occurs from the ZnO slab to the PA-DAE molecule. This charge transfer is localized between the top of the ZnO surface and the anchoring PA group of the SAM and rapidly decays in both adjacent regions (as indicated by dashed lines for the interface atoms), thus pointing to the formation of a covalent bond between the PA and top Zn atoms. a Bader charge population analysis (see reference[152]) indicates that the amount of charge transfer is 1.1 |e| for the tridentate binding and 0.7 |e| for the bidentate binding on both ZnO slabs. However, the magnitude of BDs between the bidentate and tridentate modes does not vary too much. Furthermore, it is shown that switching the PA-DAE between its open and closed forms does not significantly impact the amount of charge transfer, which implies that the magnitude of BD is weakly affected (around 0.2 eV) for a given binding mode.

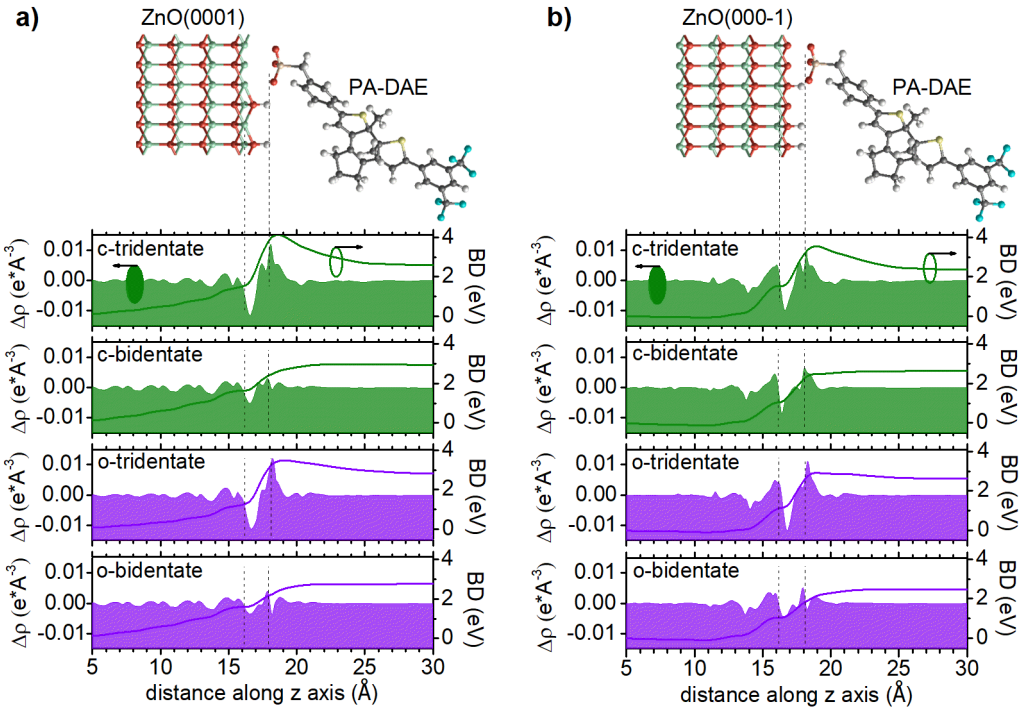

Figure 5.20. Plane averaged charge density difference (Δρ) and corresponding bond dipole (BD) potential for a) PA-DAE on ZnO(0001) and b) PA-DAE on ZnO(000-1), respectively. The positions of the topmost Zn layer in ZnO and the O layer in PA-DAE are indicated by the vertical dashed lines. c-tridentate refers to PA-DAE-c in tridentate binding and c-bidentate to PA-DAE-c in bidentate binding. The same terminology is used for the case of o-tridentate and o-bidentate.

To calculate the backbone contribution (ΔV_{SAM}) to the total work function shift, an isolated monolayer of PA-DAE molecules was built with the same geometry as that on the ZnO surface and with hydrogen atom(s) added to make the system neutral; then the plane-averaged electrostatic potential across this organic layer can be computed. For evaluating $\Delta\phi_{ZnO}$, the equation $\Delta\phi_{ZnO} = \phi' - \phi_{bare}$ was used, where ϕ_{bare} is the work function of the relaxed ZnO surface originally covered with 50% of -OH or hydrogen atoms and ϕ' is the work function of the ZnO slab after removal of the SAMs and of the transferred hydrogen in the case of the tridentate binding (there is thus one less OH group on the ZnO surface when computing ϕ'). The total work function shifts and its three components are summarized in Table 5.1.

	ΔV_{SAM}	*BD*	$\Delta\phi_{ZnO}$	$\Delta\phi$	$\Delta\phi_{avg}$
On ZnO(0001)					
c-tridentate	0.8	2.6	-2.2	1.2	1.2
c-bidentate	0.7	2.8	-2.3	1.2	
o-tridentate	0.8	2.8	-2.2	1.4	1.3
o-bidentate	0.7	2.7	-2.3	1.1	
On ZnO(000-1)					
c-tridentate	0.8	2.4	-2.5	0.7	0.7
c-bidentate	0.7	2.6	-2.7	0.6	
o-tridentate	0.7	2.6	-2.5	0.8	0.7
o-bidentate	0.7	2.5	-2.6	0.6	

Table 5.1. Individual contributions to the total work function shift ($\Delta\phi$) upon deposition of PA-DAE SAMs. The average values ($\Delta\phi_{avg}$) of $\Delta\phi$ are calculated by considering the ratio of tridentate to bidentate binding derived from XPS. All values are in eV.

The small variation of ΔV_{SAM} between the tridentate and bidentate is related to an orientational change of the molecular backbone during the relaxation process. Considering the ratio of tridentate to bidentate binding derived from XPS, the average work function difference ($\Delta\phi_{avg}$) is calculated on ZnO(0001) to be 1.2 eV for the PA-DAE-c SAM and 1.3 eV for the PA-DAE-o SAM. The results match the experimental data very well in a quantitative manner and confirm that no obvious work function changes take place during the photoswitching. Interestingly, the similar values of $\Delta\phi$ for the bidentate and tridentate modes result from a cancellation of the changes in *BD* and $\Delta\phi_{ZnO}$. On ZnO(000-1), $\Delta\phi_{avg}$ for both PA-DAE-o and PA-DAE-c SAMs is calculated to be 0.7 eV, in full agreement with the UPS results. The calculated $\Delta\phi_{avg}$ on ZnO(000-1) is 0.5 eV smaller than on ZnO(0001) due mostly to a different surface reconstruction upon SAM grafting ($\Delta\phi_{ZnO}$).

Conclusion

In this section, phosphonic acid substituted DAE molecular switches were covalently bound to polar ZnO surfaces [ZnO(0001) and ZnO(000-1)] under the form of self-assembled monolayers; the photochromic monolayer is then used to reversibly modify

the electronic properties at the hybrid interface by light stimuli. A comprehensive characterization of the clean and modified ZnO by contact angle, AFM and XPS allows one to conclude that a densely packed monolayer of PA-DAE is formed on both polar ZnO surfaces. The chemical binding at the interface was confirmed in mixed bidentate and tridentate form by the deconvolution of core level (O 1s) XPS spectra. After SAM modification, the work function measured by UPS increased by 1.2 eV for ZnO(0001) and 0.7 eV for ZnO(000-1), respectively. The work function increase is due to the bond dipole localized at the phosphonate anchoring group, the change of the ZnO surface charge distribution due to water release due to bond formation, and the molecular dipole moment, as retrieved from DFT calculations. Upon alternating illumination with ultraviolet and green light, respectively, sizeable energy shifts were observed for the HOMO and LUMO levels of the PA-DAE molecules with respect to the Fermi level of ZnO, 0.9 eV for the LUMO and 0.7 eV for the HOMO. This can be exploited to reversibly switch the energy level alignment at hybrid ZnO/PA-DAE interfaces in device structures by optical means.

5.3 Diarylethene Monolayer on Indium-Tin-Oxide

In the last section, it was proved that the chemical modification of the metal-oxide surface with photoswitchable SAMs was feasible. The surface electronic properties of ZnO can be tuned by PA-DAE photoswitches reversibly and dynamically upon light illumination. It is thus expected that such PA-DAE SAMs will have similar effects on ITO surfaces, which has been extensively used as transparent electrodes in optoelectronic device.[165,166] A dynamic control of the electronic landscape of electrode surfaces opens a gate to achieve multifunctional natures in such devices. Thus in this section, the investigation will focus on the modification of transparent ITO electrode with PA-DAE photoswitches. It is proved that the electronic properties of the ITO surface can be dynamically and reversibly tuned by the PA-DAE SAM upon light illumination. Following previous method applied on ZnO,[152] the SAMs for ITO were also fabricated with three cycles. Its

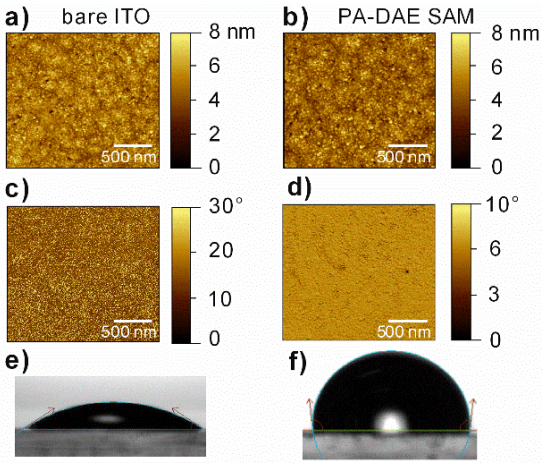

Figure 5.21. AFM of height and phase images for the bare ITO (a,c) and PA-DAE SAMs (b,d) sufaces. Water contact angles of corresponding surfaces are shown in e) for bare ITO and f) for SAM.

surface morphology was characterized by AFM and water contact angle. The chemical bonding of the phosphonic acid linker was confirmed by measuring O 1s core level spectra with XPS. Different from the binding on the ZnO surface, where both bidentate and tridentate bindings are energetically resolved, the decomposition of O 1s spectra shows these two binding modes are at the same biding energy position, this is further supported by DFT. The orientation of the PA-DAE molecules was characterized angle-dependent XAS. The work function modification and valence electronic properties were investigated by UPS. Upon illumination of the SAM, a reversible shift of frontier occupied/unoccupied levels was observed by ca. 0.7 eV, and concomitantly small change of the work function ϕ by ca 60 meV. These findings prove the feasibility of dynamical energy level tuning of the ITO electrode, which will be used to fabricate multifunctional optoelectronic devices containing the ITO/PA-DAE systems.

Surface morphology

The surface morphologies of both bare ITO and PA-DAE SAM were characterized by AFM (see Figure 5.21). For bare ITO, the height image of the surface shows small grains (average size ~40 nm in diameter) with a roughness (root mean square, RMS) of 0.7 nm. After the SAM modification, the surface roughness does not change too much (0.4 nm); the grains of ITO are well preserved, and no island formation or multilayers are observable in the height image. Combining the height and the homogenous phase image, it can be concluded that the surface modification is in consistence with an uniform monolayer coverage. In order to obtain further details about the coverage, the wettability change was measured using water contact angle measurement before and after surface

modification. As shown in Fig. 5.21e and f, the water contact angle increases significantly from 33.1° ± 1.0° (for bare ITO) to 97.1° ± 1.0° (for SAM modified ITO). The same observation has already been found for PA-DAE SAM on ZnO, where water contact angle increases from 46° to 101°. Such a wettability change further supports a densely packed coverage on the ITO surface.

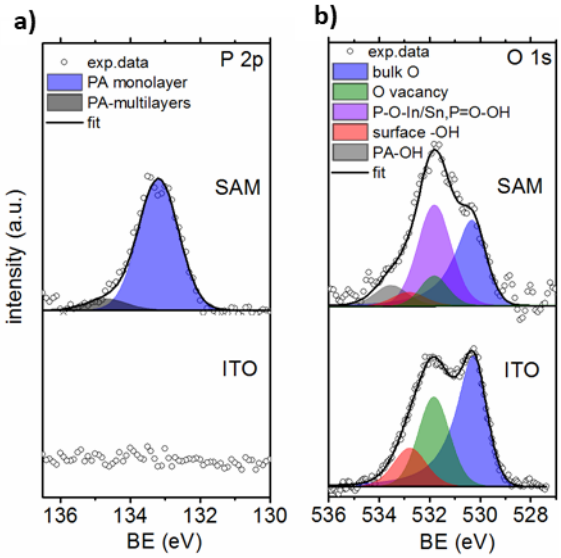

Figure 5.22. a) P 2p and b) O 1s core level spectra for bare ITO and PA-DAE SAM. The decomposition of the P 2p spectra shows that PA-DAE molecules primarily form a monolayer; the decomposition of the O 1s spectra reveals the interface bonding of the SAMs.

Chemical bonding

To further characterize the quality of the SAMs and to confirm a chemical bonding of PA-DAE to ITO, XPS measurements were performed with synchrotron light, which enables one to tune the photon energy with the highest surface sensitivity. The beam damage on the organic molecules can be neglected by analyzing the C 1s spectra (not shown here, since they were already shown in Figure 5.13 on ZnO). As shown in Figure 5.22a, first, the P 2p core level spectra were recorded to ensure a presence of phosphonic acid. One bare ITO surface (lower panel), no signal can be detected. After surface modification (upper panel), the P 2p peak is clearly detectable. Moreover, two components are resolved from the spectral fitting: The one at 133.2 eV BE, is attributed to the chemisorbed PA-DAE monolayer.[127] An additional P 2p component at higher binding energy (135.0 eV) is attributed to the presence of a small amount of physisorbed multilayers. Figure 5.23 shows the F 1s and In 3d core level spectra of the SAM measured with the Al K_α source. The packing density of PA-DAE molecules is further analyzed by comparing the signal intensity of F 1s with In 3d (see Figure 5.23):

$$\frac{I_F}{I_{In}} = \frac{N_F S_{F1s}}{N_{In} S_{In3d}} \frac{1-\exp(-d_F/\lambda_F cos\theta)}{\exp(-d_{SAM}/\lambda_{In,SAM} cos\theta)} \qquad (5.8)$$

where S_{F1s} and S_{In3d} are the relative sensitivity factor (normalized to C 1s) of the F 1s and In 3d with values of 4.02 and 21.92, respectively, λ_F is the electron IMFP of the F 1s in the SAM, $\lambda_{In,SAM}$ is the electron IMFP of the In 3d in the SAM. The calculated surface coverage for the PA-DAE molecules is 2.0 ± 0.7 molecules nm^{-2}, comparable to previous results of PA-DAE on polar ZnO.[152]

O ls core level spectra were measured for analysing the chemical bonding of PA-DAE to ITO. Figure 5.22b summarizes the O 1s spectra of bare and PA-DAE modified ITO. In the case of bare ITO (lower panel), two spectral components are clearly resolved. According to previously DFT calculations,[68,167] these two components are attributed to *i*) ITO bulk oxygen at 530.3 eV (asymmetric peak due to energy loss); *ii*) surface oxygen vacancy at 531.8 eV. Furthermore, the fitting of the experimental data resolves one more component located at 532.8 eV BE; this peak is attributed to surface hydroxyl adsorptions. After SAM modification, the intensity of O 1s from bulk ITO is markedly attenuated, and there is a major intensity increase at ca. 531.7 eV BE (1.4 eV higher than the binding energy of bulk oxygen), the fitting of the spectrum attributes this component to the chemical bonding of PA (detailed binding modes will be discussed below). Additionally, a new component at higher binding energy (533.6 eV) are considered for the fitting (details will be discussed below) of the spectrum, which is assigned to the unreacted PA-OH groups. As reported in literatures,[68,69,168] different binding modes of PA have been identified to coexist on metal oxides. As for the PA-DAE SAM, it has been observed on ZnO that the tridentate and bidentate bindings coexist since both bindings are energetically stable. To

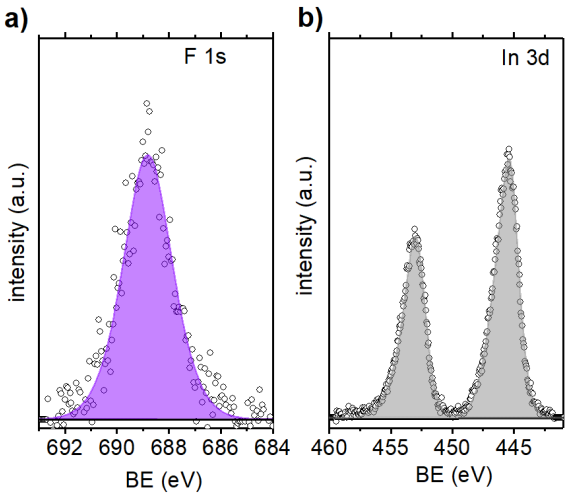

Figure 5.23. a) F 1s and b) In 3d core level spectra for PA-DAE SAM modified ITO measured with the photon energy of 1486.7 eV (Al K_α). The F 1s spectrum was fitted with a symmetric Voigt profile; while the In 3d spectrum was fitted with asymmetric profiles.

better resolve these binding modes on ITO, DFT calculations was further performed on the core level shift (CLS) of O 1s. Similar to the scenarios on ZnO, it has been assumed that PA-DAE molecules chemisorb on ITO surfaces in both bidentate and tridentate bindings. Thus for building the unit-cell, PA-DAE was grafted on ITO with both binding modes with a ratio of 1:1.

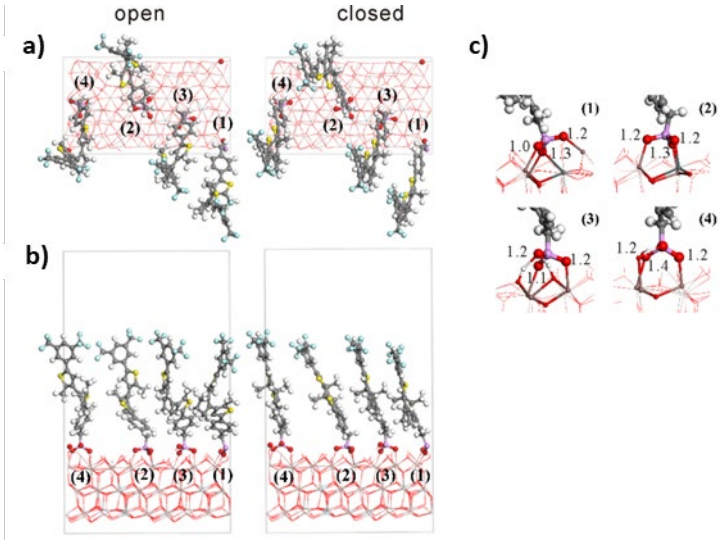

Figure 5.24. a) Top and b) lateral view of the unit cells for the open- (left) and closed- (right) PA-DAE forms. The numbers inside (1-4) denote the position of the absorption sites, i.e., 1-2 the tridentate and 3-4 the bidentate binding. c) Site lateral views of the optimized absorption geometries of the open PA-DAE molecules for the four absorption sites; values give the DFT calculated O 1s binding energy shift (in eV) with respect to the oxygen in bulk.

As shown in Fig 5.24a and b, different bonding characteristics are found at four sites: site 1 and 2 are attached in a tridentate binding with Sn and In atoms, while sites 3 and 4 are attached in bidentate binding with one O atom connected to surface hydroxyl groups. The CLS of O1s belonging to PA were calculated by the final state approximation.[169,170] Using the bulk oxygen binding energy (530.3 eV from XPS) as a reference, the calculated CLS of PA are shown in Figure 5.24c. Among the four adsorption sites, we find that the core level binding energies are not highly affected whether the O is connected to the hydroxyl groups, or the Sn/In atoms of ITO; all the CLS for bidentate and tridentate adsorptions vary from 1.0 to 1.4 eV, while the majority of the values is at 1.2 and 1.3 eV. These values are in excellent agreement with the XPS data (1.4 eV) as discussed above in Figure 5.22, pointing to that the adsorption of bidentate and tridentate coexist on the ITO surface, but

are not energetically resolved. Thus one peak at 531.7 eV is added in the fitting of O 1s, accounting for the coexistence of bidentate and tridentate bindings. In addition, no changes of CLS are observed in the DFT calculations when going from open to closed forms (not shown here), implying that photoswitching of the SAM does not impact the strength of PA bonding.

Orientation of the SAM

XAS was performed at different angles to measure the orientation of PA-DAE molecules in the SAM. As shown in Figure 5.25a, the spectra were collected from the C K-shell electrons excited to unoccupied molecular orbitals. The most intense transition located at 285.0 eV exhibits a strong angular dependence, and is assigned to the C 1s to π^* orbital transitions. Since the 1s initial state of carbon is spherically symmetric and bears no angular momentum. Therefore, the angular dependencies of absorption intensity will be directly dependent on the final state, that is the π^* orbital orientation. For the open form (PA-DAE-o), the molecular orbitals of the lowest unoccupied C=C excitations are localized on the upper part of the molecule (shown in Figure 5.25c), and perpendicular to molecular plane that is the upper part of PA-DAE. To quantify the average orientation of PA-DAE in the SAM, the intensity of π^* ($I_{\pi*}$) was collected at five different angles. By assuming that the sample under investigation is isotropic meaning that $\pi*/\sigma*$ ratio for this material does not vary with the X-ray incidence angle. $I_{\pi*}$ can be fitted with equation 5.9:

$$I_{\pi^*} = C[Pcos^2\theta cos^2\alpha + 0.5sin^2\theta sin^2\alpha + (1-P)0.5sin^2\alpha] \qquad (5.9)$$

where P is the polarization factor, which is 0.9 for the beam in Bessy, θ is the incidence angle of light, α is the molecular tilt angle as shown in Figure 5.25b. Thus the calculation yields an average tilt angle of 60° (as shown in the inset of Figure 5.25b) with respect to the surface for PA-DAE-o molecules. Since the molecular orientation in the monolayer is strongly dependent on the molecule-substrate and molecule-molecule interactions as well as on the molecular packing details, such calculated results are reasonable when compared to other fluorinated alkyl- and benzylphosphonic acids on ITO.[171,172]

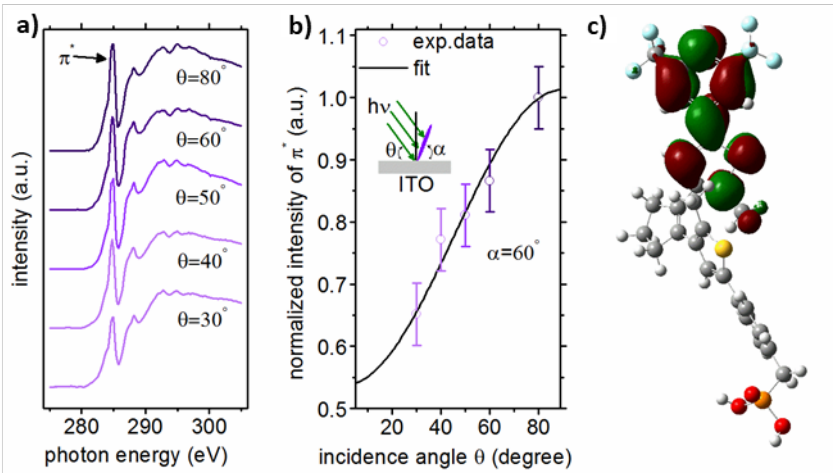

Figure 5.25. a) C K-edge X-ray absorption spectroscopy of the PA-DAE SAM modified ITO surface. b) Plots of the π^*-orbital intensities as a function of the photon incidence angle θ. The solid curve corresponds to the best fit of the intensity evolution for PA-DAE with the tilt angle of 60°. c) Molecular orbitals for the excited state corresponding to the first π-resonance of carbon atoms.

Electronic properties of the SAM

To investigate the valence electronic properties, UPS measurements were performed. Figure 5.26 shows the UPS spectra of the bare and PA-DAE modified ITO surfaces. The ϕ of the bare ITO surface is measured to be 4.6 eV. The modification with the PA-DAE SAM increases ϕ to 5.3 eV, as can be seen from the SECO. In the valence region (middle panel) the onset of the HOMO of PA-DAE-o is measured at 1.1 eV BE. Thus the ionization energy (SECO+HOMO) is 6.4 eV, in good agreement with the results on ZnO faces. The SAM was then *in situ* illuminated with UV light to induce a photoswitching from open to closed forms. After 60 s of light illumination, a new low binding energy spectral feature with an onset at 0.4 eV is observed (green line). This feature is assigned to the HOMO of the PA-DAE-c. Subsequent illumination of the SAM with green light for 120 s reversibly switches the PA-DAE to its open form, as evidenced by the disappearance of the PA-DAE-c HOMO and reappearing of the PA-DAE-o valence features. To evaluate the valence electronic features, the DOS of isolated PA-DAE with both open and closed forms is calculated with the PBE functional. They are in excellent agreement with the UPS data, confirming the occurrence of photoswitching between the isomeric forms. Note that, no obvious work function changes are measured in the

photoswitching process (see the SECO). Considering that a quantitatively repetitive photoswitching is unlikely taking place, the measured work function by UPS (detection area is in the range of mm^2) is likely to be a superposition of open and closed forms.

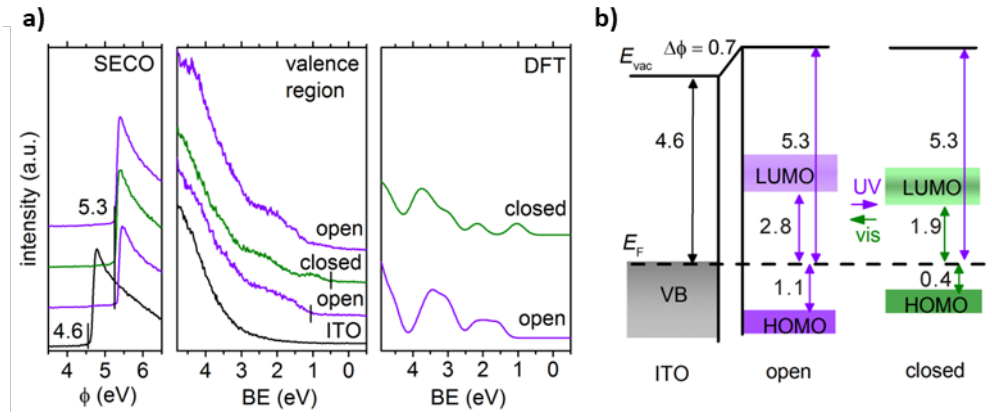

Figure 5.26. a) UPS spectra of the PA-DAE SAM on the ITO surface. Upon illumination cycles of UV and visible light, the work function of the SAM stays unchanged (left panel); the valence electronic features exhibit dramatic difference (middle panel) between the open and closed isomers. The DFT calculated DOS (right panel) for the two isomers are also plotted for comparison. b) Schematic energy level diagram of the ITO/PA-DAE interface. The energy positions of vacuum level (E_{vac}) and HOMO level are derived from UPS; while the LUMO level of PA-DAE is calculated using the transport gap of related DAE1 switches.

To better spatially resolve the work function change upon switching, the sample surface potential was mapped with the KPFM in smaller area (in the range of um^2). It was observed a reversible switching of the surface potential upon UV and green light illumination (Figure 5.27). Moreover, the surface potential of PA-DAE-c forms is ca. 60 ± 5 meV higher than that of PA-DAE-o forms. Similar switching induced potential change has been observed in other DAE SAMs by KPFM.[22] Such a potential change can be directly attributed to the change of PA-DAE dipole moment. Thus according to Helmholtz equation as discussed in equation 2.29, the packing density (n) of PA-DAE SAMs is revisited here:[173]

$$\Delta\phi = \frac{en\Delta\mu sin\alpha}{\varepsilon_r\varepsilon_0} \tag{5.10}$$

where $\Delta\phi$ is the potential change upon switching, which is 60 meV; e is the elementary charge; α is the molecular tilt angle as derived from angle dependent XAS in Figure 5.25; $\Delta\mu$ is the dipole difference between the open and closed forms. According to DFT

calculations, $\Delta\mu$ is 0.1 Debye for isolated molecules, however, it should be noted that a high coverage of molecules not only increases the density of dipoles, but also enhance the depolarization effect of surrounding dipoles.[79] This can be roughly accounted for by an relative dielectric constant ε_r, which is 1.4-1.5.[127] Thus the packing density n is estimated to be 1.5 ± 0.3 molecules nm^{-2}, in good agreement with the results estimated from XPS (as discussed earlier).

The interfacial ELA of the ITO/PA-DAE system derived from UPS was summarized in Figure 5.26b. For the unoccupied energy levels, the LUMO level of PA-DAE is obtained by referring to the transport gap of similar DAE1 derivatives as obtained by IPES. As shown in Figure 5.26b, the increase of work function upon SAM deposition is due to the presence of interface dipoles (will be discussed below). Similar to the previous observations on ZnO in the last section, the HOMO to E_F energy difference is reversibly switched upon illumination with light, i.e., 1.1 eV for the open and 0.4 eV for the closed forms, respectively. In the meanwhile, the LUMO to E_F difference shifts accordingly from 2.8 eV to 1.9 eV when going from open to closed forms. Consequently, this gives rise to HOMO and LUMO differences between open and closed forms of $\Delta E_{o\text{-}c,HOMO}$ = 0.7 eV and $\Delta E_{o\text{-}c,LUMO}$ = 0.9 eV, respectively. The PA-DAE frontier level shift going from isolated to packed monolayer was also calculated to further understand its relative energy level alignment between two forms. In isolated molecules, the HOMO (LUMO) of PA-DAE-c is located higher (lower) than that of PA-DAE-o due to an increase in the conjugation and a bandgap reduction in the closed form (Figure 5.28). The calculated $\Delta E_{o\text{-}c,HOMO}$ and $\Delta E_{o\text{-}c,LUMO}$ are both 0.7 eV. When increasing the coverage to monolayer,

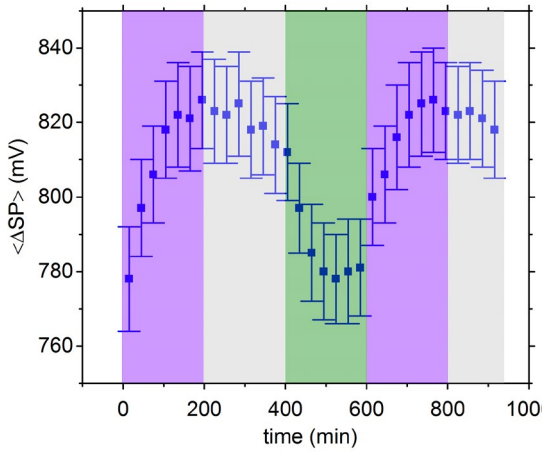

Figure 5.27. Surface potential (SP) mapping of the PA-DAE SAM on ITO. Upon UV illumination, the SP increases by ca. 60 meV, and upon illumination with visible light, the SP shifts back reversibly. The SP is measured with respect to the bare ITO surface.

all the frontier molecular orbital energies exhibit an upshift, since the intermolecular interactions are enhanced, and this shift saturates at a degree of coverage n=3. However, the relative energy level alignment is still well preserved, i.e., $\Delta E_{o\text{-}c,HOMO}$=0.5 eV and $\Delta E_{o\text{-}c,LUMO}$ =0.9 eV, which is in good agreement with the experimental alignment.

Theoretical understandings on the surface potential change

To further understand the surface potential modification at the ITO/PA-DAE interface, theoretical modeling at the DFT level was performed. Similar to the studies on ZnO, the isolated PA-DAE molecules are geometrically optimized in the beginning in Gaussian09 with the PBE functional, and they were subsequently grafted on the ITO surface (in both tridentate and bidentate modes) to form a monolayer. The description of ITO has been previously reported by H. Li et al,[68] which is formed by three (In-O)/(Sn-O) layers with a In/Sn ratio of 0.14; while the surface is passivated with hydroxyl groups. Following the methodology proposed by H. Li et al, four PA-DAE molecules (n=4) with both open and closed forms were attached on the ITO surface. The unit cell used has the dimensions a= 24.79Å and b=14.32Å, whereas a vacuum of 32 Å between slabs were set in the normal dimension, where the dipole correction was applied.[174] The resulting surface area is A = 88.75 Å^2 per molecule. This value is higher than the experimental data obtained by XPS, which is A= 50 ± 11.54 Å^2 per molecule. Despite this discrepancy, Li et al. showed that at the high coverage regime (n=4) the value of $\Delta\phi$ has already converged; and there is only a difference of 0.1 eV compared to the value obtained with the experimental coverage for the trifluorophenyl-PA SAMs.[68] Similar to the descriptions for PA-DAE on ZnO, the work function modification can be defined as the work

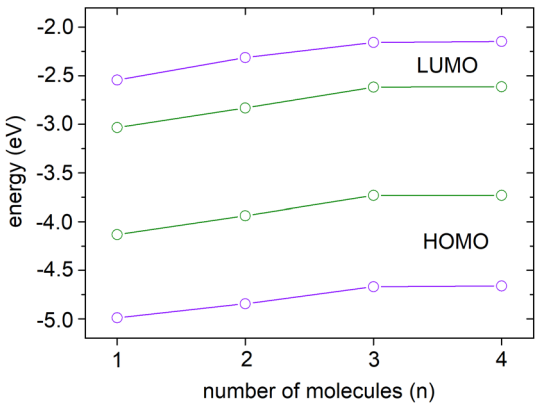

Figure 5.28. Frontier molecular orbitals (HOMO/LUMO) energies of the PA-DAE SAMs as a function of the coverage (n=1-4) for open- (purple) and closed- (green) forms. The vacuum level at the unabsorbed (left) side was set as reference.

function difference $\Delta\phi$ between the SAM ($\phi_{ITO\text{-}SAM}$) and the bare ITO (ϕ_0), thus it is decomposed into three contributions:

$$\Delta\phi = \phi_{ITO-SAM} - \phi_0 = BD + \Delta V_{SAM} + \Delta\phi_{ITO} \quad (5.11)$$

where BD is the formation of a bond dipole at the ITO/PA-DAE SAM interface due to charge transfer; ΔV_{SAM} is the intrinsic dipole of PA-DAE in the monolayer; $\Delta\phi_{ITO}$ is work function change due to the surface relaxation effect upon SAM grafting. For the calculation of BD, we refer to Poisson's equation, thus the potential difference $V(z)$ on both sides of the slab is a function of the plane averaged charge density difference $\Delta\rho$, which has been calculated following the so-called molecular scenario:[175,176]

$$\Delta\rho = \rho_{sys} - \rho_{ITO} - \rho_{SAM-H} + \rho_H \quad (5.12)$$

where ρ_{sys} is the plane averaged charge density of the full ITO/PA-DAE system; ρ_{ITO} is the charge density of the modified ITO surface; $\rho_{SAM\text{-}H}$ is the charge density of the PA-DAE layer including two added H per molecule corresponding to the original PA-DAE molecule; ρ_H is the charge density of the two isolated atoms per molecule with the same geometry as in the PA-DAE monolayer. Figure 5.29 shows the $\Delta\rho$ and its cumulated charge reorganization $\Delta Q(z) = \int \Delta\rho(z)dz$ upon SAM formation along the z axis. It is shown that for both open and closed forms, $\Delta\rho$ exhibits similar distributions and the amounts of transferred charges (ΔQ) from ITO to PA-DAE are virtually the same. A further Bader population analysis indicates that the amount of charge transfer is 1.36 |e| per PA-DAE molecule, such transferred charges are mostly localized in the PA anchoring group (-1.0 |e|), while the charges in the

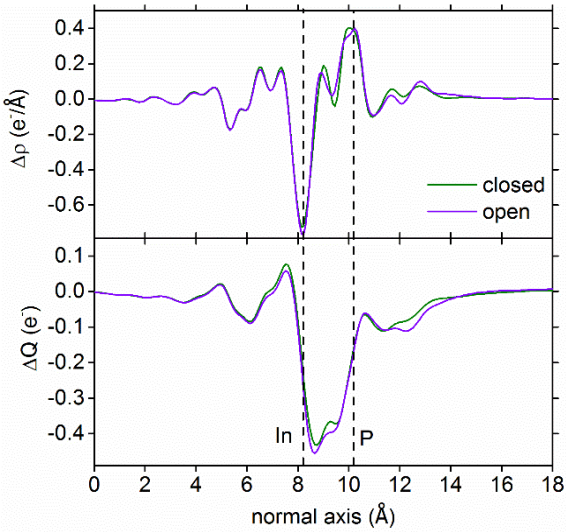

Figure 5.29. Plane averaged charge density difference (top) and its integral (bottom) along z-axis at the ITO/PA-DAE interface for open- (violet) and closed- (green) forms. The vertical dashed lines denote the averaged position of the top layer In and P atoms. The plottings show that charge transfer occurs from the ITO substrate to PA molecules.

DAE backbone are not highly modified (-0.36 |e|). To calculate ΔV_{SAM}, an isolated monolayer of PA-DAE molecules was constructed with the same geometry as that on the ITO surface and with hydrogen atom(s) added to make the system neutral; then the plane-averaged electrostatic potential across this organic layer was computed. For evaluating $\Delta\phi_{ITO}$, the equation $\Delta\phi_{ITO} = \phi_{ITO} - \phi_0$ was applied, where ϕ_{ITO} is the work function of the ITO surface after removing the SAMs; ϕ_0 is the work function of the initially unmodified ITO surface as mentioned earlier. The work function change and its three components are summarized in Table 5.2.

eV	*BD*	ΔV_{SAM}	$\Delta\phi_{ITO}$	$\Delta\phi$	$\phi_{ITO-SAM}$	ϕ_0
open	0.61	1.29	-0.42	1.48	4.68	3.20
closed	0.55	1.57	-0.41	1.71	4.92	3.20

Table 5.2. Decomposition of the work function modification upon adsorption of the PA-DAE molecules. All the values are given in the unit of eV.

It is noted that for both open and closed SAMs, the values of BD are compensated by that of $\Delta\phi_{ITO}$ ($BD + \Delta\phi_{ITO} \approx 0.2\ eV$), thus making the magnitude of $\Delta\phi$ primarily driven by the molecular dipole component $V_{\mu SAM}$. The DFT calculated $\Delta\phi$ for the closed form is ca. 200 meV higher than that of the open form, which is consistent with the KPFM results (60 meV). This $\Delta\phi$ difference between the open and closed forms is mainly ascribed to a higher value of the molecular contribution ($V_{\mu SAM}$) in the closed form. Although the relative changes in $\Delta\phi$ is well reproduced by the calculations, it has to be emphasized that the absolute value of the theoretical $\Delta\phi$ is twice as large as the experimental value (0.7 eV). It is suggested that this discrepancy is likely related to a Fermi level pinning effect of the molecular levels, which creates another interfacial dipole contribution. This process appears not to be well depicted by the DFT calculations and two reasons can be put forward for this: *i)* the relative energy level alignment of the isolated components (ITO versus PA-DAE molecules) is not adequately described; and/or *ii)* much larger unit cells are needed to describe a full charge transfer between the molecule and the electrode to properly describe the Fermi level pinning. Fully addressing this issue is, however, beyond the scope of the present work.

Conclusion

The photochromic PA-DAE SAM was employed to dynamically switch the surface electronic properties of the ITO electrode surface. The bare and modified ITO were comprehensively investigated by contact angle, AFM, XPS, XAS and UPS measurements, these characterizations provide a detailed picture of the coverage, chemical binding, and arrangement of PA-DAE SAMs. Both of our XPS and UPS results are further supported by DFT calculations to unambiguously unclose the *i*) binding modes of the PA; *ii*) surface potential modification which is primarily driven by the molecular dipole moment. Upon alternating illumination of UV and green light, the PA-DAE molecule switches between its open and closed isomers, which leads to reversible frontier level shifts (0.7 eV for HOMO, 0.9 eV for LUMO), and concomitantly a small work function change. Our findings provide a pathway to modify the electrode surface electronic properties upon external light illumination, and this strategy will be further employed in ITO-based photoswitchable devices.

5.4 Pyridyl-Dihydropyrene Switches on Zinc Oxide

The abovementioned photoswitches is based on the light-switching. However, for some of photoswitches, e.g., azobenzenes,[177] spiropyrans,[178] they are not only responsive to light but also sensitive to other stimuli, such as heat and PH values. To obtain knowledge on multiple stimuli-induced switching, negative T-type DHP molecules were synthesized as their ring-opening reaction is upon light illumination, while the back-switching reaction can be triggered by heat. Due to these switching properties, DHP switches show promising applications for photoswitchable and thermoswitchable devices.[179] Another aspect which makes DHP a promising component is that the DHP core can be modified with a wide range of chemical groups that allow either tuning its electronic and switching properties or being integrated in photoswitchable devices.[180]

Here, the pyridyl-DHP (Py-DHP) molecules (chemical structure in Figure 5.30a) were synthesized for switching the hybrid ZnO/Py-DHP interface. The pyridine linker is expected to function as an anchoring group to adsorb on the inorganic metal oxide

surfaces,[72] thus forming ordered molecular alignment and modifying the surface electronic properties. It is demonstrated that the use of Py-DHP can reversibly change the electronic properties of the polar ZnO surfaces, that is ZnO(0001) and ZnO(000-1). The ability to modify its surface electronic properties in a dynamic manner leads to a reversible control of interfacial charge injection/extraction properties, thus implementing a multifunctional nature in ZnO-based devices. The switching induced changes in the valence electronic properties and core level region are evidenced by UPS and XPS measurements. Theoretical calculations at the DFT are also performed to provide a deeper understanding of the experimental observations. Py-DHP is switched *in situ* either by exposure to green light (λ=565 nm) or proper heat treatment in order to switch between its open and closed form. It is found that a Fermi level pinning of the Py-DHP monolayer exists on both polar ZnO surfaces; the position of the Py-DHP HOMO level exhibits a reversible shift of 0.7 eV with respect to E_F when switching between the open and closed forms. Furthermore, a sizable work function increase is observed for the multilayer coverage upon green light illumination. In conjunction with the positions of the frontier energy levels in the multilayer higher ionization potentials in the multilayer regime than in the monolayer regime for both open and close Py-DHP were evidenced. This is attributed to a transition of the molecular orientation from preferentially standing up in the monolayer regime to a lying down or at least more inclined fashion in multilayer structures. These findings provide a solid basis for modulating the interface energy level alignment dynamically under external stimulations, which will further aid the development of multifunctional optoelectronic devices.

5.4.1 Electronic Properties of Py-DHP

First, the switching properties of a 10 nm thick Py-DHP on quartz was characterized by UV-vis spectroscopy. Figure 5.30b displays the spectral evolution of Py-DHP upon green light illumination (left Figure) to induce the ring-opening reaction and subsequent heat treatment (right Figure) for the reverse reaction. The spectrum of Py-DHP in its original closed form (Py-DHP-c) exhibits an absorption maximum in the green wavelength region (ca. 530 nm or 2.3 eV). Upon green light illumination, the absorption maximum of closed

Py-DHP attenuates gradually accompanied by an enhancement of the absorption in the UV region (ca. 300 nm or 4.1 eV). These changes occur as the effect of the aforementioned ring-opening reaction. After 30 minutes of illumination, no further changes in the spectra are observed. This indicates that the photoswitching of closed Py-DHP reaches a photostationary state. The film was then *in situ* heated at a temperature of 50 ºC (see also Figure 5.30b) to switch open Py-DHP (Py-DHP-o) back to its closed form. Within 30 min of heat treatment, the spectral appearance is restored to that observed initially for Py-DHP-c, evidencing a high switching efficiency of Py-DHP back to its closed form. To rationalize the experimental observations, TD-DFT calculations (dashed lines) were performed. The results show that the lowest absorption peak lies at 510 nm for Py-DHP-c (green dashed line), in agreement with the experimental data. For Py-DHP-o, the lowest absorption peak is predicted at 400 nm (red dashed line). Interestingly, in the experimental results, the absorption peak in green region does not disappear completely upon green light illumination to induce the ring-opening reaction. Such an incomplete photoswitching of the Py-DHP-c is primarily attributed to thermal back-switching of Py-DHP-o (even at room temperature),[181] The switching efficiency of closed to open Py-DHP is estimated to be ca. 80% by comparing the absorption intensity in the visible region after subtracting the Rayleigh scattering background.

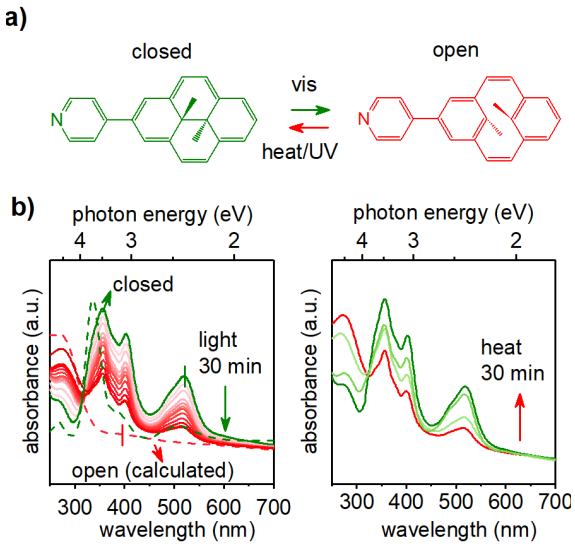

Figure 5.30. a) Chemical structure of Py-DHP switches. Switching between the two isomers is triggered via either light illumination or heat treatment. The ring-opening process of the Py-DHP film (10 nm) reaches a photostationary state after ca. 30 min illumination (λ=565 nm, I_{max} > 200 mW cm^{-2}) and can be reset by heat treatment (50 ºC), as displayed by UV-vis absorption spectra in b). Calculated absorption spectra of Py-DHP by TD-DFT are also plotted as a comparison (dashed line).

UPS and XPS measurements were performed in order to access the changes in the electronic properties of Py-DHP upon switching. Figure 5.31 displays the UPS spectra of Py-DHP on both ZnO polar faces upon switching back and forth (by green light illumination and heating) for both mono- and multilayer regimes (thicknesses of 10 and 100 Å).

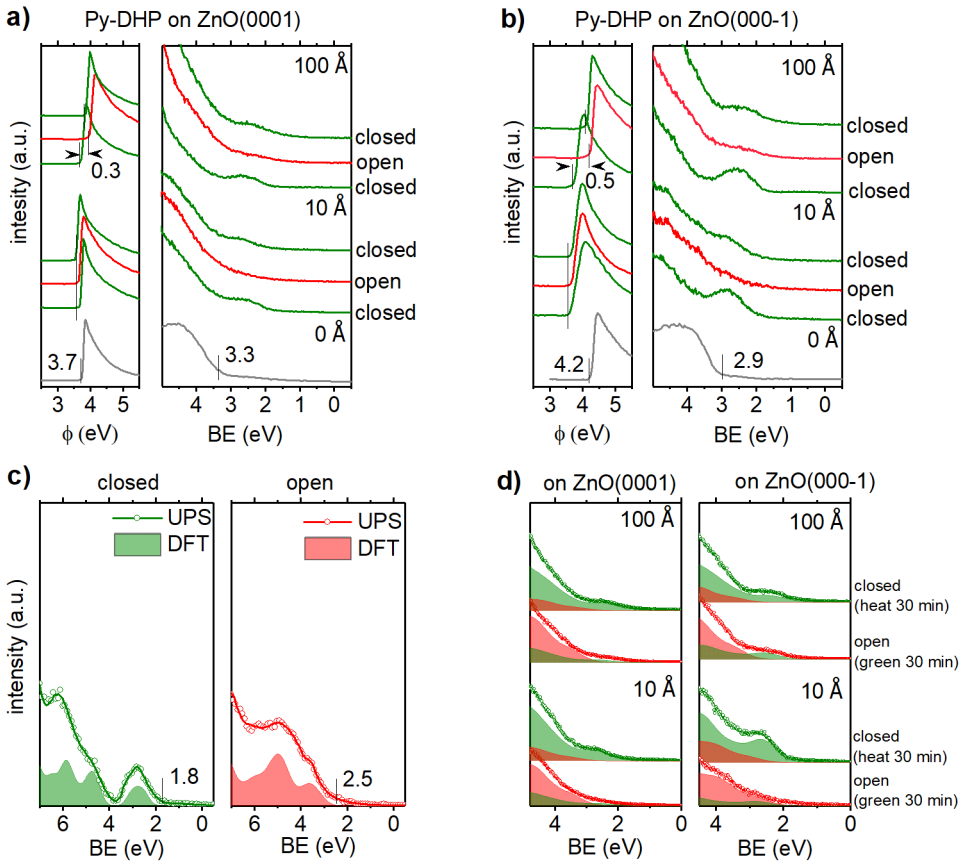

Figure 5.31. UPS spectra of 10 Å and 100 Å Py-DHP films evaporated on a) ZnO(0001) and b) ZnO(000-1) surfaces, respectively. For each film, in situ switching was realized through the illumination by green light, which switches the molecule from its closed to its open form (red line); and through heat treatment (50 °C temperature) for switching back to its closed form (green line). c) UPS spectra (substrate signal subtracted) and DFT calculated density of states (DOS) of the closed of open Py-DHP molecule. The DFT calculated spectra were shifted by 0.4 eV for aligning the experimental results. In the calculations, photoemission cross sections were not taken into account. d) Decomposition of the sample spectra into closed and open Py-DHP contributions.

For bare ZnO(0001) (top left inset in Figure 5.31a), the VBM and the work function ϕ are measured at 3.3 eV and 3.7 eV, respectively, This is in line with the reported values for clean ZnO(0001).[19] First, a 10 Å thick Py-DHP film (originally in its closed form) was

deposited on ZnO to form a monolayer coverage. No ϕ change is observed upon film deposition, and the onset of HOMO of Py-DHP-c arises at 1.8 eV BE.

The film was subsequently illuminated with green light for 30 min. As a result of the illumination, Py-DHP switches from its closed form to its open form, and accordantly its spectral features in the valence region change dramatically. Most prominently, the HOMO of Py-DHP-c located between ca. 2-3 eV BE disappears. Noteworthy, even though it was estimated the switching efficiency to be ca. 80%, the valence electronic features of the Py-DHP-o film is hardly discernible in the UPS. This is because the signal of Py-DHP-o is superposed by the signals arising from both the substrate and the remaining Py-DHP-c molecules. To better display the pure signal for the open form, Figure 5.31c shows UPS data for which the signal of ZnO as well as the one of the Py-DHP-c is subtracted. After the data correction, the valence features of Py-DHP-o are well observable with the HOMO onset at 2.5 eV BE. Therefore, the photo-induced ring-opening reaction shifts the frontier HOMO level by 0.7 eV farther away from the Fermi level, as also observed in other photoswitches, e.g., DAE molecules in the previous section. The film was then heated *in situ* to a temperature of 50 ºC for 30 min in order to trigger the reverse ring-closure reaction. Consequently, the reappearing of the Py-DHP-c HOMO with its onset at 1.8 eV binding energy is observed, confirming that Py-DHP molecules are indeed switched back to their closed form. To corroborate these findings of the different electronic structure of Py-DHP-o and Py-DHP-c molecules, theoretical calculations at the DFT level were performed using the PBE functional. As shown in Figure 5.31c, The UPS spectra of both open and closed Py-DHP films can be well reproduced by the calculated DOS projected onto the molecular region; this confirms that the switching of Py-DHP occurs under different stimuli. Moreover, the valence electronic features between the open and closed Py-DHP are totally different. With the corrected UPS spectra of open and closed forms, the experimental UPS spectra of the monolayer film after switching by green light can be quantitatively fitted with two contributions (see Figure 5.31d). Hereby we obtain a fraction of ca. 80% open Py-DHP and 20% closed Py-DHP. This ratio is consistent with the switching efficiency as observed in the UV-vis

measurements. Applying the same procedure to the spectra after the induced back-switching into the closed form by heat treatment, we obtain numbers of 95% closed Py-DHP and 5% open Py-DHP.

To study the switching properties of Py-DHP in bulk films, the film thickness was first increased to 50 Å and subsequently to 100 Å on both ZnO. It is found that the HOMO onset of Py-DHP-c stays fixed at 1.8 eV, where it was also for the monolayers. Upon inducing the switching process by green light illumination and subsequent heat treatment, it is also found that in the multilayer regime Py-DHP exhibits a reversible switching behaviour. Equivalent to the results for the monolayer, the ring-opening reaction is accompanied by a disappearance of the Py-DHP-c HOMO feature at 1.8 eV BE and a corresponding reappearance of the Py-DHP-o at 2.5 eV BE (deduced from the different spectra). Subsequent heat treat expectedly restores the HOMO feature of Py-DHP-c in the valence region (Figure 5.31a). However, different to the monolayer regime where the work function stayed constant upon switching, here in the multilayer regime the switching (ring-opening reaction) also leads a work function increase by 0.2 eV and 0.3 eV for 50 Å and 100 Å thick films, respectively. Moreover, this switching induced change of the work function is not fully reversible.

To obtain more general insight into the ZnO/Py-DHP interface electronic properties, Py-DHP was also deposited on ZnO(000-1) (see Figure 5.31b). Due to different surface termination, the bare surface exhibits a VBM and ϕ of 2.9 eV and 4.2 eV, respectively, deposition of a 10 Å thick Py-DHP-c film equivalent to ca. a monolayer coverage results in a decrease of the work function by 0.6 eV to a final ϕ of 3.6 eV. Noteworthy for Py-DHP-c monolayer on ZnO(0001), no change of ϕ was observed. Yet, the final work functions exhibited by the Py-DHP-c monolayer coverages on both of the two surfaces are virtually identical. Accordingly one observes the HOMO onset of Py-DHP-c on ZnO(000-1) also at 1.8 eV BE. Equivalent to the ZnO(0001) surface a reversible switching of the Py-DHP film on ZnO(000-1) can also be induced by green light illumination and heat treatment, as shown in Figure 5.31b. According to the decomposition of the spectra (Figure 5.31d), the HOMO onset for Py-DHP-o is

determined at 2.5 eV. Also here the ϕ of Py-DHP monolayer films stays constant during switching. Differently also on ZnO(000-1), one observes an increase of the multilayer work function upon switching the film. Quantitatively, the switching-induced work function change is similar, yet a little larger than the observations made on ZnO(0001). For the 50 Å and 100 Å thick films, we observe ϕ increases by 0.3 eV and 0.5 eV, respectively. On ZnO(0001) the corresponding values were 0.2 and 0.3 eV.

The energy level alignment discussed in the previous paragraphs for Py-DHP on both ZnO faces for mono- and multilayer coverages as well as upon switching is summarized in Figure 5.32.

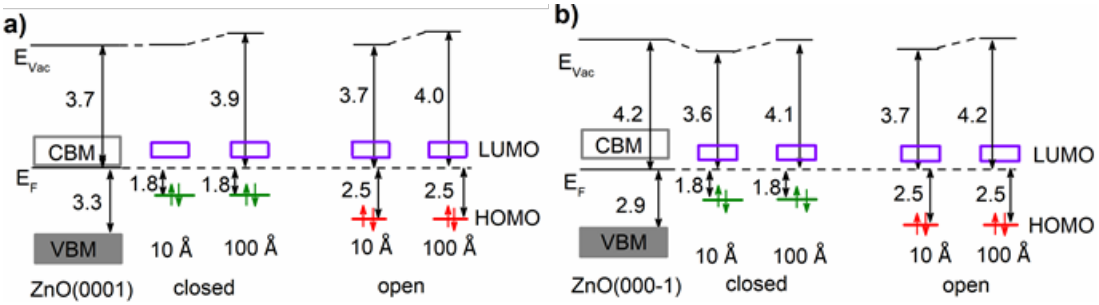

Figure 5.32. Energy level diagrams of a) Py-DHP on ZnO(0001) and b) Py-DHP on ZnO(000-1). All values are in the unit of eV. Energetic positions of vacuum level (E_{Vac}), VBM, HOMO with respect to the Fermi level (E_F) were derived from UPS measurements. While the positions of CBM and LUMO were derived by considering the material's transport gaps. Note that for Py-DHP the transport gap was calculated by summing up its optical gap and exciton binding energies (for details, see the main text).

Clearly one cannot recognize a single energy level alignment scheme, as e.g., the Schottky-Mott limit, explaining all the data at hand. As a natural starting point to elucidate this complex situation we note that Py-DHP has an intrinsic dipole moment roughly along the long molecular axis. This can easily be rationalized from the fact that the pyridine group is polar and that the first Py-DHP monolayer with this anchoring group will preferentially align upright on the surfaces.[70,72] By that one can easily and qualitatively explain the work function reduction by 0.6 eV on ZnO(000-1). However, this then raises the question why on both surfaces identical final work functions are observed or in other words, and why ϕ stays constant on ZnO(0001). Undisputedly, there is a second process raising back the potential (effectively keeping it constant) must also be present, e.g.,

Fermi level pinning. However, adding the optical gap as deduced from UV-vis (2.1 eV for the open and 2.9 eV for the closed) to the obtained HOMO position as well as an appropriate exciton binding energy of 0.3-0.4 eV,[45] it is estimated that the LUMO position is ca. 0.5 eV above E_F for both forms. While pinning levels of 0.5 eV are not unprecedented in the literature,[84] this assignment is not univocal. Therefore, this is required to perform theoretical calculations at the DFT level to further understand the electronic properties at the ZnO/Py-DHP interface.

5.4.2 Theoretical Understandings of the Interface

To obtain the information of Py-DHP monolayer packing densities, XPS core level spectra were carefully analysed. As shown in Figure 5.33, Zn 3p signals are from ZnO, while C 1s and O 1s signals are from Py-DHP. All the spectra were fitted with a Shirley background and Voigt profiles.

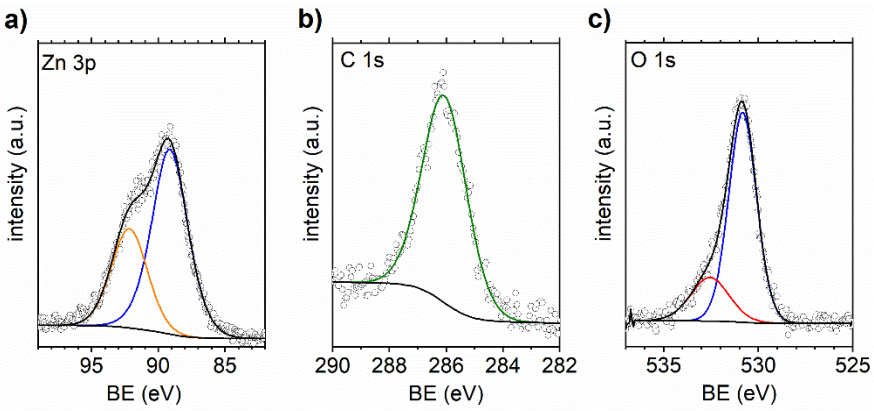

Figure 5.33. XPS spectra of a) Zn 3p, b) C 1s, c) O 1s for 10 Å Py-DHP (closed) film on the ZnO(0001) surface. The spectra were fitted with Pseudo-Voigt profiles by adding a Shirley background, where the electron inelastic scattering cross-section is considered as a constant.

The measured peak intensities of the three elements satisfy the following equation, where the exponential decay of out-coming electrons is taken into consideration:

$$\frac{I_C}{I_{Zn3p}} = \frac{N_C S_{C1s}}{N_{Zn3p} S_{Zn3p}} \frac{1-\exp(-d_{mol}/\lambda_C cos\theta)}{\exp(-d_{mol}/\lambda_{Zn,mol} cos\theta)}$$
$$\frac{I_C}{I_{O1s}} = \frac{N_C S_{C1s}}{N_{O1s} S_{O1s}} \frac{1-\exp(-d_{mol}/\lambda_C cos\theta)}{\exp(-d_{mol}/\lambda_{O,mol} cos\theta)} \quad (5.13)$$

where S_{C1s}, S_{O1s} and S_{Zn3p} are the relative sensitivity factors (normalized to C 1s) of the C 1s, O 1s and Zn 3p. Their values are 1, 2.77 and 2.95, respectively, λ_O is the electron IMFP of O 1s in the Py-DHP monolayer (thickness is the length of the molecular

backbone, which is ca. 1 nm), $\lambda_{Zn,SAM}$ is the electron IMFP of Zn 3p in the Py-DHP monolayer. Thus the surface coverage of the Py-DHP molecules is given by $N_C \times d_{mol}$, which is 2.6 $\pm$ 0.8 molecules nm^{-2} (30% of error for the estimation) for 10 Å Py-DHP on ZnO(0001).

Similar surface coverages are also calculated on the ZnO(000-1) surface. Based on the calculated Py-DHP packing densities, the unit cells of polar ZnO faces (for standing Py-DHP) were made of 12 layers with their a and b lattice vectors of 6.5 Å and 5.6 Å, respectively. This yields theoretical surface density of ca. 2.8 molecules nm^{-2}, comparable to experimental data. For lying Py-DHP larger unit cells, in the absence of experimental coverage, unit cell with a=13 Å, b=11.2 Å, respectively, was used to fit the molecular volume when it is lying down. Thus the surface density of lying Py-DHP is 0.7 molecules nm^{-2} (see Figure 5.34).

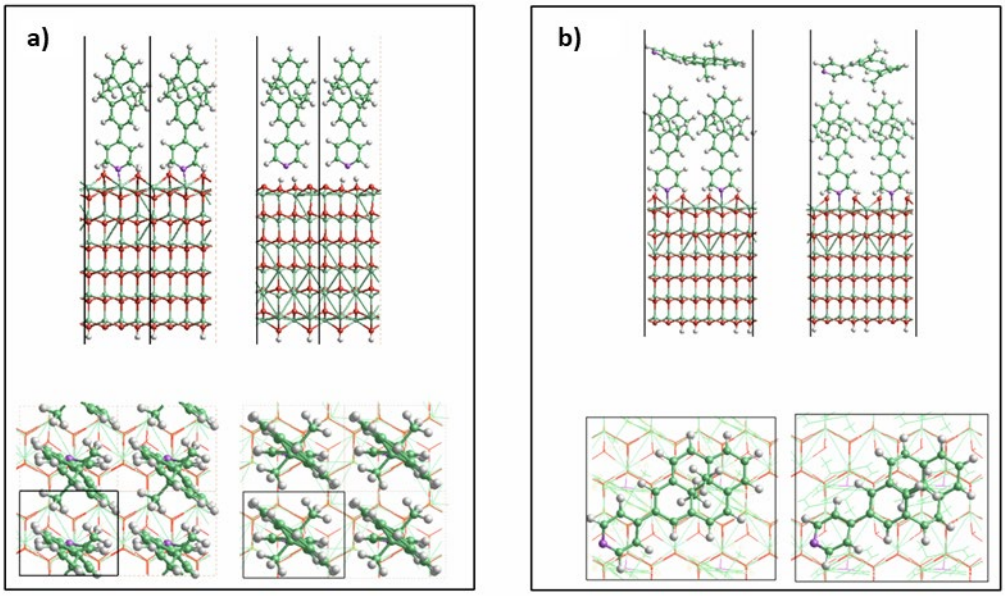

Figure 5.34. a) Lateral (upper panel) and top (lower panel) view of unit cells for Py-DHP standing on ZnO(0001) and ZnO(000-1) slabs. b) Lateral (upper panel) and top (lower) of unit cells for Py-DHP with lying down structures on top of the standing monolayer.

First, the dipole moments of isolated Py-DHP-c and Py-DHP-o molecules in the gas phase were computed to be 3.4 and 3.5 Debye, respectively (direction from Pyridine negative pole to DHP positive pole) along the molecular backbone. These values are definitely large enough to allow work function reductions of the experimentally observed

magnitude. To further verify such reductions at the interface between Py-DHP and ZnO, Py-DHP with its open and closed forms was subsequently onto both polar ZnO surfaces. The adsorption energies of the Py-DHP on ZnO are computed in order to evaluate the stability of Py-DHP on ZnO. As displayed in Table 5.3, they are calculated from the difference between the energy of the SAM and the sum of the energies of the free isolated molecule and free bare ZnO. Py-DHP on ZnO(000-1) is more stable by 0.5 eV per molecule than on ZnO(0001). Similar to the behaviours of other pyridine groups on polar ZnO,[164] Py-DHP is stabilized on ZnO(000-1) by a hydrogen bond between the pyridine and adjacent hydrogen atoms. On the contrary, the interactions between the pyridine and surface Zn atoms are reduced due to the presence of hydroxyl groups. Nevertheless, on both faces Py-DHP assumes a mostly upright conformation with the pyridine group facing the substrate.

On ZnO(0001)	E_{ads} (eV)	Bader charge (e)
closed	-0.55	0.02
open	-0.57	0.02
On ZnO(000-1)		
closed	-1.09	-0.04
open	-1.09	-0.04

Table 5.3. Calculated adsorption energy and interfacial Bader charge transfer between the ZnO slab and the Py-DHP molecule.

The projected density of states (PDOS) for Py-DHP on ZnO was first plotted in Figure 5.35. The energy level is referenced to the top of the ZnO conduction band. Interestingly, the PDOS of the LUMO levels for both open and closed forms on both surfaces overlaps with the position of the Fermi level. This is an indication of Fermi level pinning of Py-DHP on ZnO, which limits or in part cancels the downward ϕ shift due to the molecular dipole. Similar pinning effect caused by pyridine groups has been previously observed in pyrideneoligophenylene SAMs absorbed on Au(111).[182]

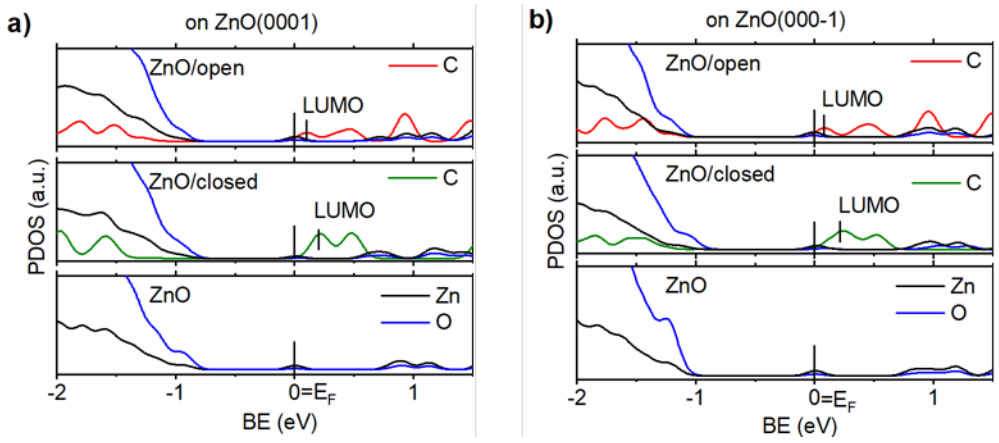

Figure 5.35. Projected density of states for Py-DHP monolayer on a) ZnO(0001) and b) ZnO(000-1), respectively. The E_F is referenced to the top of ZnO conduction band.

To further investigate the origin of such a pinning effect, it is necessary to understand the modification of surface potentials, e.g., contribution of molecular dipole moments, interface charge rearrangement. Thus a detailed decomposition of the work function modification is presented below.

As described in previous sections, the modification of the work function ($\Delta\phi$) can be decomposed into the following partitions.

$$\Delta\phi = BD + \Delta V_{Py-DHP} + \Delta\phi_{ZnO} \tag{5.14}$$

where BD is the bond dipole at the ZnO/Py-DHP interface due to charge transfer; $\Delta V_{Py\text{-}DHP}$ is the intrinsic dipole of the Py-DHP monolayer and $\Delta\phi_{ZnO}$ is the induced work function change in the ZnO slab itself due to the deformations caused by Py-DHP grafting. The BD in conjunction with the charge density difference ($\Delta\rho$) of the system is plotted in Figure 5.36, in which $\Delta\rho$ is expressed as:

$$\Delta\rho = \rho_{sys} - \rho_{Py-DHP} - \rho_{ZnO} \tag{5.15}$$

where ρ_{sys} represents the charge density of the full ZnO/Py-DHP interface in its final geometry, ρ_{ZnO} that of the ZnO surface in its final geometry; $\rho_{Py\text{-}DHP}$ the charge density of Py-DHP monolayer. It is shown in Figure 5.36 that $\Delta\rho$ exhibits similar distributions for both closed and open forms. The amount of charge transfer at the interface is relatively low due to the weak interactions between the pyridine anchor group and the top atoms of ZnO.

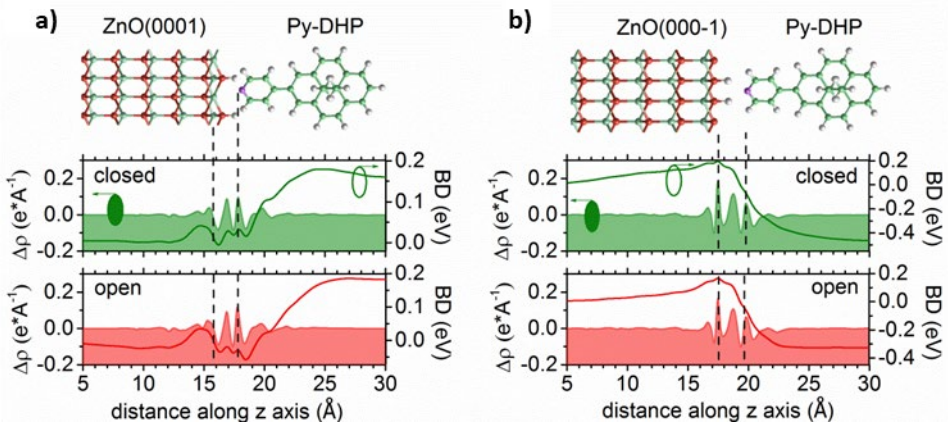

Figure 5.36. Plane averaged charge density difference (Δρ) and corresponding bond dipole (BD) potential for Py-DHP on a) ZnO(0001) and b) ZnO(000-1), respectively. The positions of the topmost Zn or O layer in ZnO and the N layer in Py-DHP are indicated by the vertical dashed lines.

A Bader charge population analysis (Table 5.3) reveals that 0.02 |e| are transferred from Py-DHP to ZnO(0001), whereas on ZnO(000-1), the direction of charge transfer is inverted and the size equals 0.04 |e|. Consequently, also the direction of the bond dipole is inverted. However, the overall size of the charge transfer is small and thus also the values of the BD components (Figure 5.36).

For calculating $\Delta V_{Py\text{-}DHP}$, an isolated monolayer of Py-DHP molecules is built with the same geometry as that on the ZnO. Then the plane-averaged electrostatic potential across this organic layer can be plotted. In the case of $\Delta\phi_{ZnO}$, one can rely on the equation $\Delta\phi_{ZnO} = \phi_{ZnO} - \phi_0$, where ϕ_{ZnO} is the work function of the ZnO surface after removing Py-DHP; ϕ_0 is the work function of the originally unmodified ZnO surface. $\Delta\phi$ and its three components are summarized in Table 5.4.

	$\Delta V_{Py\text{-}DHP}$	BD	$\Delta\phi_{ZnO}$	$\Delta\phi$
on ZnO(0001)				
closed	-1.6	0.2	0.2	-1.2
open	-1.6	0.2	0.2	-1.2
on ZnO(000-1)				
closed	-1.5	-0.4	0.3	-1.6
open	-1.5	-0.3	0.2	-1.6

Table 5.4. Decomposition of the work function shift ($\Delta\phi$) upon adsorption of the Py-DHP monolayer. All values are in the unit of eV.

On both ZnO, not only the BD contribution is small but also $\Delta\phi_{ZnO}$; almost all of the negative work function shift actually stem from the molecular contribution ($\Delta V_{Py\text{-}DHP}$ in equation 5.14) with only minor differences between the open and the closed isomer. This confirms the experimental findings that switching of the Py-DHP monolayer does not result in significant work function changes. However, there exists a sizeable difference between the calculated and measured $\Delta\phi$, i.e., the calculations provide values of -1.2 eV and -1.6 eV for ZnO(0001) and ZnO (000-1), respectively. Whereas experiments yield 0 eV and -0.6 eV for Py-DHP monolayer on ZnO(0001) and ZnO(000-1), respectively. Nevertheless, the larger reduction of the work function in ZnO(000-1) is reproduced by the calculations, thus indicating that the simulations correctly grasp the relative variations in the plane-averaged dipole moment at the interface. On the one hand, the discrepancy might originate from the fact that the partial charge transfer is not quantitatively described due to the underestimation of the ZnO bandgap in the calculations but it is unlikely that this effect could explain a difference of ca. 1 eV between theory and experiment in view of the weak interfacial interactions. On the other hand, the discrepancy might originate from a wrong description of the actual spatial distribution of the charge transferred at the interface. Indeed, by considering small unit cells, DFT calculation is bound to create an interface dipole by transferring a partial charge between the two components. Thus one cannot account for a situation where a full charge transfer implies a single molecule whereas the neighboring molecules remain neutral, as investigated hereafter.

5.4.3 Electrostatic Modelling of the Surface Potential

The pinning from an experimental point of view can be rationalized as: If in a thought experiment applying the calculated size of the molecular dipole (1.5-1.6 eV) to the experimental values (see Table 5.4), in particular on ZnO(0001) the Py-DHP (for both open and closed) LUMO would come to lie far below the E_F. Electronic equilibrium will be re-established by charge transfer into Py-DHP to raise back the LUMO above E_F by the concomitantly formed interface dipoles ΔV_{CT}. The fact that the final ϕ of the Py-DHP monolayer systems are the same (which is 3.7 eV) even though the initial ϕ of ZnO are not (i.e., 3.7 eV VS 4.2 eV) further evidence that the electronic level alignment is dominated by the position of the Py-DHP LUMO. While the qualitative description of the competing interplay of molecular dipole and pinning by theory and experiment agrees well, but the DFT calculations do not well reproduce the energy gaps and thereby also the pinning work function.

Noteworthy, the charge transfer upon pinning probably does not depolarize the molecular dipole, since the LUMO is mostly located on the molecular backbone (see Figure 5.38), whereas the molecular dipole is mostly formed by the polar bonds in the anchoring group. Accordingly, it is speculated that the systems actually exhibit a significant potential cancellation between the molecular dipole $\Delta V_{Py\text{-}DHP}$ and subsequent raise ΔV_{CT} in spatially disjunct regions of the Py-DHP monolayer. This is illustrated in Figure 5.37. Furthermore, by this a simple electrostatic model was introduced to describe the pinning situation,[53] which allows one to quantify the position of Py-DHP frontier levels after the re-establishment of electronic equilibrium.

For this a (integer) charge transfer is considered by building a regular mesh of dipoles consisting of a positive point charge right at the ZnO surface facing its negative counter charge in the molecule (see Figure 5.37c).[183] For the latter location, the whole range of the Py-DHP backbone is chosen, where the LUMO orbital is mainly located.

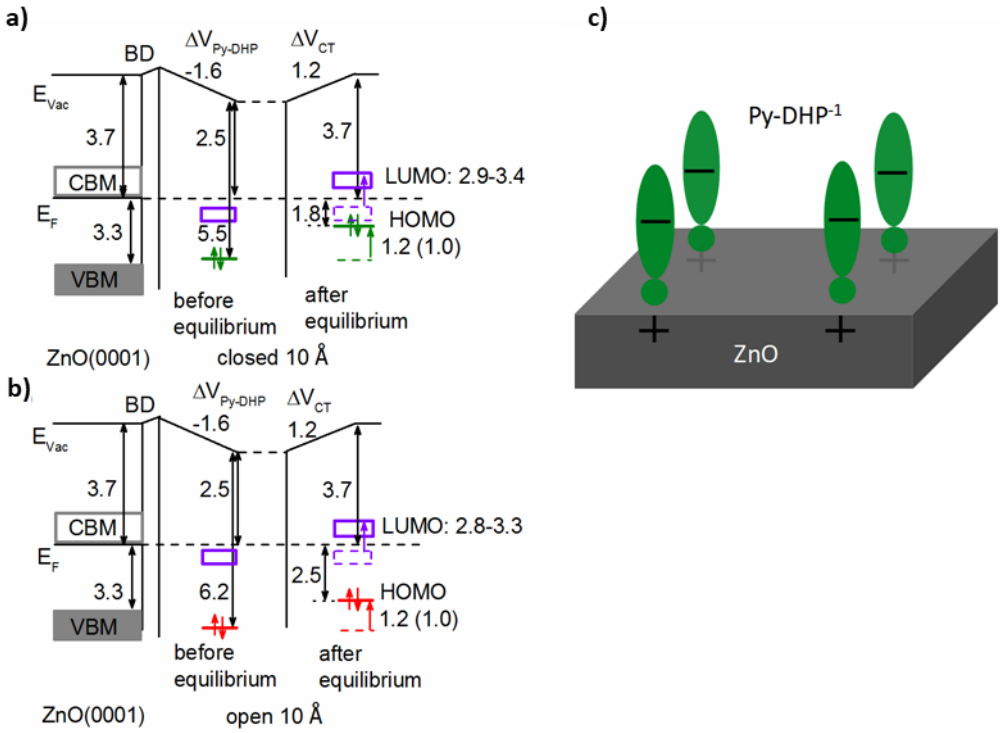

Figure 5.37. Schematic description of Fermi level pinning of a) closed and b) open Py-DHP/ZnO(0001) interfaces. Before the equilibrium, the frontier levels of Py-DHP are located below the Fermi level due to the potential drop created the intramolecular dipoles. After charge transfer, HOMO levels for Py-DHP are measured at 1.8 eV for the closed and 2.5 eV for the open form below the Fermi level. This corresponds to a 1.2 eV level shift for Py-DHP^{-1} after the equilibrium as shown in the Figure. The mapping of the potential in the uncharged Py-DHP region shows a 1.0 eV (shown in the parentheses) potential increase, which agrees well with the measured HOMO onset. c) Distribution of the electric field created by the Py-DHP^{-1} mesh at the surface.

The electrostatic potential on the surface of the substrate is considered as the sum of the potentials created by the negative point charges in Py-DHP and the positive point charges in ZnO. Considering different dielectric constants (take ε_r=8 for ZnO crystal[184] and ε_r=4 for Py-DHP monolayer[185]) for ZnO and Py-DHP, the electrostatic potential is expressed as:

$$\Delta V_{CT1} = \frac{q^-}{4\pi\varepsilon_1\varepsilon_0}\sum\left(\frac{1}{r_i} + \frac{\varepsilon_1-\varepsilon_2}{\varepsilon_1+\varepsilon_2}\frac{1}{r_i'}\right) - \frac{q^+}{4\pi\varepsilon_1\varepsilon_0}\sum\frac{2\varepsilon_1}{\varepsilon_1+\varepsilon_2}\frac{1}{R_i}, \quad z \geq 0 \tag{5.16}$$

$$\Delta V_{CT2} = -\frac{q^+}{4\pi\varepsilon_2\varepsilon_0}\sum\left(\frac{1}{R_i} - \frac{\varepsilon_1-\varepsilon_2}{\varepsilon_1+\varepsilon_2}\frac{1}{R_i'}\right) + \frac{q^-}{4\pi\varepsilon_2\varepsilon_0}\sum\frac{2\varepsilon_2}{\varepsilon_1+\varepsilon_2}\frac{1}{r_i}, \quad z \leq 0 \tag{5.17}$$

where ε_1 and ε_2 correspond to different dielectric constants for Py-DHP monolayer and ZnO. r' and R' are the position of the image charges of q^- and q^+. .ΔV_{CT1} is the potential above the ZnO surface and ΔV_{CT2} is the potential below the ZnO surface. Since the LUMO is primarily delocalized in the DHP backbone part, possible distributions of the negative charges with three different scenarios are considered, Thus by applying Helmholtz equation $\Delta\phi - -qn\mu_{\perp}/\varepsilon_r\varepsilon_0$, one can the fraction of Py-DHP^{-1}; the Py-DHP^{-1} fraction is primarily influenced by the so-called dipole-dipole repulsions, as discussed in section 2.3.1. Then, to cancel the calculated molecular dipole fully on ZnO(0001) and only in part on ZnO(000-1), fractions of charged Py-DHP are required to be below 10% on both surface. Thus the actual charge transfer in experiment can be hardly detected.

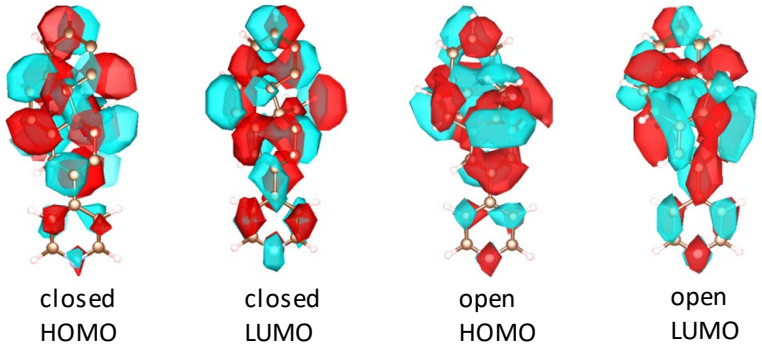

Figure 5.38. Frontier molecular orbital shapes of Py-DHP with its open and closed forms. The isovalue used is ±0.04 a.u. Note that the distribution of frontier orbitals such as LUMO is mainly localized on the DHP backbones.

Moreover, this non-vanishing charge transfer yields a significant energy inhomogeneity right on top and in the Py-DHP monolayer. Contour plots [see Figure 5.39 for Py-DHP on ZnO(0001)] in close vicinity at the top of the monolayer (z = 1.4 nm) map the potential distribution and evidence an energy inhomogeneity between the charged and uncharged regions of ca. 0.2 eV-0.3 eV. Importantly, this energetic disorder helps rationalizing how the experimentally estimated LUMO position (0.5 eV) is allowed to be rather far away from E_F (see Figure 5.38), while still causing an E_F pinning.

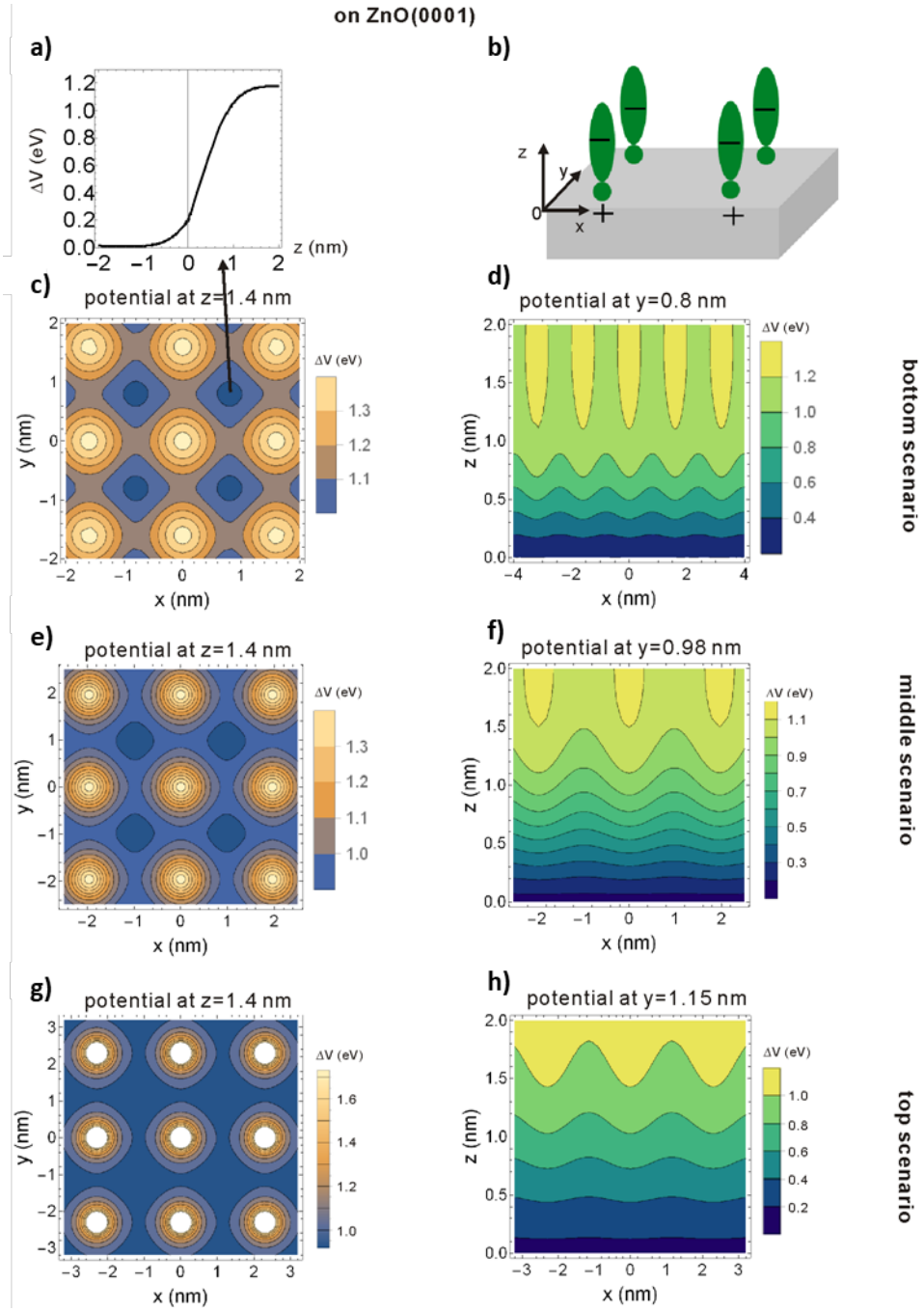

Figure 5.39. Map of the potential increase for Py-DHP monolayer on ZnO(0001) with different scenarios (from c-h). The coordinate of the system is shown in Figure b). The mapping shows that in the uncharged Py-DHP region, there is still substantial potential increase of ~1.0-1.1 eV on the top of the molecule (z=1.4 nm). For all calculations, zero potential is set at the bulk of ZnO (see Figure a).

Note that this energy inhomogeneity even exists if in sum (molecular dipole and pinning) the work function does not change at all.

Having now fully discussed the ELA of the monolayer and the switching properties, we will now revisit the multilayer regime. For this, it is necessary to recall that the HOMO positions of the open and closed isomers are identical to the monolayer. Yet, the work functions observed for multilayer Py-DHP on both ZnO faces are hundreds of meV larger as compared with the monolayer regime. This applies to both the open and closed isomers in the multilayer (which is summarized in Figure 5.32), which then directly translates into larger ionization energies as well. This implies a change of the molecular orientation going from mono to multilayer coverages,[186–188] probably because the second layer on the pyridine group cannot anchor anymore to the substrate.

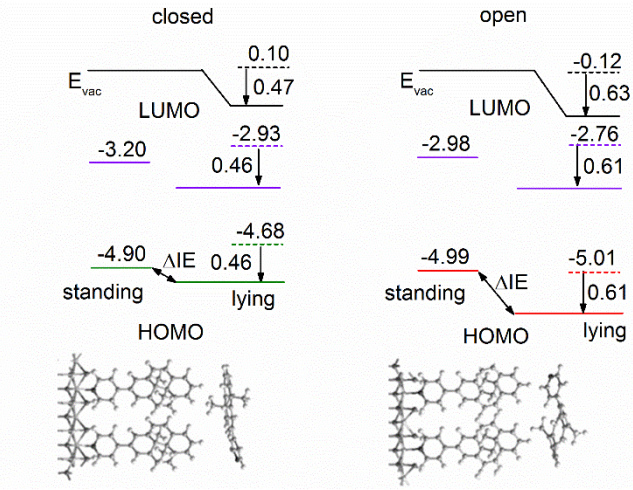

Figure 5.40. Energy level diagram of the multilayered Py-DHP molecules (standing and lying from left to right) adsorbed on ZnO(0001) surface for closed- (green) and open (red) forms. A schematic representation of the unit cell is represented at the bottom. In the case of the lying layer, the dashed and continuous lines represent isolated and interacting level energies, respectively. The arrows represent the shift in the energies when going from isolated to the ZnO/standing Py-DHP surface, thus resulting in an increase of the IP in the lying molecules compared to the standing molecules.

In the present case it is invoked a lying down or at least on average less upright conformation of Py-DHP in multilayers. In order to corroborate the explanation of orientational changes in multilayered systems, we also facilitate electronic structure calculations of systems comprising a second Py-DHP layer with a lying down orientation on top of the standing Py-DHP monolayer on ZnO.

First, the frontier levels of the isolated lying-down Py-DHP monolayer (shown in dashed lines) were calculated, then this monolayer was placed on the ZnO/standing Py-DHP surface. The calculations evidence a downward shift of these frontier levels in the lying second layer as compared with their isolated levels (0.46 and 0.61 eV for closed-and open forms, respectively). This is illustrated in Figure 5.40, in which the energy levels are referenced to a common vacuum level.[176] From this one can directly read that the IP of the lying layer is higher than the IP of the standing molecules (0.24 and 0.63 for closed- and open forms). To exclude any effects on the IP from the lying second layer unexpectedly being charged we also here perform a Bader charge analysis confirming that only negligibly charge transfer occurs into or from the multilayer (0.07|e| and 0.02|e| for closed- and open forms). Moreover, the energy alignment of the lying molecules is maintained when increasing the number of lying molecules. The calculated differences in the IP of open and closed Py-DHP between the standing monolayer and the lying second layer are in good consistency with the experimentally observed values, which corroborates that different orientations are assumed within the first and subsequent layers.

Conclusion

In conclusion, Py-DHP switches are employed to modulate the electronic properties on polar ZnO surfaces, i.e., ZnO(0001) and ZnO(000-1). With a comprehensive characterization of the sample by UPS and XPS, supported by DFT calculations, it is shown that the energy level alignment at the hybrid ZnO/Py-DHP interface can be reversibly modulated in a dynamic manner by external stimuli. Upon green light illumination, Py-DHP molecules switch from closed to open forms, resulting in a substantial shift of the HOMO level by 0.7 eV (towards higher binding energy) on both polar faces, corresponding changes in the energy level offset between the VBM of the ZnO and the HOMO of Py-DHP are determined. Meanwhile, in multilayer coverages we observe a 0.3 eV and 0.5 eV work function increase upon photoswitching on ZnO(0001) and ZnO(000-1), respectively, leading to different ionization potentials of Py-DHP compared to in monolayer. This is attributed to the molecular orientation transition from

a preferential standing up to lying down structure. These findings provide a pathway for the manipulation of interfacial electronic properties with photoswitches in a dynamical manner and will further be used to the development of multifunctional (opto-) electronic devices.

6. Summary and Outlook

6.1 Summary

The goal of the present work was to understand the electronic properties of photoswitches. In particular, focuses were on the dynamic photoswitching of energy levels at photochromic heterojunctions. This will provide a solid basis for developing multifunctional, photoswitchable devices. To achieve this goal, a range of complementary characterization techniques was used in this work. The optical properties of photoswitches were revealed by UV-vis absorption spectroscopy. The surface topography and wettability of photoswitch SAMs were investigated by AFM and contact angle, respectively, while information about the (average) orientation of molecules in the monolayer was acquired from angle-dependent XAS. The chemical/physical interactions at the interface were monitored by XPS, further information about the film thickness and molecular packing density on the surface was also derived from the quantification of XPS. The work function change and valence occupied levels upon film formation were measured by UPS, whereas the unoccupied levels were obtained from IPES. Experimental findings were further supported by DFT calculations: the electronic properties of single molecules in gas phase were computed in Gaussian09 software. For SAMs chemisorbed on semiconductors, calculations were performed with the SIESTA code.

First, in section 5.1 the electronic properties of DAE1 films were detailed revealed both experimentally and theoretically. It was demonstrated from UV-vis absorption and DFT calculations that the DAE1 optical gaps were different between its open and closed forms. Further DFT calculations on the dipole moments point to a 1.2 D dipole difference between the two forms. The measured transport gaps for open and closed DAE1 were 3.8 eV and 2.3 eV, respectively, which were larger than their optical gaps due to the

contribution of exciton binding energies. Upon switching from open to closed forms, the changes in the ionization energy of DAE1 exhibit a reduction by 0.8 eV. With all of these findings, it was concluded that the electronic properties of DAE1, i.e., energy gaps, dipoles, ionization energies, can be dynamically switched between the two isomers. Then the switching properties of DAE1 were applied to interfaces in the form of thin films to manifest an optical tuning of the energy level alignment. The ELAs at Au/DAE1 interfaces as well as the P3HT/DAE1 and N2200/DAE1 interfaces were investigated by sequential deposition method, the measured alignment schemes at interfaces reveal totally different energy level offsets for charge injections before and after photoswitching, as a result, leading to photo-controlled charge transport barriers.

Second, after getting familiar with the electronic properties of DAEs, the application of this photoswitch was extended to hybrid inorganic/organic interfaces, where ZnO polar crystal was the inorganic component. In this study, the phosphonic-acid PA-DAE molecular switches were employed to chemically modify the polar ZnO surfaces [ZnO(0001) and ZnO(000-1)] in the form of SAMs. The study was divided into three parts: *i*) the characterization of the quality of photoswitchable SAMs. With a range of surface characterization techniques and quantification of XPS, it was concluded that PA-DAEs form a densely packed monolayer with a packing density of 2.2 molecules nm^{-2}; *ii*) after modification with PA-DAE, the electronic properties at the ZnO/PA-DAE hybrid interface were reversibly switched upon light illumination; the HOMO level shifts towards E_F by 0.7 eV when switching from open to closed forms. As measured by UPS, the ZnO surface potential was increased due to the formation of surface dipoles; *iii*) DFT calculations on the ZnO/PA-DAE system pointed to that the potential increase was due to the formation of bond dipole localized at the PA, the molecular dipole moment and potential change of ZnO surface due to water release. These findings can further be exploited to reversibly switch the energy level alignment at the ZnO/PA-DAE interface in device structures.

The third part of the work was an extension of previous studies. It has been proved that PA-DAE was successfully employed to modify inorganic metal oxide (ZnO), thus the

modification with photochromic SAM on ITO electrodes was expected to be feasible and was further detailed studied. It was proved that the packing density (ca. 2 molecules nm^{-2}) of PA-DAE on ITO was comparable to that on ZnO, and the molecules adopted an average tilt angle of ca. 30° with respect to the surface normal. Upon illumination with ultraviolet and green light, it was observed that the frontier occupied levels reversibly shifted by 0.7 eV, and concomitantly a reversible work function changed by ca. 60 meV. These results are important for the fabrication of ITO-based photoswitchable devices.

In the fourth system, to investigate a multiple stimuli-induced electronic changes, a T-type photoswitch, Py-DHP, was chosen as a candidate. Py-DHP switches optically in one direction and switches back both thermally. The switch was used to modify the ZnO polar crystal surface and it was proved that both light and thermal energy can be used to switch the molecule. Regarding the electronic properties, in the monolayer coverage the ELA revealed Fermi level pinning due to the presence of Py-DHP molecular dipoles. The surface electronic properties of ZnO can be switched either with light or heat treatment. In multilayer coverages, work function increase of 0.3 eV and 0.5 eV upon photoswitching were observed on ZnO(0001) and ZnO(000-1), respectively, which led to different ionization potentials of Py-DHP compared to in monolayer. These observations were attributed to the molecular orientation transition from a preferential standing up to lying down structure.

6.2 Outlook

In this work, a systematic study of photoswitches at (hybrid) interfaces was presented. The findings provide a solid basis for the rational use of photochromic molecules for dynamically tuning interface energy levels regarding charge transport and injection. This work will hopefully aid the development of photoswitchable (opto-)electronic devices. Based on the current results obtained and conclusions summarized in this thesis, future work will be worthwhile in order to further understand the physical properties of photoswitches both in films and at interfaces:

1. Current illumination of light is so macroscopic that photoswitching occurs on the whole sample area, the influence of local (or single molecule) switching on surrounding molecules will not be detected. It will be interesting to further look at the nano-photoswitching or single molecule switching, such as the illumination applied at near field with small light spot size.

2. The fabrication photoswitchable devices, such as photoswitchable OFETs, diodes, based on the hybrid inorganic/photoswitch systems will be interesting, and help further understand the interface electronic properties.

Bibliography

(1) Horowitz, G. Organic Field-Effect Transistors. *Adv. Mater.* **1998**, *10*, 365–377.

(2) Tang, C. W.; VanSlyke, S. A. Organic electroluminescent diodes. *Appl. Phys. Lett.* **1987**, *51*, 913–915.

(3) Tang, C. W. Two-layer organic photovoltaic cell. *Appl. Phys. Lett.* **1986**, *48*, 183–185.

(4) Li, G.; Zhu, R.; Yang, Y. Polymer solar cells. *Nature Photon* **2012**, *6*, 153–161.

(5) Krebs, F. C.; Espinosa, N.; Hösel, M.; Søndergaard, R. R.; Jørgensen, M. 25th Anniversary Article: Rise to Power - OPV-Based Solar Parks. *Adv. Mater.* **2014**, *26*, 29–39.

(6) Brütting, W.; Frischeisen, J.; Schmidt, T. D.; Scholz, B. J.; Mayr, C. Device efficiency of organic light-emitting diodes: Progress by improved light outcoupling. *Phys. Status Solidi A* **2013**, *210*, 44–65.

(7) Cao, W.; Xue, J. Recent progress in organic photovoltaics: device architecture and optical design. *Energy Environ. Sci.* **2014**, *7*, 2123.

(8) Dimitrakopoulos, C. D.; Malenfant, P.R.L. Organic Thin Film Transistors for Large Area Electronics. *Adv. Mater.* **2002**, *14*, 99–117.

(9) Kelley, T.; W. Baude; Paul F. Gerlach; Chris Ender; David E. Muyres; Dawn Haase; Michael A. Vogel; Dennis E. Theiss; Steven D. Recent Progress in Organic Electronics: Materials, Devices, and Processes. *Chem. Mater.* **2004**, *16*, 4413–4422.

(10) Sekine, C.; Tsubata, Y.; Yamada, T.; Kitano, M.; Doi, S. Recent progress of high performance polymer OLED and OPV materials for organic printed electronics. *Sci. Technol. Adv. Mater.* **2014**, *15*, 34203.

(11) Sirringhaus, H. Device Physics of Solution-Processed Organic Field-Effect Transistors. *Adv. Mater.* **2005**, *17*, 2411–2425.

(12) Koch, N. Organic electronic devices and their functional interfaces. *ChemPhysChem* **2007**, *8*, 1438–1455.

(13) Heimel, G.; Brédas, J.-L. Reflections on charge transport. *Nature Nanotech* **2013**, *8*, 230–231.

(14) Olthof, S.; Meerheim, R.; Schober, M.; Leo, K. Energy level alignment at the interfaces in a multilayer organic light-emitting diode structure. *Phys. Rev. B* **2009**, *79*, 245308.

(15) Hu, Z.; Zhong, Z.; Chen, Y.; Sun, C.; Huang, F.; Peng, J.; Wang, J.; Cao, Y. Energy-Level Alignment at the Organic/Electrode Interface in Organic Optoelectronic Devices. *Adv. Funct. Mater.* **2016**, *26*, 129–136.

(16) Opitz, A.; Frisch, J.; Schlesinger, R.; Wilke, A.; Koch, N. Energy level alignment at interfaces in organic photovoltaic devices. *J. Electron Spectr. Rel. Phenom.* **2013**, *190*, 12–24.

(17) Ishii, H.; Sugiyama, K.; Ito.E.; Seki, K. Energy Level Alignment and Interfacial Electronic Structures at Organic/Metal and Organic/Organic Interfaces. *Adv. Mater.* **1999**, *11*, 605–625.

(18) Koch, N.; Duhm, S.; Rabe, J. P.; Vollmer, A.; Johnson, R. L. Optimized hole injection with strong electron acceptors at organic-metal interfaces. *Physical Review Letters* **2005**, *95*, 237601.

(19) Schlesinger, R.; Xu, Y.; Hofmann, O. T.; Winkler, S.; Frisch, J.; Niederhausen, J.; Vollmer, A.; Blumstengel, S.; Henneberger, F.; Rinke, P. *et al.* Controlling the work function of ZnO and the energy-level alignment at the interface to organic semiconductors with a molecular electron acceptor. *Phys. Rev. B* **2013**, *87*, 155311.

(20) Orgiu, E.; Crivillers, N.; Herder, M.; Grubert, L.; Pätzel, M.; Frisch, J.; Pavlica, E.; Duong, D. T.; Bratina, G.; Salleo, A. *et al.* Optically switchable transistor via energy-level phototuning in a bicomponent organic semiconductor. *Nature Chem* **2012**, *4*, 675–679.

(21) Frisch, J.; Herder, M.; Herrmann, P.; Heimel, G.; Hecht, S.; Koch, N. Photoinduced reversible changes in the electronic structure of photochromic diarylethene films. *Appl. Phys. A* **2013**, *113*, 1–4.

(22) Mosciatti, T.; del Rosso, M. G.; Herder, M.; Frisch, J.; Koch, N.; Hecht, S.; Orgiu, E.; Samorì, P. Light-Modulation of the Charge Injection in a Polymer Thin-Film Transistor by Functionalizing the Electrodes with Bistable Photochromic Self-Assembled Monolayers. *Adv. Mater.* **2016**, *28*, 6606–6611.

(23) Gobbi, M.; Bonacchi, S.; Lian, J. X.; Vercouter, A.; Bertolazzi, S.; Zyska, B.; Timpel, M.; Tatti, R.; Olivier, Y.; Hecht, S. *et al.* Collective molecular switching in hybrid superlattices for light-modulated two-dimensional electronics. *Nat. Commun.* **2018**, *9*, 2661.

(24) Raimondo, C.; Crivillers, N.; Reinders, F.; Sander, F.; Mayor, M.; Samorì, P. Optically switchable organic field-effect transistors based on photoresponsive gold nanoparticles blended with poly(3-hexylthiophene). *Proc. Natl. Acad. Sci.* **2012**, *109*, 12375–12380.

(25) Wakayama, Y.; Hayakawa, R.; Seo, H.-S. Recent progress in photoactive organic field-effect transistors. *Sci. Technol. Adv. Mater.* **2014**, *15*, 24202.

(26) Kathan, M.; Hecht, S. Photoswitchable molecules as key ingredients to drive systems away from the global thermodynamic minimum. *Chem. Soc. Rev.* **2017**, *46*, , 5536--5550.

(27) Frolova, L. A.; Troshin, P. A.; Susarova, D. K.; Kulikov, A. V.; Sanina, N. A.; Aldoshin, S. M. Photoswitchable organic field-effect transistors and memory elements comprising an interfacial photochromic layer. *Chem. Commun.* **2015**, *51*, 6130–6132.

(28) Wang, Q.; Frisch, J.; Herder, M.; Hecht, S.; Koch, N. Electronic Properties of Optically Switchable Photochromic Diarylethene Molecules at the Interface with Organic Semiconductors. *ChemPhysChem* **2017**, *18*, 722–727.

(29) Hayakawa, R.; Petit, M.; Higashiguchi, K.; Matsuda, K.; Chikyow, T.; Wakayama, Y. Interface engineering for improving optical switching in a diarylethene-channel transistor. *Org. Electron.* **2015**, *21*, 149–154.

(30) Böckmann, M.; Doltsinis, N. L.; Marx, D. Azobenzene photoswitches in bulk materials. *Physical review. E, Statistical, nonlinear, and soft matter physics* **2008**, *78*, 36101.

(31) Heilemann, M.; Dedecker, P.; Hofkens, J.; Sauer, M. Photoswitches: Key molecules for subdiffraction-resolution fluorescence imaging and molecular quantification. *Laser & Photon. Rev.* **2009**, *3*, 180–202.

(32) Szymański, W.; Beierle, J. M.; Kistemaker, H. A. V.; Velema, W. A.; Feringa, B. L. Reversible photocontrol of biological systems by the incorporation of molecular photoswitches. *Chem. Rev.* **2013**, *113*, 6114–6718.

(33) Irie, M. Diarylethenes for Memories and Switches. *Chem. Rev.* **2000**, *100*, 1685–1716.

(34) Paniagua, S. A.; Giordano, A. J.; Smith, O.'N. L.; Barlow, S.; Li, H.; Armstrong, N. R.; Pemberton, J. E.; Brédas, J.-L.; Ginger, D.; Marder, S. R. Phosphonic Acids for Interfacial Engineering of Transparent Conductive Oxides. *Chem. Rev.* **2016**, *116*, 7117–7158.

(35) Lange, I.; Reiter, S.; Pätzel, M.; Zykov, A.; Nefedov, A.; Hildebrandt, J.; Hecht, S.; Kowarik, S.; Wöll, C.; Heimel, G. *et al.* Tuning the Work Function of Polar Zinc Oxide Surfaces using Modified Phosphonic Acid Self-Assembled Monolayers. *Adv. Funct. Mater.* **2014**, *24*, 7014–7024.

(36) Schlesinger, R.; Bianchi, F.; Blumstengel, S.; Christodoulou, C.; Ovsyannikov, R.; Kobin, B.; Moudgil, K.; Barlow, S.; Hecht, S.; Marder, S. R. *et al.* Efficient light emission from inorganic and organic semiconductor hybrid structures by energy-level tuning. *Nat. Commun.* **2015**, *6*, 237401.

(37) Piersimoni, F.; Schlesinger, R.; Benduhn, J.; Spoltore, D.; Reiter, S.; Lange, I.; Koch, N.; Vandewal, K.; Neher, D. Charge transfer absorption and emission at ZnO/organic interfaces. *J. Phys. Chem. Lett.* **2015**, *6*, 500–504.

(38) Wu, G.; Li, Z.; Zhang, X.; Lu, G. Charge Separation and Exciton Dynamics at Polymer/ZnO Interface from First-Principles Simulations. *J. Phys. Chem. Lett.* **2014**, *5*, 2649–2656.

(39) Farchioni, R.; Grosso, G. (e.). *Organic Electronic Materials: Conjugated Polymers and Low Molecular Weight Organic Solids*; Springer: Springer-Verlag Berlin Heidelberg GmbH, 2001.

(40) Costa, J. C.S.; Taveira, R. J.S.; Lima, C. F.R.A.C.; Mendes, A.; Santos, L. M.N.B.F. Optical band gaps of organic semiconductor materials. *Opt. Mater.* **2016**, *58*, 51–60.

(41) Tsiper, E. V.; Soos, Z. G.; Gao, W.; Kahn, A. Electronic polarization at surfaces and thin films of organic molecular crystals: PTCDA. *Chem. Phys. Lett.* **2002**, *360*, 47–52.

(42) D'Avino, G.; Muccioli, L.; Castet, F.; Poelking, C.; Andrienko, D.; Soos, Z. G.; Cornil, J.; Beljonne, D. Electrostatic phenomena in organic semiconductors: fundamentals and implications for photovoltaics. *J. Phys.: Condens. Matter* **2016**, *28*, 433002.

(43) Yoshida, H.; Yamada, K.; Tsutsumi, J.'y.; Sato, N. Complete description of ionization energy and electron affinity in organic solids: Determining contributions from electronic polarization, energy band dispersion, and molecular orientation. *Phys. Rev. B* **2015**, *92*, 75145.

(44) Schwoerer, M.; Wolf, H. C. *organic molecular solid*; Wiley-VCH Verlag: Germany, 2007.

(45) Nayak, P. K.; Periasamy, N. Calculation of electron affinity, ionization potential, transport gap, optical band gap and exciton binding energy of organic solids using 'solvation' model and DFT. *Org. Electron.* **2009**, *10*, 1396–1400.

(46) Zhang, X.; Hou, L.; Samorì, P. Coupling carbon nanomaterials with photochromic molecules for the generation of optically responsive materials. *Nat Commun* **2016**, *7*, 11118.

(47) Irie, M. Photochromism of diarylethene molecules and crystals. *Proc. Jpn. Acad., Ser. B* **2010**, *86*, 472–483.

(48) Kim, D.; Jeong, H.; Hwang, W.-T.; Jang, Y.; Sysoiev, D.; Scheer, E.; Huhn, T.; Min, M.; Lee, H.; Lee, T. Reversible Switching Phenomenon in Diarylethene Molecular Devices with Reduced Graphene Oxide Electrodes on Flexible Substrates. *Adv. Funct. Mater.* **2015**, *25*, 5918–5923.

(49) Irie, M.; Fukaminato, T.; Matsuda, K.; Kobatake, S. Photochromism of Diarylethene Molecules and Crystals: Memories, Switches, and Actuators. *Chem. Rev.* **2014**, *114*, 12174–12277.

(50) Robert F. Pierret, Gerold W. Neudeck. *Advanced-Semiconductor-Fundamentals-Se-Robert-F-Pierret-OCR*; Pearson Education, inc, 1987.

(51) Kronig, R. d. L.; Penney, W. G. Quantum mechanics of electrons in crystal lattices. *Proc. Royal Soc. Lond.* **1931**, 499–513.

(52) Bruch, L. W. Theory of physisorption interactions. *Surf. Sci* **1983**, *125*, 194–217.

(53) Amsalem, P.; Niederhausen, J.; Wilke, A.; Heimel, G.; Schlesinger, R.; Winkler, S.; Vollmer, A.; Rabe, J. P.; Koch, N. Role of charge transfer, dipole-dipole interactions, and electrostatics in Fermi-level pinning at a molecular heterojunction on a metal surface. *Phys. Rev. B* **2013**, *87*, 244704.

(54) Heimel, G.; Salzmann, I.; Duhm, S.; Koch, N. Design of Organic Semiconductors from Molecular Electrostatics. *Chem. Mater.* **2011**, *23*, 359–377.

(55) Neucheva, O. Investigation of a metal-organic interface - realization and understanding of a molecular switch (graduation thesis), 2010.

(56) Knupfer, M.; Peisert, H. Electronic properties of interfaces between model organic semiconductors and metals. *phys. stat. sol. (a)* **2004**, *201*, 1055–1074.

(57) Braun, S.; Salaneck, W. R. Fermi level pinning at interfaces with tetrafluorotetracyanoquinodimethane (F4-TCNQ): The role of integer charge transfer states. *Chem. Phys. Lett.* **2007**, *438*, 259–262.

(58) Bokdam, M.; Çakır, D.; Brocks, G. Fermi level pinning by integer charge transfer at electrode-organic semiconductor interfaces. *Appl. Phys. Lett.* **2011**, *98*, 113303.

(59) Braun, S.; Salaneck, W. R.; Fahlman, M. Energy-level alignment at organic/metal and organic/organic interfaces. *Adv. Mater.* **2009**, *21*, 1450–1472.

(60) Hofmann, O. T.; Rinke, P.; Scheffler, M.; Heimel, G. Integer versus Fractional Charge Transfer at Metal(/Insulator)/Organic Interfaces: Cu(/NaCl)/TCNE. *ACS Nano* **2015**, *9*, 5391–5404.

(61) Rissner, F.; Rangger, G. M.; Hofmann, O. T.; Track, A. M.; Heimel, G.; Zojer, E. Understanding the electronic structure of metal/SAM/organic-semiconductor heterojunctions. *ACS Nano* **2009**, *3*, 3513–3520.

(62) Kahn, A.; Koch, N.; Gao, W. Electronic structure and electrical properties of interfaces between metals and ?-conjugated molecular films. *J. Polym. Sci. B Polym. Phys.* **2003**, *41*, 2529–2548.

(63) Fukuda, K.; Hamamoto, T.; Yokota, T.; Sekitani, T.; Zschieschang, U.; Klauk, H.; Someya, T. Effects of the alkyl chain length in phosphonic acid self-assembled monolayer gate dielectrics on the performance and stability of low-voltage organic thin-film transistors. *Appl. Phys. Lett.* **2009**, *95*, 203301.

(64) Ulman, A. Formation and Structure of Self-Assembled Monolayers. *Chem. Rev.* **1996**, *96*, 1533–1554.

(65) Paniagua, S. A.; Hotchkiss, P. J.; Jones, S. C.; Marder, S. R.; Mudalige, A.; Marrikar, F. S.; Pemberton, J. E.; Armstrong, N. R. Phosphonic Acid Modification of Indium−Tin Oxide Electrodes: Combined XPS/UPS/Contact Angle Studies. *J. Phys. Chem. C* **2008**, *112*, 7809–7817.

(66) Wood, C.; Li, H.; Winget, P.; Brédas, J.-L. Binding Modes of Fluorinated Benzylphosphonic Acids on the Polar ZnO Surface and Impact on Work Function. *J. Phys. Chem. C* **2012**, *116*, 19125–19133.

(67) Timpel, M.; Li, H.; Nardi, M. V.; Wegner, B.; Frisch, J.; Hotchkiss, P. J.; Marder, S. R.; Barlow, S.; Brédas, J.-L.; Koch, N. Electrode Work Function Engineering with Phosphonic Acid Monolayers and Molecular Acceptors: Charge Redistribution Mechanisms. *Adv. Funct. Mater.* **2018**, *28*, 1704438.

(68) Li, H.; Paramonov, P.; Brédas, J.-L. Theoretical study of the surface modification of indium tin oxide with trifluorophenyl phosphonic acid molecules: impact of coverage density and binding geometry. *J. Mater. Chem.* **2010**, *20*, 2630.

(69) Paniagua, S. A.; Hotchkiss, P. J.; Jones, S. C.; Marder, S. R.; Mudalige, A.; Marrikar, F. S.; Pemberton, J. E.; Armstrong, N. R. Phosphonic Acid Modification of Indium−Tin Oxide Electrodes: Combined XPS/UPS/Contact Angle Studies. *J. Phys. Chem. C* **2008**, *112*, 7809–7817.

(70) St. Hövel; Kolczewski, C.; Wühn, M.; Albers, J.; Weiss, K.; Staemmler, V.; Wöll, C. Pyridine adsorption on the polar ZnO(0001) surface: Zn termination versus O termination. *J. Chem. Phys.* **2000**, *112*, 3909–3916.

(71) J. F. Walsh; R. Davis; C. A. Muryn; G. Thornton; V. R. Dhanak; and K. C. Prince. Orientation of benzene and pyridine on ZnO(1010). *Phys. Rev. B* **1993**, *48*, 749–752.

(72) Hofmann, O. T.; Deinert, J.-C.; Xu, Y.; Rinke, P.; Stähler, J.; Wolf, M.; Scheffler, M. Large work function reduction by adsorption of a molecule with a negative electron affinity: Pyridine on ZnO(101-0). *J. Chem. Phys.* **2013**, *139*, 174701.

(73) Cornil, D.; Cornil, J. Work-function modification of the (111) gold surface upon deposition of self-assembled monolayers based on alkanethiol derivatives. *J. Electron Spectr. Rel. Phenom.* **2013**, *189*, 32–38.

(74) Ramprasad, R.; Allmen, P. v.; Fonseca, L. R. C. Contributions to the work function: A density-functional study of adsorbates at graphene ribbon edges. *Phys. Rev. B* **1999**, *60*, 6023–6027.

(75) Freysoldt, C.; Neugebauer, J.; Van de Walle, Chris G. Electrostatic interactions between charged defects in supercells. *Phys. Status Solidi B* **2011**, *248*, 1067–1076.

(76) Soler, J. M.; Artacho, E.; Gale, J. D.; Garcia, A.; Junquera, J.; Ordejon, P.; Sanchez-Portal, D. The SIESTA method for ab initio order-N materials simulation. *J. Phys.: Condens. Matter* **2002**, *14*, 2745.

(77) Lee, H.-S.; Tuckerman, M. E. Efficient solution of Poisson's equation using discrete variable representation basis sets for Car-Parrinello ab initio molecular dynamics simulations with cluster boundary conditions. *J. Chem. Phys.* **2008**, *129*, 224108.

(78) Saito, N.; Hayashi, K.; Sugimura, H.; Takai, O.; Nakagiri, N. Surface potential images of self-assembled monolayers patterned by organosilanes:ab initio molecular orbital calculations. *Surf. Interface Anal.* **2002**, *34*, 601–605.

(79) Cornil, D.; Olivier, Y.; Geskin, V.; Cornil, J. Depolarization Effects in Self-Assembled Monolayers: A Quantum-Chemical Insight. *Adv. Funct. Mater.* **2007**, *17*, 1143–1148.

(80) Lange, I.; Blakesley, J. C.; Frisch, J.; Vollmer, A.; Koch, N.; Neher, D. Band bending in conjugated polymer layers. *Phys. Rev. Lett.* **2011**, *106*, 216402.

(81) Wang, H.; Amsalem, P.; Heimel, G.; Salzmann, I.; Koch, N.; Oehzelt, M. Band-Bending in Organic Semiconductors: the Role of Alkali-Halide Interlayers. *Adv. Mater.* **2014**, *26*, 925–930.

(82) Oehzelt, M.; Koch, N.; Heimel, G. Organic semiconductor density of states controls the energy level alignment at electrode interfaces. *Nat Commun* **2014**, *5*, 4174.

(83) Oehzelt, M.; Akaike, K.; Koch, N.; Heimel, G. Energy-level alignment at organic heterointerfaces. *Sci. Adv.* **2015**, *1*, e1501127.

(84) Hill, I. G.; Milliron, D.; Schwartz, J.; Kahn, A. Organic semiconductor interfaces: electronic structure and transport properties. *Appl. Surf. Sci.* **2000**, *166*, 354–362.

(85) Hüfner, S. *Photoelectron Spectroscopy 3rd edition*; Springer-Verlag Berlin Heidelberg, 2003.

(86) Schattke, W.; van Hove, M. A. *Solid-State Photoemission and Related Methods: Theory and Experiment*; WILEY-VCH GmbH & Co. KGaA, 2003.

(87) Berglund, C. N.; Spicer, W. E. Photoemission Studies of Copper and Silver: Theory. *Phys. Rev.* **1964**, *136*, A1030-A1044.

(88) Schwabl, F. *Quantum mechanics*; Springer-Verlag: Berlin, 2007.

(89) S. Tanuma, C. J. Powell and D. R. Penn. Calculations of electron inelastic mean free paths for 31 materials. *Surf. Interface Anal.* **1988**, *11*, 577–589.

(90) Seah, M. P.; Dench, W. A. Quantitative electron spectroscopy of surfaces: A standard data base for electron inelastic mean free paths in solids. *Surf. Interface Anal.* **1979**, *1*, 1–11.

(91) Tanuma, S.; Powell, C. J.; Penn, D. R. Calculation of electron inelastic mean free paths (IMFPs) VII. Reliability of the TPP-2M IMFP predictive equation. *Surf. Interface Anal.* **2003**, *35*, 268–275.

(92) Biesinger, M. C.; Payne, B. P.; Lau, L. W. M.; Gerson, A.; St. Smart, R. C. X-ray photoelectron spectroscopic chemical state quantification of mixed nickel metal, oxide and hydroxide systems. *Surf. Interface Anal.* **2009**, *41*, 324–332.

(93) Hehn, I.; Schuster, S.; Wächter, T.; Abu-Husein, T.; Terfort, A.; Zharnikov, M.; Zojer, E. Employing X-ray Photoelectron Spectroscopy for Determining Layer Homogeneity in Mixed Polar Self-Assembled Monolayers. *J. Phys. Chem. Lett.* **2016**, *7*, 2994–3000.

(94) Cabarcos, O. M.; Shaporenko, A.; Weidner, T.; Uppili, S.; Dake, L. S.; Zharnikov, M.; Allara, D. L. Physical and Electronic Structure Effects of Embedded Dipoles in Self-Assembled Monolayers: Characterization of Mid-Chain Ester Functionalized Alkanethiols on Au{111}. *J. Phys. Chem. C* **2008**, *112*, 10842–10854.

(95) Cabarcos, O. M.; Schuster, S.; Hehn, I.; Zhang, P. P.; Maitani, M. M.; Sullivan, N.; Giguère, J.-B.; Morin, J.-F.; Weiss, P. S.; Zojer, E. *et al.* Effects of Embedded Dipole Layers on Electrostatic Properties of Alkanethiolate Self-Assembled Monolayers. *J. Phys. Chem. C* **2017**, *121*, 15815–15830.

(96) Moulder, J. F.; Stickle, W. F.; Sobol, P. E.; Bomben, K. D. *Handbook of X-ray photoelectron spectroscopy (2nd Edition)*; Perkin-Elmer Corporation: Minnesota, 1992.

(97) Zommer, L. Determination of the spectrometer transmission function for XPS quantitative analysis. *Vacuum* **1995**, *46*, 617–620.

(98) Trzhaskovskaya, M. B.; Nefedov, V. I.; Yarzhemsky, V. G. Photoelectron angular distribution parameters for elements Z=1 to Z=54 in the photoelectron energy range 100-5000 eV. *At. Data Nucl. Data Tables* **2001**, *77*.

(99) Gelius, U.; Siegbahn, K. ESCA Studies of Molecular Core and Valence Levels in the Gas Phase. *Faraday Discuss. Chem. Soc.* **1972**, *54*, 257–268.

(100) Yeh, J. J.; Lindau, I. Atomic subshell photoionization cross sections and asymmetry parameters. *At. Data Nucl. Data Tables* **1985**, *32*, 1–155.

(101) Haase, J. NEXAFS and SEXAFS studies of chemisorbed molecules. *Appl. Phys. A* **1985**, *38*, 181–190.

(102) Bagus, P. S.; Weiss, K.; Schertel, A.; Wöll, C.; Braun, W.; Hellwig, C.; Jung, C. Identification of transitions into Rydberg states in the X-ray absorption spectra of condensed long-chain alkanes. *Chem. Phys. Lett.* **1996**, *248*, 129–135.

(103) Bagus, P. S.; Krauss, M.; Lavilla, R. E. The threshold region of the methane carbon K-absorption spectrum. *Chem. Phys. Lett.* **1973**, *23*, 13–17.

(104) Urquhart, S. G.; Gillies, R. Rydberg-valence mixing in the carbon 1s near-edge X-ray absorption fine structure spectra of gaseous alkanes. *J. Phys. Chem. A* **2005**, *109*, 2151–2159.

(105) Stohr, J.; Outka, D. A. Determination of molecular orientations on surfaces from the angular dependence of near-edge x-ray-absorption fine-structure spectra. *Phys. Rev. B* **1987**, *36*, 7891–7905.

(106) Hähner, G. Near edge X-ray absorption fine structure spectroscopy as a tool to probe electronic and structural properties of thin organic films and liquids. *Chem. Soc. Rev.* **2006**, *35*, 1244–1255.

(107) Patel, S. N.; Su, G. M.; Luo, C.; Wang, M.; Perez, L. A.; Fischer, D. A.; Prendergast, D.; Bazan, G. C.; Heeger, A. J.; Chabinyc, M. L. *et al.* NEXAFS Spectroscopy Reveals the Molecular Orientation in Blade-Coated Pyridal[2,1,3]thiadiazole-Containing Conjugated Polymer Thin Films. *Macromolecules* **2015**, *48*, 6606–6616.

(108) Binnig, G.; Quate, C. F.; Gerber, C. Atomic Force Microscope. *Phys. Rev. Lett.* **1986**, *56*, 930–933.

(109) Melitz, W.; Shen, J.; Kummel, A. C.; Lee, S. Kelvin probe force microscopy and its application. *Surf Sci Rep.* **2011**, *66*, 1–27.

(110) Payton, O.; Champneys, A. R.; Homer, M. E.; Picco, L.; Miles, M. J. Feedback-induced instability in tapping mode atomic force microscopy: theory and experiment. *Proc. R. Soc. A* **2011**, *467*, 1801–1822.

(111) Born, M.; Oppenheimer, R. Zur Quantentheorie der Molekeln. *Ann. Phys.* **1927**, *389*, 457–484.

(112) Koch, W.; Holthausen, M. C. *A chemist's guide to density functional theory*, 2nd ed., 5. reprint; Wiley-VCH: Weinheim, 2008.

(113) Teller, E. On the Stability of Molecules in the Thomas-Fermi Theory. *Rev. Mod. Phys.* **1962**, *34*, 627–631.

(114) Hohenberg, P.; Kohn, W. Inhomogeneous Electron Gas. *Phys. Rev.* **1964**, *136*, B864-B870.

(115) Kohn, W.; Sham, L. J. Self-Consistent Equations Including Exchange and Correlation Effects. *Phys. Rev.* **1965**, *140*, 1133–1138.

(116) Perdew, J. P.; Burke, K.; Ernzerhof, M. Generalized Gradient Approximation Made Simple. *Phys. Rev. Lett.* **1996**, *77*, 3865–3868.

(117) Gemayel, M. E.; Börjesson, K.; Herder, M.; Duong, D. T.; Hutchison, J. a.; Ruzié, C.; Schweicher, G.; Salleo, A.; Geerts, Y.; Hecht, S. *et al.* Optically switchable transistors by simple incorporation of photochromic systems into small-molecule semiconducting matrices. *Nat. Commun.* **2015**, *6*, 6330.

(118) Herder, M.; Eisenreich, F.; Bonasera, A.; Grafl, A.; Grubert, L.; Pätzel, M.; Schwarz, J.; Hecht, S. Light-Controlled Reversible Modulation of Frontier Molecular Orbital Energy Levels in Trifluoromethylated Diarylethenes. *Chem. Eur. J.* **2017**, *23*, 3743–3754.

(119) Herder, M.; Schmidt, B. M.; Grubert, L.; Pätzel, M.; Schwarz, J.; Hecht, S. Improving the fatigue resistance of diarylethene switches. *J. Am. Chem. Soc.* **2015**, *137*, 2738–2747.

(120) Frisch, J.; Vollmer, A.; Rabe, J. P.; Koch, N. Ultrathin polythiophene films on an intrinsically conducting polymer electrode: Charge transfer induced valence states and interface dipoles. *Org. Electron.* **2011**, *12*, 916–922.

(121) Frisch, J.; Vollmer, A.; Koch, N. Energy level pinning of an n-type semiconducting polymer on conductive polymer electrodes: Effects of work function and annealing. *J. Appl. Phys.* **2012**, *112*, 33712.

(122) Lauritsen, J. V.; Porsgaard, S.; Rasmussen, M. K.; Jensen, M. C. R.; Bechstein, R.; Meinander, K.; Clausen, B. S.; Helveg, S.; Wahl, R.; Kresse, G. *et al.* Stabilization principles for polar surfaces of ZnO. *ACS Nano* **2011**, *5*, 5987–5994.

(123) Jacobs, R.; Zheng, B.; Puchala, B.; Voyles, P. M.; Yankovich, A. B.; Morgan, D. Counterintuitive Reconstruction of the Polar O-Terminated ZnO Surface with Zinc Vacancies and Hydrogen. *J. Phys. Chem. Lett.* **2016**, *7*, 4483–4487.

(124) Timpel, M.; Nardi, M. V.; Ligorio, G.; Wegner, B.; Pätzel, M.; Kobin, B.; Hecht, S.; Koch, N. Energy-Level Engineering at ZnO/Oligophenylene Interfaces with Phosphonate-Based Self-Assembled Monolayers. *ACS Appl. Mater. Interfaces* **2015**, *7*, 11900–11907.

(125) Hösel, M.; Søndergaard, R. R.; Jørgensen, M.; Krebs, F. C. Fast Inline Roll-to-Roll Printing for Indium-Tin-Oxide-Free Polymer Solar Cells Using Automatic Registration. *Energy Technol.* **2013**, *1*, 102–107.

(126) Kim, J. S.; Park, J. H.; Lee, J. H.; Jo, J.; Kim, D.-Y.; Cho, K. Control of the electrode work function and active layer morphology via surface modification of indium tin oxide for high efficiency organic photovoltaics. *Appl. Phys. Lett.* **2007**, *91*, 112111.

(127) Timpel, M.; Nardi, M. V.; Krause, S.; Ligorio, G.; Christodoulou, C.; Pasquali, L.; Giglia, A.; Frisch, J.; Wegner, B.; Moras, P. *et al.* Surface Modification of ZnO(0001)–Zn with Phosphonate-Based Self-Assembled Monolayers: Binding Modes, Orientation, and Work Function. *Chem. Mater.* **2014**, *26*, 5042–5050.

(128) Koch, N.; Pop, D.; Weber, R.L.; Böwering, N.; Winter, B.; Wick, M.; Leising, G.; Hertel, I.V.; Braun, W. Radiation induced degradation and surface charging of organic thin films in ultraviolet photoemission spectroscopy. *Thin Solid Films* **2001**, *391*, 81–87.

(129) Zerulla, D.; Chassé, T. X-ray Induced Damage of Self-Assembled Alkanethiols on Gold and Indium Phosphide. *Langmuir* **1999**, *15*, 5285–5294.

(130) Adamo, C.; Barone, V. Toward reliable density functional methods without adjustable parameters: The PBE0 model. *J. Chem. Phys.* **1999**, *110*, 6158–6170.

(131) Rassolov, V. A.; Ratner, M. A.; Pople, J. A.; Redfern, P. C.; Curtiss, L. A. 6‐31G* basis set for third‐row atoms. *J. Comput. Chem.* **2001**, *22*, 976–984.

(132) Frisch, M. J.; Trucks, G. W.; Schlegel, H. B.; Scuseria, G. E.; Robb, M. A.; Cheeseman, J. R.; Scalmani, G.; Barone, V.; Petersson, G. A.; Nakatsuji, H.*, et al. Gaussian 09*; Gaussian, Inc., Wallingford CT, 2009.

(133) N. Troullier and Jose Luriaas Martins. EfFicient pseudopotentials for plane-wave calculations. *Phys. Rev. B* **1993**, *43*, 1993–2006.

(134) Li, H.; Schirra, L. K.; Shim, J.; Cheun, H.; Kippelen, B.; Monti, O. L. A.; Brédas, J.-L. Zinc Oxide as a Model Transparent Conducting Oxide: A Theoretical and Experimental Study of the Impact of Hydroxylation, Vacancies, Interstitials, and Extrinsic Doping on the Electronic Properties of the Polar ZnO (0002) Surface. *Chem. Mater.* **2012**, *24*, 3044–3055.

(135) Monkhorst, H. J.; Pack, J. D. Special points for Brillouin-zone integrations. *Phys. Rev. B* **1976**, *13*, 5188–5192.

(136) Sprenger, D.; Anderson, O. Deconvolution of XPS spectra. *Fresenius J Anal Chem* **1991**, *341*, 116–120.

(137) Végh, J. The Shirley-equivalent electron inelastic scattering cross-section function. *Surf. Sci.* **2004**, *563*, 183–190.

(138) Tougaard, S. Quantitative analysis of the inelastic background in surface electron spectroscopy. *Surf. Interface Anal.* **1988**, *11*, 453–472.

(139) Tougaard, S. Practical algorithm for background subtraction. *Surf. Sci.* **1989**, *216*, 343–360.

(140) Hawn, D. D.; DeKoven, B. M. Deconvolution as a correction for photoelectron inelastic energy losses in the core level XPS spectra of iron oxides. *Surf. Interface Anal.* **1987**, *10*, 63–74.

(141) Vasquez, R. P.; Klein, J. D.; Barton, J. J.; Grunthaner, F. J. Application of maximum-entropy spectral estimation to deconvolution of XPS data. *J. Electron Spectr. Rel. Phenom.* **1981**, *23*, 63–81.

(142) Chornik, B.; Sopizet, R.; Le Gressus, C. Deconvolution in electron spectroscopy revisited: computational aspects. *J. Electron Spectr. Rel. Phenom* **1987**, *42*, 329–350.

(143) Watts, B.; Thomsen, L.; Dastoor, P. C. Methods in carbon K-edge NEXAFS: Experiment and analysis. *J. Electron Spectr. Rel. Phenom* **2006**, *151*, 105–120.

(144) Hisao, I.; Kiyoshi, S.; Eisuke, I.; Kazuhiko, S. Energy Level Alignment and Interfacial Electronic Structures at Organic/Metal and Organic/Organic Interfaces. *Adv. Mater.* **1999**, *11*, 605–625.

(145) Li, W.; Cai, Y.; Li, X.; Ågren, H.; Tian, H.; Zhu, W.-H. Sterically hindered diarylethenes with a benzobis(thiadiazole) bridge: photochemical and kinetic studies. *J. Mater. Chem. C* **2015**, *3*, 8665–8674.

(146) Li, X.; Li, W.; Ågren, H.; Tian, H.; Zhu, W. Theoretical insight into the enhanced hindrance, thermal stability and optical properties of diarylethene with a benzobis(thiadiazole) bridge and benzothiophene rings. *Dyes Pigm.* **2016**, *125*, 348–355.

(147) Heimel, G.; Brédas, J.-L. Molecular electronics: Reflections on charge transport. *Nature Nanotech* **2013**, *8*, 230–231.

(148) F. Amy, C. Chan, A. Kahn. Polarization at the gold/pentacene interface. *Org. Electron.* **2005**, *6*, 85–91.

(149) Kanai, K.; Miyazaki, T.; Suzuki, H.; Inaba, M.; Ouchi, Y.; Seki, K. Effect of annealing on the electronic structure of poly(3-hexylthiophene) thin film. *Phys. Chem. Chem. Phys.* **2010**, *12*, 273–282.

(150) Campbell, I. H.; Rubin, S.; Zawodzinski, T. A.; Kress, J. D.; Martin, R. L.; Smith, D. L.; Barashkov, N. N.; Ferraris, J. P. Controlling Schottky energy barriers in organic electronic devices using self-assembled monolayers. *Phys. Rev. B* **1996**, *54*, R14321-R14324.

(151) Crivillers, N.; Liscio, a.; Di Stasio, F.; van Dyck, C.; Osella, S.; Cornil, D.; Mian, S.; Lazzerini, G. M.; Fenwick, O.; Orgiu, E. *et al.* Photoinduced work function changes by isomerization of a densely packed azobenzene-based SAM on Au: a joint experimental and theoretical study. *Phys. Chem. Chem. Phys.* **2011**, *13*, 14302–14310.

(152) Wang, Q.; Ligorio, G.; Diez-Cabanes, V.; Cornil, D.; Kobin, B.; Hildebrandt, J.; Nardi, M. V.; Timpel, M.; Hecht, S.; Cornil, J. *et al.* Dynamic Photoswitching of Electron Energy Levels at Hybrid ZnO/Organic Photochromic Molecule Junctions. *Adv. Funct. Mater.* **2018**, *4*, 1800716.

(153) Look, D. C. Recent advances in ZnO materials and devices. *Mater. Sci. Eng.* **2001**, *80*, 383–387.

(154) Mashford, B. S.; Stevenson, M.; Popovic, Z.; Hamilton, C.; Zhou, Z.; Breen, C.; Steckel, J.; Bulovic, V.; Bawendi, M.; Coe-Sullivan, S. *et al.* High-efficiency quantum-dot light-emitting devices with enhanced charge injection. *Nature Photon* **2013**, *7*, 407–412.

(155) Özgür, Ü.; Alivov, Y. I.; Liu, C.; Teke, A.; Reshchikov, M. A.; Doğan, S.; Avrutin, V.; Cho, S.-J.; Morkoç, H. A comprehensive review of ZnO materials and devices. *J. Appl. Phys.* **2005**, *98*, 41301.

(156) Ostapenko, A.; Klöffel, T.; Eußner, J.; Harms, K.; Dehnen, S.; Meyer, B.; Witte, G. Etching of Crystalline ZnO Surfaces upon Phosphonic Acid Adsorption: Guidelines for the Realization of Well-Engineered Functional Self-Assembled Monolayers. *ACS Appl. Mater. Interfaces* **2016**, *8*, 13472–13483.

(157) Götzen, J.; Witte, G. Rapid preparation of highly ordered ultraflat ZnO surfaces. *Appl. Surf. Sci.* **2012**, *258*, 10144–10147.

(158) Paul E. Laibinis, George M. Whitesides. Self-assembled monolayers of n-alkanethiolates on copper are barrier films that protect the metal against oxidation by air. *J. Am. Chem. Soc.* **1992**, *114*, 9022–9028.

(159) Carla A. Alves, Marc D. Porter. Atomic force microscopic characterization of a fluorinated alkanethiolate monolayer at gold and correlations to electrochemical and infrared reflection spectroscopic structural descriptions. *Langmuir* **1993**, *9*, 3507–3512.

(160) Hanson, E. L.; Schwartz, J.; Nickel, B.; Koch, N.; Danisman, M. F. Bonding self-assembled, compact organophosphonate monolayers to the native oxide surface of silicon. *J. Am. Chem. Soc.* **2003**, *125*, 16074–16080.

(161) Hellström, M.; Beinik, I.; Broqvist, P.; Lauritsen, J. V.; Hermansson, K. Subsurface hydrogen bonds at the polar Zn-terminated ZnO(0001) surface. *Phys. Rev. B* **2016**, *94*, 245433.

(162) Li, Z.-X.; Liao, L.-Y.; Sun, W.; Xu, C.-H.; Zhang, C.; Fang, C.-J.; Yan, C.-H. Reconfigurable Cascade Circuit in a Photo- and Chemical-Switchable Fluorescent Diarylethene Derivative. *J. Phys. Chem. C* **2008**, *112*, 5190–5196.

(163) Srikant, V.; Clarke, D. R. On the optical band gap of zinc oxide. *J. Appl. Phys.* **1998**, *83*, 5447–5451.

(164) Cornil, D.; van Regemorter, T.; Beljonne, D.; Cornil, J. Work function shifts of a zinc oxide surface upon deposition of self-assembled monolayers: a theoretical insight. *Phys. Chem. Chem. Phys.* **2014**, *16*, 20887–20899.

(165) Napier, M. E.; Thorp, H. H. Modification of Electrodes with Dicarboxylate Self-Assembled Monolayers for Attachment and Detection of Nucleic Acids. *Langmuir* **1997**, *13*, 6342–6344.

(166) Yamada, H.; Imahori, H.; Nishimura, Y.; Yamazaki, I.; Ahn, T. K.; Kim, S. K.; Kim, D.; Fukuzumi, S. Photovoltaic properties of self-assembled monolayers of porphyrins and porphyrin-fullerene dyads on ITO and gold surfaces. *J. Am. Chem. Soc.* **2003**, *125*, 9129–9139.

(167) Paramonov, P. B.; Paniagua, S. A.; Hotchkiss, P. J.; Jones, S. C.; Armstrong, N. R.; Marder, S. R.; Brédas, J.-L. Theoretical Characterization of the Indium Tin Oxide Surface and of Its Binding Sites for Adsorption of Phosphonic Acid Monolayers. *Chem. Mater.* **2008**, *20*, 5131–5133.

(168) Li, H.; Winget, P.; Brédas, J.-L. Surface Modification of Indium-Tin-Oxide Via Self-Assembly of a Donor-Acceptor Complex: A Density Functional Theory Study. *Adv. Mater.* **2012**, *24*, 687–693.

(169) Kresse, G.; Furthmüller, J. Efficiency of ab-initio total energy calculations for metals and semiconductors using a plane-wave basis set. *Comput. Mater. Sci.* **1996**, *6*, 15–50.

(170) Köhler, L.; Kresse, G. Density functional study of CO on Rh(111). *Phys. Rev. B* **2004**, *70*, 13.

(171) Gliboff, M.; Li, H.; Knesting, K. M.; Giordano, A. J.; Nordlund, D.; Seidler, G. T.; Brédas, J.-L.; Marder, S. R.; Ginger, D. S. Competing Effects of Fluorination on the Orientation of Aromatic and Aliphatic Phosphonic Acid Monolayers on Indium Tin Oxide. *J. Phys. Chem. C* **2013**, *117*, 15139–15147.

(172) Gliboff, M.; Sang, L.; Knesting, K. M.; Schalnat, M. C.; Mudalige, A.; Ratcliff, E. L.; Li, H.; Sigdel, A. K.; Giordano, A. J.; Berry, J. J. *et al.* Orientation of phenylphosphonic acid self-assembled monolayers on a transparent conductive oxide: a combined NEXAFS, PM-IRRAS, and DFT study. *Langmuir* **2013**, *29*, 2166–2174.

(173) Taylor, D. M.; Oliveira, O. N. de; Morgan, H. Models for interpreting surface potential measurements and their application to phospholipid monolayers. *J. Colloid Interface Sci.* **1990**, *139*, 508–518.

(174) Natan, A.; Kronik, L.; Shapira, Y. Computing surface dipoles and potentials of self-assembled monolayers from first principles. *Appl. Surf. Sci.* **2006**, *252*, 7608–7613.

(175) Cornil, D.; Li, H.; Wood, C.; Pourtois, G.; Brédas, J.-L.; Cornil, J. Work-function modification of Au and Ag surfaces upon deposition of self-assembled monolayers: influence of the choice of the theoretical approach and the thiol decomposition scheme. *ChemPhysChem* **2013**, *14*, 2939–2946.

(176) Heimel, G.; Romaner, L.; Brédas, J.-L.; Zojer, E. Interface Energetics and Level Alignment at Covalent Metal-Molecule Junctions: π-Conjugated Thiols on Gold. *Phys. Rev. Lett.* **2006**, *96*.

(177) Russew, M.-M.; Hecht, S. Photoswitches: From Molecules to Materials. *Adv. Mater.* **2010**, *22*, 3348–3360.

(178) Klajn, R. Spiropyran-based dynamic materials. *Chem. Soc. Rev.* **2014**, *43*, 148–184.

(179) Garmshausen, Y.; Klaue, K.; Hecht, S. Dihydropyrene as an Aromaticity Probe for Partially Quinoid Push-Pull Systems. *ChemPlusChem* **2017**, *82*, 1025–1029.

(180) Roldan, D.; Cobo, S.; Lafolet, F.; Vilà, N.; Bochot, C.; Bucher, C.; Saint-Aman, E.; Boggio-Pasqua, M.; Garavelli, M.; Royal, G. A Multi-Addressable Switch Based on the Dimethyldihydropyrene Photochrome with Remarkable Proton-Triggered Photo-opening Efficiency. *Chem. Eur. J.* **2015**, *21*, 455–467.

(181) Bakkar, A.; Lafolet, F.; Boggio-Pasqua, M.; Jouvenot, D.; Saint-Aman, E.; Cobo, S. Electrochemical control of the switching process of photochromic dimethyldihydropyrene derivatives. *Chem. Commun.* **2017**, *53*, 9360–9363.

(182) Ma, Z.; Rissner, F.; Wang, L.; Heimel, G.; Li, Q.; Shuai, Z.; Zojer, E. Electronic structure of pyridine-based SAMs on flat Au(111) surfaces: extended charge rearrangements and Fermi level pinning. *Phys. Chem. Chem. Phys.* **2011**, *13*, 9747–9760.

(183) Topham, B. J.; Kumar, M.; Soos, Z. G. Profiles of Work Function Shifts and Collective Charge Transfer in Submonolayer Metal-Organic Films. *Adv. Funct. Mater.* **2011**, *21*, 1931–1940.

(184) Hisashi Yoshikawa; Sadao Adachi. Optical Constants of ZnO. *Jpn. J. Appl. Phys.* **1997**, *36*, 6237.

(185) Armin, A.; Stoltzfus, D. M.; Donaghey, J. E.; Clulow, A. J.; Nagiri, R. C. R.; Burn, P. L.; Gentle, I. R.; Meredith, P. Engineering dielectric constants in organic semiconductors. *J. Mater. Chem. C* **2017**, *5*, 3736–3747.

(186) Duhm, S.; Heimel, G.; Salzmann, I.; Glowatzki, H.; Johnson, R. L.; Vollmer, A.; Rabe, J. P.; Koch, N. Orientation-dependent ionization energies and interface dipoles in ordered molecular assemblies. *Nature Mater* **2008**, *7*, 326–332.

(187) Chen, W.; Huang, H.; Chen, S.; Huang, Y. L.; Gao, X. Y.; Wee, A. T. S. Molecular Orientation-Dependent Ionization Potential of Organic Thin Films. *Chem. Mater.* **2008**, *20*, 7017–7021.

(188) Chen, W.; Qi, D.-C.; Huang, H.; Gao, X.; Wee, A. T. S. Organic-Organic Heterojunction Interfaces: Effect of Molecular Orientation. *Adv. Funct. Mater.* **2011**, *21*, 410–424.

(189) Klauber, C. Refinement of magnesium and aluminium K-alpha X ray source functions. *Surf. Interface Anal.* **1993**, *20*, 703–715.

(190) Soos, Z. G.; Topham, B. J. Surface dipole of F4TCNQ films: Collective charge transfer and dipole–dipole repulsion in submonolayers. *Org. Electron.* **2011**, *12*, 39–44.

Appendices

A. PES Satellites

X-ray satellite

X-ray line	Al		Mg	
	energy	rel.intensity	energy	rel.intensity
$K\alpha_{1,2}$	1486.6	100	1253.6	100
$K\alpha'$	1492.2	1.0	1258.1	1.0
$K\alpha_3$	1496.2	7.8	1262.0	9.2
$K\alpha_4$	1498.1	3.3	1263.6	5.1
$K\alpha_5$	1506.4	0.4	1270.9	0.8
$K\alpha_6$	1510.0	0.3	1274.1	0.5
$K\beta$	1556.6	2.0	1301.6	2.0

Table A.1. Typical Al K_α and Mg K_α satellites with their relative intensities (rel. intensity) normalized to $K\alpha_{1,2}$ lines.[189]

He-line satellite

UV line	He I		He II	
	energy	rel.intensity	energy	rel.intensity
α	21.22	100	40.82	100
β	23.09	2.5	48.37	2.0
γ	23.74	0.5	51.02	<1

Table A.2. He I and He II satellites with their relative intensities normalized to α-lines.

B. Algorithms for Spectral Evaluation

The following script about spectra processing was written in Wolfram Mathematica. The spectra processing includes the background subtraction and spectra deconvolution.

B.1 Shirley Background Subtraction

1. Input data

```
data:=Sort[ReadList["file path",{Number,Number}]]

length=Length[data];     (*number of point*)

x=data[[All,1]]; (*x coordinate*)

y=data[[All,2]]; (*y coordinate*)

y1=Transpose[{x,Table[data[[1,2]],{i,length}]}];  (*define the
original BG, which is a constant*)
```

2. Define the first BG

```
a={{data[[1,1]],0}};

For[i=1;s=0,i<length,AppendTo[a,{data[[i,1]],s}],s=s+(y[[i]]+y[[
i+1]])*(x[[i+1]]-x[[i]])/2;i++]  (*x[[]] is the x step*)

bg2=Transpose[{x,(Abs[data[[length,2]]-
data[[1,2]]])*(a[[All,2]]-y1[[All,2]])/Max[a[[All,2]]-
y1[[All,2]]]+data[[1,2]]}];  (*normalize BG, then shift to
peak*)
```

3. Self-consistently optimize BG

```
f[aa_,bb_]:=Module[{r,s,t,b}, b=bb; t=1;

While[t<100,r={{data[[1,1]],0}};For[i=1;s=0,i<length,AppendTo[r,
{x[[i]],s}],s=s+(b[[i,2]]+b[[i+1,2]])*((x[[i+1]]-x[[i]]))/2;
i++];

b1=Transpose[{x,(Abs[data[[length,2]]-
data[[1,2]]])*(aa[[All,2]]-r[[All,2]])/Max[aa[[All,2]]-
r[[All,2]]]+data[[1,2]]}];

If[Total[(b[[All,2]]-b1[[All,2]])^2]>0.00000001,b=b1,Break[]];

t++];b1] (*self-consistent system to define Shirley background,
aa and bb are the input parameters of the first background*)
```

4. Output final BG

```
bgfinal=f[a,bg2];

ListLinePlot[{data,bg2,bgfinal},PlotRange->Full]; (*show the
Shirley background and compare the difference between the first
iteration and the final iteration of background*)
```

B.2 Deconvolution of Spectra

Following the algorithm described in reference [136], the deconvolution of the spectrum after background subtraction is:

```
newdata=Transpose[{x,data[[All,2]]-bgfinal[[All,2]]}];

datax=newdata[[All,1]];

datax=datax-Mean[datax];

datay=newdata[[All,2]];

datay=datay-Min[datay];

datay=datay/Max[datay];

Length[datay];

epass=Input["put your pass energy"];  (*the pass energy used
during the PES measurements*)

fwhmpass=If[epass==5,0.214,If[epass==10,0.269,If[epass==20,0.684
,If[epass==30,1.106,If[epass==50,1.794,If[epass==100,3.545,Break
[]]]]]]];  (*note that here the FWHM is dependent on the pass
energy, which is different for different PES setups.*)

fwhm=Sqrt[0.53^2+fwhmpass^2];   (*0.53 is the FWHM of
monochromatic X-ray*)

gy=Exp[-Log[16]*datax^2/fwhm^2];    (*set response function,
datapoint and step of x-axis consistent with input data*)

gy=gy/Max[gy];

deconv[dy_,gaussy_]:=Module[{a,b,c,k},c=0.5;k=1;a=dy;b=gaussy;
```

```
While[k<15000,
conv:=ListConvolve[b,a,{Floor[Length[b]/2]+1,Floor[Length[b]/2]+
1}]; (*discrete convolution is from the center of the spectrum*)

conv=conv-Min[conv];

conv=conv/Max[conv];

a=a-c*(a^2+Abs[a])*(conv-datay);

a=a-Min[a];

a=a/Max[a];

If[Mod[k,100]==0,c=c*5];

If[Sqrt[Total[(conv-datay)^2]]>0.15,k++,Break[]]

];{a,c,k}]      (*c is a parameter which should increase upon
iterations, threshold Sqrt[Total[(conv-datay)^2]]>0.7 should be
carefully defined, the more the iteration steps the poor the
signal and the narrower the peak.   Change parameter c and
threshold*)

final=deconv[datay,gy];

ListLinePlot[{Transpose[{x,datay}],Transpose[{x,final[[1]]}]},Pl
otRange->Full];
```

C. Image Charge Model with Dielectrics

The image charge model discussed here is applied to dielectrics. In contrast to a metallic substrate where charges are free to move on the surface, in dielectrics the charges are bound to atoms and they undergo displacement under the applied electric field.

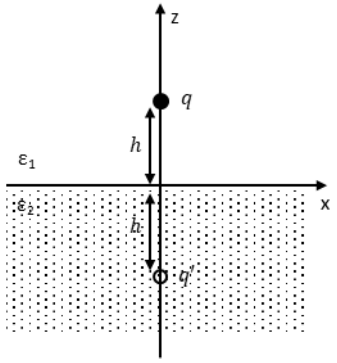

Figure C.1. Schematic illustration of the image charge model. In the material whose dielectric is ε_1, a point charge is located above the interface with a distance of h, while its image charge q' is located below the interface with the same distance h to the interface and the dielectric below the interface is ε_2.

To illustrate the method of image charges for dielectrics, it is considered that in Figure. C.1, a point charge q is in a dielectric ε_1 above the interface, whose distance to the interface is h. Thus the image charge q' is located in a dielectric ε_2 below the interface with the same distance h to the interface. Such a system has to be subjected to the boundary conditions, that is:

$$V_1\big|_{z=0} = V_2\big|_{z=0}, \qquad \varepsilon_1 \frac{\partial V_1}{\partial z}\Big|_{z=0} = \varepsilon_2 \frac{\partial V_2}{\partial z}\Big|_{z=0} \tag{C.1}$$

Now we specify the potential distribution in both dielectrics based on the image charge model (expression is in Cartesian coordinate):

$$\begin{aligned} V_1(x,y,z) &= \frac{1}{4\pi\varepsilon_1}\left[\frac{q}{\sqrt{x^2+y^2+(z-h)^2}} + \frac{q'}{\sqrt{x^2+y^2+(z+h)^2}}\right] && z \geq 0 \\ V_2(x,y,z) &= \frac{1}{4\pi\varepsilon_2}\left[\frac{q+q''}{\sqrt{x^2+y^2+(z-h)^2}}\right] && z \leq 0 \end{aligned} \tag{C.2}$$

Inserting equation C.2 to equation C.1 (the boundary conditions) gives rise to:

$$\begin{aligned} \varepsilon_2(q+q') &= \varepsilon_1(q+q'') \\ q-q' &= q+q'' \end{aligned} \tag{C.3}$$

Therefore, $q'$and q'' are calculated to be:

$$q' = \frac{\varepsilon_1 - \varepsilon_2}{\varepsilon_1 + \varepsilon_2} q, \qquad q'' = -\frac{\varepsilon_1 - \varepsilon_2}{\varepsilon_1 + \varepsilon_2} q \tag{C.4}$$

With $q'$and q'' known, it is thus possible to calculate the potential in equation C.2 and the electric displacement at the interface (the derivative of the potential). Interestingly, Depending on the value of ε_1 and ε_2, the distribution of electric displacement can be different, as shown in Figure C.2.

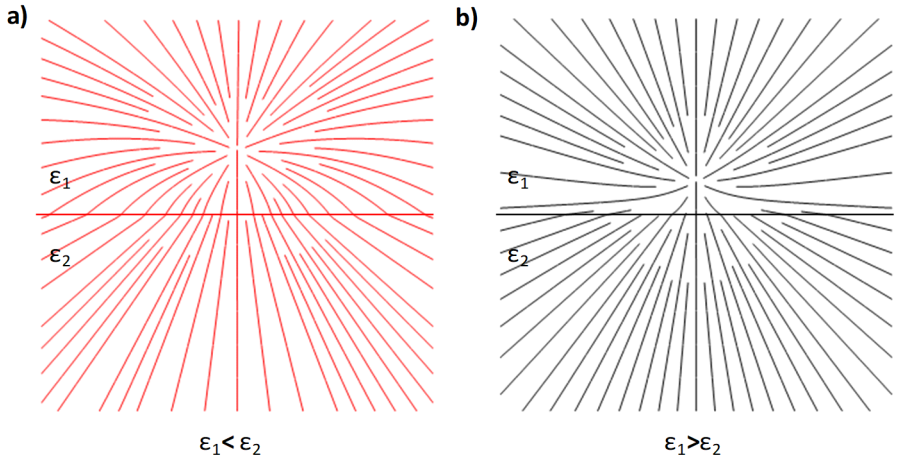

Figure C.2. Distribution of the electric displacement created by a point charge located above the interface in dielectric ε_1. The distribution is totally different in the space in the case of a) $\varepsilon_1 < \varepsilon_2$ and b) $\varepsilon_1 > \varepsilon_2$.

Furthermore, let us consider that charge transfer occurs at the interface of two different dielectrics; this creates a negative point charge in the top (organic) layer and leaves a positive point charge on the surface of the substrate. As described in Figure C.3, the positive and negative charges form charge transfer dimers,[183,190] and the dimer distance is determined by the dipole-dipole repulsions.

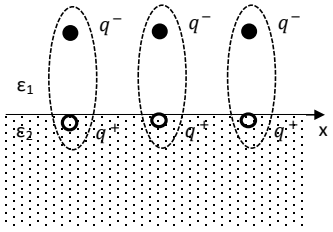

Figure C.3. Charge transfer dimers formed between the substrate and top organic layers. The negative point charge is in the organic layer, while the positive charge is localized on the substrate surface.

Therefore, the potential in the space created by these charge transfer dimers is actually the sum of potentials created by both the negative and positive point charges. Applying the above mentioned image charge models and boundary conditions, the potential distribution in the space is given by:

$$V_1(r,R)=\frac{q^-}{4\pi\varepsilon_1}\left(\frac{1}{r}+\frac{\varepsilon_1-\varepsilon_2}{\varepsilon_1+\varepsilon_2}\frac{1}{r'}\right)-\frac{q^+}{4\pi\varepsilon_1}\frac{2\varepsilon_1}{\varepsilon_1+\varepsilon_2}\frac{1}{R} \qquad z\geq 0$$
$$V_2(r,R)=\frac{q^-}{4\pi\varepsilon_2}\frac{2\varepsilon_2}{\varepsilon_1+\varepsilon_2}\frac{1}{r}-\frac{q^+}{4\pi\varepsilon_2}\left(\frac{1}{R}-\frac{\varepsilon_1-\varepsilon_2}{\varepsilon_1+\varepsilon_2}\frac{1}{R'}\right) \qquad z\leq 0 \qquad \text{(C.5)}$$

Acknowledgements

I would like to gratefully acknowledge many people who have been journeyed with me in the past three years. Without their supports, this dissertation would not have been possible.

I want to thank Prof. Norbert Koch for giving me the opportunity to work on this interesting and exciting iSwitch project in his group. I am thankful for his mentoring and for letting me perform the state of the art experiment both in his lab and at beam station. Particularly, he enabled me to visit several important international conferences and famous groups. This allows me to meet so many experts in the field and to grow as a research scientist.

I want to thank partners for the synthesis of photoswitches: Prof. Stefan Hecht, Dr. Björn Kobin, Jana Hildebrandt, Yves Garmshausen, Wenjie Han. I want to thank Dr. Jérôme Cornil, Dr. David Cornil, and Valentin Diez Cabanes from University of Mons for the support of DFT calculations,

I want to thank all of my colleagues in the SMS group for spending hours helping me with the experiments, and discussing scientific issues. Particularly, Dr. Giovanni Ligorio, Dr. Raphael Schlesinger, who have been very important guides for this thesis.

I would like to thank all the members in the iSwitch project for being together and exchanging knowledge during the iSwitch meeting, I want also to thank Dr. Stefano Prato, Dr. Barbara Troian, Matteo Lo Cicero from APE research for helping perform SPM measurements. It was really a great experience in Trieste.

Finally, I want to thank my family for their support and understanding.

Declaration of independent work

I declare that I have completed the thesis independently using only the aids and tools specified. I have not applied for a doctor's degree in the doctoral subject elsewhere and do not hold a corresponding doctor's degree. I have taken due note of the Faculty of Mathematics and Natural Sciences PhD Regulations.

Qiankun Wang

Berlin, 20.12.2018